ภาคผนวก

วารสารวิชาการระดับนานาชาติที่ได้รับการตีพิมพ์จากงานวิจัยนี้

1. I. Ngamroo (2010). Robust SMES controller design based on inverse additive perturbation for stabilization of interconnected power systems with wind farms. *Energy Conversion and Management*, Vol. 51, Issue 3, March 2010, pp. 459-464. (Impact factor 2009 = 1.944)
2. I. Ngamroo, Cuk Supriyadi A. N., S. Dechanupaprittha, M. Watanabe, Y. Mitani (2010). Wide area robust SMES controller design using synchronized PMUs for stabilization of interconnected power system with wind farms. *IEEJ Transactions on Electrical and Electronics Engineering,* Vol.5, No.4, July.2010, pp. 428-438. (Impact factor 2009 = 0.361)
3. S. Pothiya, I. Ngamroo and W. Kongprawechnon (2010). Ant colony optimisation for economic dispatch problem with nonsmooth cost functions. *International Journal of Electrical Power and Energy Systems*, Vol.32, Issue 5, June 2010, pp.478-487. (Impact factor 2009 = 1.613)
4. S. Vachirasricirikul, I. Ngamroo and S. Kaitwanidvilai (2010). Coordinated SVC and AVR for robust voltage control in a hybrid wind-diesel system. *Energy Conversion and Management*, Vol. 51, Issue 12, December 2010, pp. 2383-2393. (Impact factor 2009 = 1.944)
5. I. Ngamroo (2009). Robust frequency control of wind-diesel hybrid power system using superconducting magnetic energy storage. *International Journal of Emerging Electric Power Systems*, Vol. 10, Issue. 2, April 2009, Article 3. (Impact factor 2008 = NaN)
6. I. Ngamroo, Cuk Supriyadi A. N., S. Dechanupaprittha and Y. Mitani (2009). Power oscillation suppression by robust SMES in power system with large wind power penetration. *Physica C: Superconductivity and Its Applications,* Vol. 469, Issue 1, 1 January 2009, pp. 44-51. (Impact factor 2009 = 0.723)
7. S. Vachirasricirikul, I. Ngamroo and S. Kaitwanidvilai (2009). Application of electrolyzer system to enhance frequency stabilization effect of microturbine in a microgrid system. *International Journal of Hydrogen Energy*, Vol. 34, Issue 17, September 2009, pp. 7131-7142. (Impact factor 2009 = 3.945)

Energy Conversion and Management 51 (2010) 459–464

Contents lists available at ScienceDirect

Energy Conversion and Management

journal homepage: www.elsevier.com/locate/enconman

Robust SMES controller design based on inverse additive perturbation for stabilization of interconnected power systems with wind farms

Issarachai Ngamroo *

Center of Excellence for Innovative Energy Systems, Faculty of Engineering, King Mongkut's Institute of Technology Ladkrabang, Bangkok 10520, Thailand

ARTICLE INFO

Article history:
Received 13 July 2008
Received in revised form 15 March 2009
Accepted 10 October 2009
Available online 11 November 2009

Keywords:
Superconducting magnetic energy storage
Power system stabilization
Wind farms
Robust control
System uncertainties
Inverse additive perturbation

ABSTRACT

This paper proposes a robust controller design of Superconducting Magnetic Energy Storage (SMES) for stabilization of tie-line power oscillation in the interconnected power systems with wind farms. The inverse additive perturbation model is applied to represent system uncertainties such as several generating and loading conditions, variation of system parameters, wind power fluctuations, etc. The structure of active and reactive power controllers of SMES is the first-order lead-lag compensator. To tune the controller parameters, the optimization problem is formulated based on the enhancement of additive stability margin. The genetic algorithm is used to solve the problem and achieve the controller parameters. Simulation studies in the two-area four-machine interconnected power system with wind farms confirm the robustness of the proposed SMES under various operating conditions.

1. Introduction

Nowadays, the wind power generations connected to the grid significantly increase because of low impact to environment and infinite availability. Nevertheless, the wind power is naturally intermittent and unpredictable. The power output fluctuation from wind power generations leads to a severe problem of low frequency oscillations in interconnected power systems due to insufficient system damping [1,2]. Besides, the high penetration of wind power results in a fluctuation of tie-line power flow which may violate the transmission capability margin and deteriorate the system stability [3–6].

To tackle this problem, a Superconducting Magnetic Energy Storage (SMES), which is able to supply and absorb active power rapidly [7,8], has been highly expected as one of the most effective controller of power system stabilization. The SMES has been successfully applied to solve many problems in power systems such as an improvement of power system dynamics [9,10], a frequency control in interconnected power systems [11,12], an improvement of power quality [13], a stabilization of sub-synchronous oscillation in the turbine-generator [14], a load leveling [15], etc. Besides, a SMES unit has been applied to stabilize interconnected power systems with wind farms [16–18]. On the other hand, various generating and loading conditions, unpredictable wind power fluctuations, variation of system parameters and system nonlinearities, etc., result in system uncertainties. The SMES controllers [9–18] have been designed based on an optimization of proportional integral controllers without considering such system uncertainties. Accordingly, it cannot guarantee that they can handle such uncertainties and stabilize the power systems. To handle such system uncertainties, a new SMES controller design which is robust to various uncertainties, is significantly expected.

To enhance the robustness of the SMES controller against system uncertainties, this paper proposes a robust controller design of SMES based on the inverse additive perturbation [19]. In the mathematical modeling, unstructured system uncertainties are represented by the inverse additive perturbation model. The structure of active and reactive power controllers is the first-order lead-lag compensator. Controller parameters are optimized by genetic algorithm (GA) based on the improvement of the robust stability margin of the control system. Simulation studies are carried out in the two-area four-machine interconnected power system with wind farms. Simulation results under various operating conditions such as heavy line flow, weak line, wind power fluctuations and system faults, confirm that the proposed SMES is superior to that of the SMES designed without considering robustness.

2. Study system and modeling

A two-area four-machine interconnected power system [20] in Fig. 1 is used as the study system. Each generator is represented by a five-state transient model. It is equipped with a simplified exciter. The wind farms are located at buses 4 and 14 with maximum

* Tel.: +66 2 326 4550.
E-mail address: ngamroo@gmail.com

0196-8904/$ - see front matter © 2009 Elsevier Ltd. All rights reserved.
doi:10.1016/j.enconman.2009.10.008

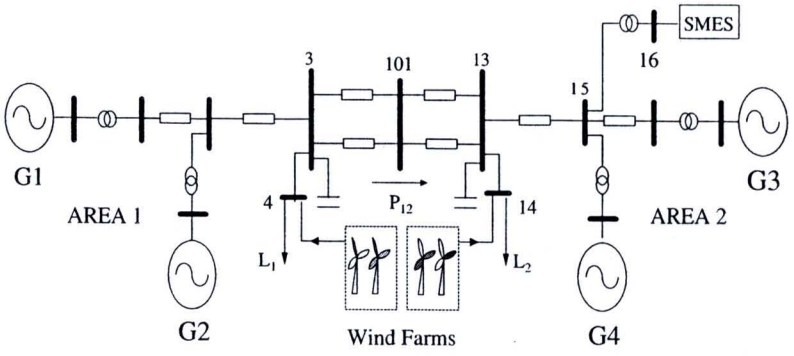

Fig. 1. Two areas four machines power system with wind farms.

generating capacities 405 MW. In this study, the wind farm is modeled by the random active power source. Based on the residue method [21], the suitable location of SMES is selected at bus 16 in area 2. The SMES has a specification of 80 MJ, 40 kA, 100 MVA [22].

Fig. 2 shows the SMES model with simultaneous active and reactive power (P–Q) modulation control scheme [22]. In the model, $K_P(s)$ and $K_Q(s)$ are the SMES active and reactive power controllers, respectively, which are represented by

$$K_P(s) = K_1 \frac{(1+T_{11}s)}{(1+T_{12}s)} \tag{1}$$

$$K_Q(s) = K_2 \frac{(1+T_{21}s)}{(1+T_{22}s)} \tag{2}$$

where, K_1 and K_2 are gains of active and reactive power controller; T_{11} and T_{12} are time constants of the active power controller; T_{21} and T_{22} are time constants of the reactive power controller. The input signals of active and reactive power controllers are active power deviation ΔP_{tie} and reactive power deviation ΔQ_{tie} in a tie-line between bus 13 and 15, respectively. In this paper, gains and time constants of both controllers are optimized by the proposed control design.

As shown in Fig. 2, $K_{Ism}(s)$ which is the SMES coil current controller, can be represented by

$$K_{Ism}(s) = \left(K_P + \frac{1}{T_i s}\right) K_{sm}(I_{sm} - I_{sm0}) \tag{3}$$

where, K_P is the proportional gain, T_i is the time constant (s), K_{sm} is a SMES coil controller gain; I_{sm} is a SMES coil current (pu); I_{sm0} is an initial value of SMES coil current (pu). In the SMES model, the effect of I_{sm} is considered, since the dynamic behavior of I_{sm} significantly affects the overall performance of SMES. In practice, I_{sm} is not allowed to reach zero to prevent the possibility of discontinuous conduction under unexpected disturbances. On the other hand, high I_{sm} which is above the maximum allowable limit, may lead to loss of superconducting properties. Based on the hardware operational constraints, the lower and upper coil current limits are considered and assigned as $0.30I_{sm0}$ and $1.38I_{sm0}$, respectively. Here, I_{sm} can be calculated from the PEI block which has a relation as

$$I_{sm} = \sqrt{I_{sm0}^2 - 2E_{out} \Big/ \left(L_{sm} I_{sm,base}^2\right)} \tag{4}$$

$$E_{out} = \int P_{sm} dt \cdot S_{sm,base} \tag{5}$$

where, E_{out} is the SMES energy output (J); L_{sm} is the SMES coil inductance (H); $I_{sm,base}$ is the SMES current base (A); P_{sm} is the SMES active power output and $S_{sm,base}$ is the SMES MVA base (MVA). Subsequently, the energy stored in a SMES unit (E_{sm}) and the initial energy stored (E_{sm0}) can be determined by

$$E_{sm} = E_{sm0} - E_{out} \tag{6}$$

$$E_{sm0} = 0.5 L_{sm} I_{sm0}^2 \cdot I_{sm,base}^2 \tag{7}$$

Besides, $K_V(s)$ which is the voltage controller, can be represented by

$$K_V(s) = K_{Vsm}(V_{t0} - V_{ts}) \tag{8}$$

where, K_{Vsm} is the controller gain; V_{t0} is an initial value of a terminal bus voltage of a SMES unit (pu); and V_{ts} is a bus voltage of SMES (pu).

The desired active and reactive power output of SMES (P_d and Q_d) can be expressed as

$$P_d = V_{ts} I_{sm} AP \tag{9}$$

$$Q_d = V_{ts} I_{sm} AQ \tag{10}$$

where, AP and AQ are the active and reactive power fractions, respectively. The SMES active and reactive power outputs (P_{sm} and Q_{sm}) are the output of the SMES controlled converter (CONV). The converter transfer function can be represented by the first-order time-lag compensator as

$$\text{CONV} = 1/(1 + T_c s) \tag{11}$$

where T_c is the time constant of converter (s).

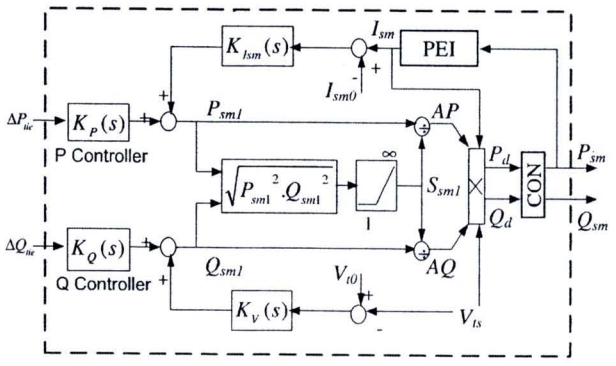

Fig. 2. SMES with active and reactive (P–Q) controllers.

3. Proposed robust SMES controller design

To enhance the robustness of active and reactive power controllers against system uncertainties, the inverse additive perturbation [19] is applied to formulate the optimization problem of controller parameters.

The feedback control system with inverse additive perturbation is depicted in Fig. 3. G is the nominal plant. K is the designed

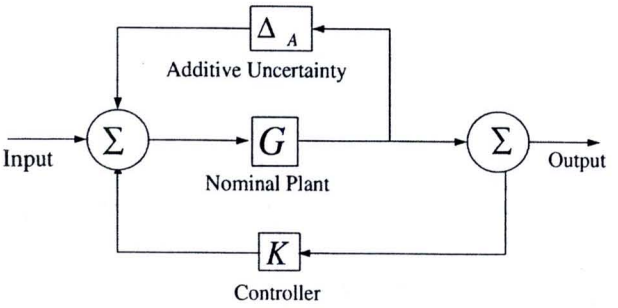

Fig. 3. Feedback system with inverse additive perturbation.

controller. For system uncertainties such as various generating and loading conditions, variation of system parameters and nonlinearities, etc., they are represented by Δ_A which is the unstructured additive uncertainty model. Based on the small gain theorem, for a stable additive uncertainty Δ_A, the system is stable if

$$|\Delta_A G/(1 - GK)| < 1 \tag{12}$$

Then,

$$|\Delta_A| < 1/|G/(1 - GK)| \tag{13}$$

The right hand side of (13) implies the size of system uncertainties or the robust stability margin against system uncertainties. By minimizing $|G/(1 - GK)|$, the robust stability margin of the closed-loop system is maximum. This concept can be applied as the optimization problem as

$$\begin{aligned} &\text{Minimize} && \|G/(1 - GK)\|_\infty \\ &\text{Subject to} && \zeta \geqslant \zeta_{spec}, \quad \sigma \geqslant \sigma_{spec} \\ & && K_{i,\min} \leqslant K_i \leqslant K_{i,\max} \\ & && T_{ij,\min} \leqslant T_{ij} \leqslant T_{ij,\max}, \quad i = 1,2, \quad j = 1,2 \end{aligned} \tag{14}$$

where $\| \bullet \|_\infty$ is the infinite norm of transfer function; ζ_{spec} and σ_{spec} are desired damping ratio and desired real part of the eigenvalue corresponding to the dominant inter-area oscillation mode, respectively. The objective of the optimization is not only to improve the robustness of the SMES but also to move the dominant inter-area oscillation modes to the *D*-stability region as shown in Fig. 4. This optimization problem is solved by GA.

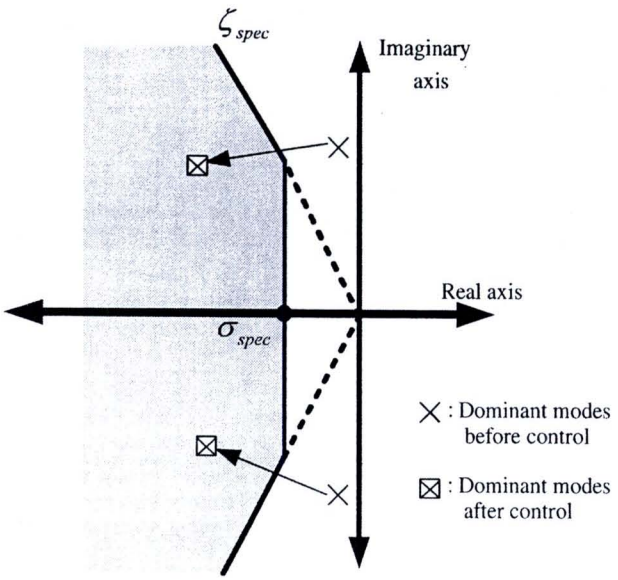

Fig. 4. *D*-Stability region.

4. Simulation studies

In the SMES model, the fixed parameters are set as follows:

$K_p = 40$, $T_i = 0.4$, $K_{sm} = 1$, $K_{Vsm} = 1$,
$T_c = 0.01$, $I_{sm0} = 0.6377$, $L_{sm} = 10$,
$S_{sm,base} = 100$ MVA, $V_{tbase} = 22$ kV, $V_{t0} = 0.95$

In the GA optimization [23], the ranges of search parameters are set as follows: $\zeta_{spec} = 0.1$, $\sigma_{spec} = -0.4$, K_1 and $K_2 \in [1 \quad 10]$, $T_{ij} \in [0.0001 \quad 1]$, population size = 100, crossover probability = 0.6, mutation probability = 0.05, maximum generation = 100. First, the linearized power system is formulated based on the normal operating condition of case 1 in Table 1. Optimizing control parameters in the linearized system by GA, the *P* and *Q* controllers of the robust SMES which is referred to as "RSMES", are obtained as

$$K_P(s) = 7.5\left(\frac{1 + 0.2092s}{1 + 0.2032s}\right) \tag{15}$$

$$K_Q(s) = 5.5\left(\frac{1 + 0.8576s}{1 + 0.3387s}\right) \tag{16}$$

The robustness of RSMES is compared with the SMES designed without considering the robustness which is referred as "CSMES" designed by the method proposed in [24]. CSMES is designed to yield the damping ratio and the real part of the dominant inter-area mode same as the design specification of RSMES. Based on [24], the optimization problem of CSMES is formulated as

$$\begin{aligned} &\text{Minimize} && J = \sum_{\zeta \leqslant \zeta_{spec}} |\zeta_{spec} - \zeta| + \sum_{\sigma \geqslant \sigma_{spec}} |\sigma_{spec} - \sigma| \\ &\text{Subject to} && K_{i,\min} \leqslant K_i \leqslant K_{i,\max} \\ & && T_{ij,\min} \leqslant T_{ij} \leqslant T_{ij,\max}, \quad i = 1,2, \quad j = 1,2 \end{aligned} \tag{17}$$

As a result, the active and reactive power controllers of CSMES are given by

$$K_{PC}(s) = 2.09\left(\frac{1 + 0.8216s}{1 + 0.0411s}\right) \tag{18}$$

$$K_{QC}(s) = 4.61\left(\frac{1 + 0.3053s}{1 + 0.2034s}\right) \tag{19}$$

Table 2 shows the eigenvalue and damping ratio of the dominant inter-area oscillation mode. Without SMES, the damping ratio of the oscillation mode is very poor. On the other hand, the desired damping ratio and the desired real part of the oscillation mode are achieved by both CSMES and RSMES.

Next, nonlinear simulations of three case studies in Table 1 are carried out under two patterns of wind power generations [PW1] and [PW2] as depicted in Fig. 5a and b. PW1 and PW2 of each pattern are injected to bus 4 and 14, respectively. Figs. 6 and 7 show the maximum tie-line power deviation in case of wind power generation patterns I and II, respectively. Without SMES, the maximum power deviation is very large especially in cases 2 and 3. In contrast, the maximum power deviation is effectively suppressed by SMES. However, CSMES is sensitive to operating conditions in cases 2 and 3. The maximum power deviation highly increases in cases 2 and 3. On the other hand, RSMES is very robust to any operating condition. The maximum power deviation rarely changes. Fig. 8 shows a sample result of tie-line power deviations of case 3 with wind power generation pattern II. Without SMES, the tie-line power severely fluctuates. On the contrary, the power fluctuation is alleviated by SMES. Nevertheless, RSMES provides more stabilizing effects than CSMES. These results signify that the stabilizing effect of RSMES against wind power fluctuations is superior to that of CSMES.

Next, simulation results with wind power generation pattern II and applied fault are shown as follows. In case 1, it is assumed that

Table 1
Case studies (Base = 900 MVA).

Case	1. Normal condition (P_{tie} = 1.5)	2. Heavy line flow (P_{tie} = 4.5)	3. Heavy line flow and weak line (P_{tie} = 4.5)
G1	P_G = 6.0	P_G = 7.5	P_G = 9.0
G2	P_G = 5.5	P_G = 6.0	P_G = 7.5
G3	P_G = 5.5	P_G = 4.5	P_G = 5.0
G4	P_G = 5.5	P_G = 4.0	P_G = 4.0
Load and line conditions	L_1 = 10, L_2 = 12	L_1 = 10, L_2 = 12	L_1 = 12, L_2 = 13 one line between bus 3 and 101 is opened

Note: P_G = Generation power (pu), L = Load power (pu).

Table 2
Eigenvalues of dominant inter-area mode.

Cases	Eigenvalue (damping ratio)
No SMES	$-0.107 \pm j\,4.066i$, $\zeta = 0.026$
CSMES	$-0.421 \pm j\,3.75i$, $\zeta = 0.120$
RSMES	$-0.667 \pm j\,3.38i$, $\zeta = 0.194$

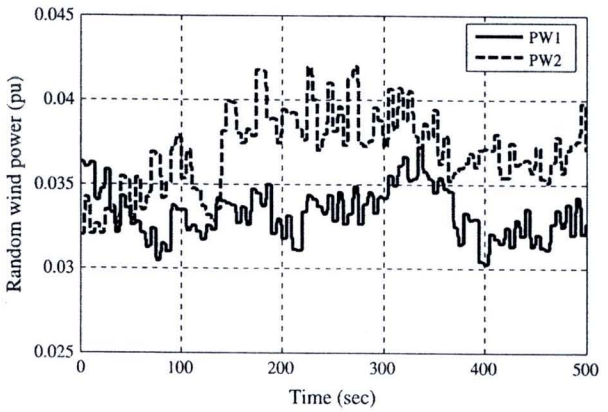

(a) Pattern I

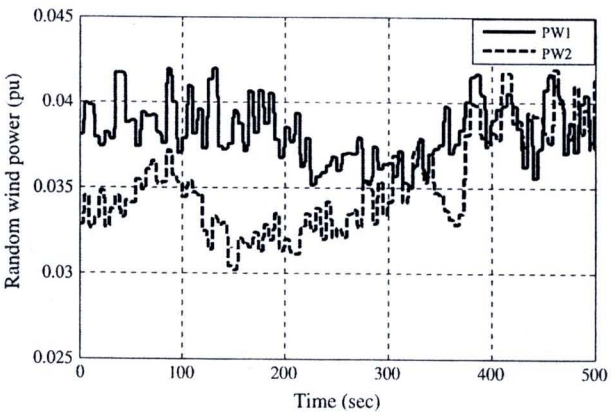

(b) Pattern II

Fig. 5. Wind power generations.

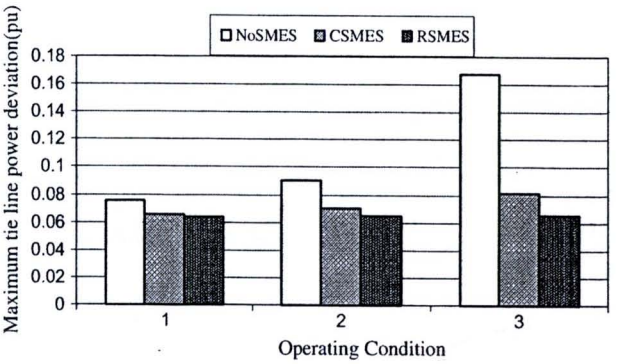

Fig. 6. Maximum tie-line power deviation in case of wind power pattern I.

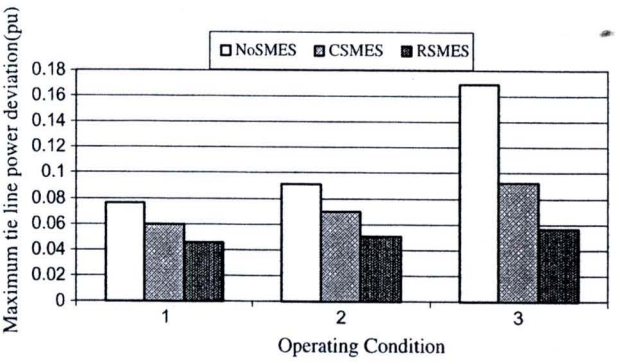

Fig. 7. Maximum tie-line power deviation in case of wind power pattern II.

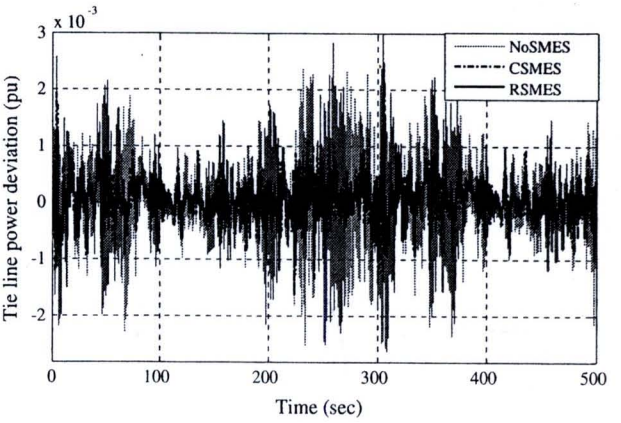

Fig. 8. Tie line power deviation in case 3 with wind power pattern II.

a 3ø fault occurs at the midpoint of one tie-line between bus 3 and 101 at 5.0 s. The fault is cleared 50 ms after. As shown in Fig. 9, the damping effect of RSMES on power oscillation is better than that of CSMES. In case 2 with the same 3ø fault, the stabilizing effect of CSMES is significantly deteriorated as illustrated in Fig. 10. The power oscillation takes long time to damp out. In contrast, RSMES is capable of stabilizing power oscillation. It still retains system stability successfully. In case 3, it is assumed that two parallel lines between bus 3 and 101 are operated from the beginning of simulation time at 0 s. At 5 s, one line of two parallel lines between bus 3 and 101 is suddenly opened and not re-closed. As depicted in Fig. 11, CSMES loses stabilizing effect. It is not able to damp

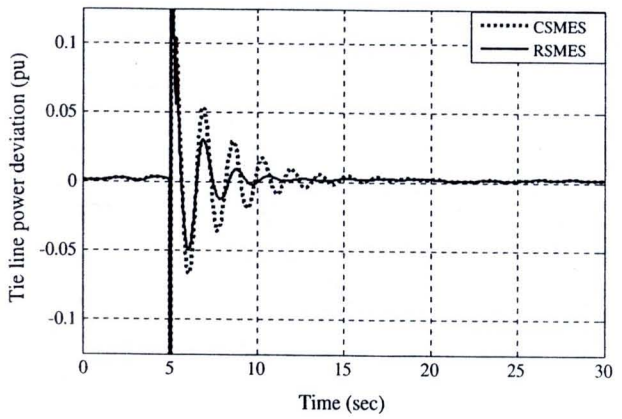

Fig. 9. Tie line power deviation in case 1 with fault and wind power pattern II.

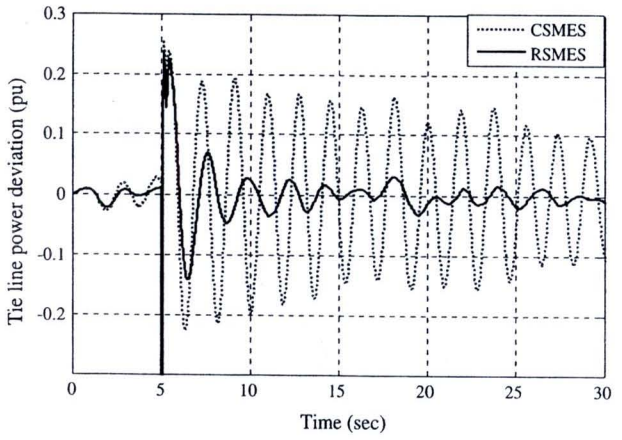

Fig. 10. Tie line power deviation in case 2 with fault and wind power pattern II.

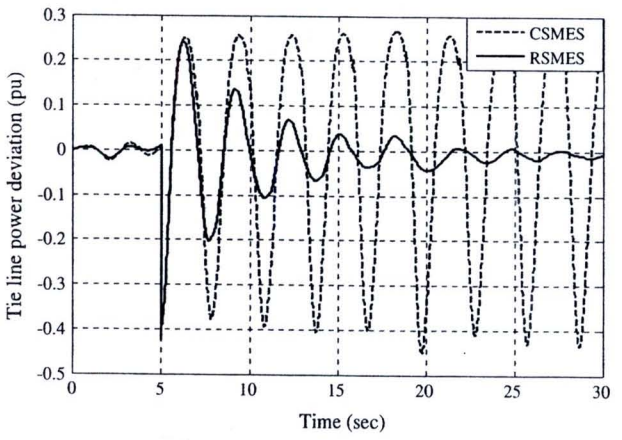

Fig. 11. Tie line power deviation in case 3 with fault and wind power pattern II.

out power oscillation. The system stability cannot be maintained. On the other hand, RSMES is very robust against this heavy load and weak line situation. The power oscillation can be stabilized effectively.

The SMES coil currents in case 3 with wind generation pattern II without fault are shown in Fig. 12, respectively. Both coil currents of CSMES and RSMES can properly remain within the allowable limits. However, the fluctuation of SMES current in case of RSMES is larger. This indicates that RSMES can appropriately supply and

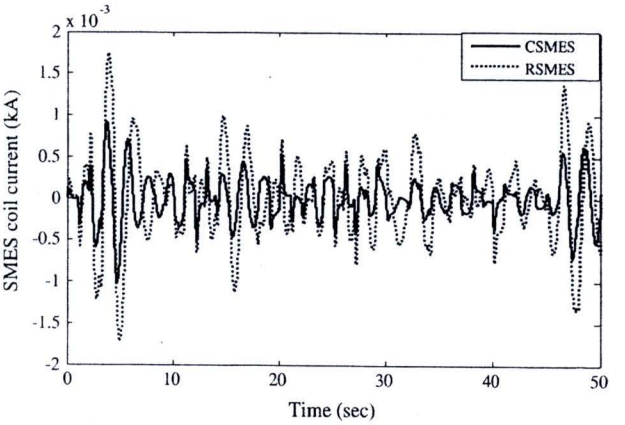

Fig. 12. SMES coil current in case 3 with wind power pattern II.

receive the larger amount of electrical energy with power system. Accordingly, the stabilizing effect of tie-line power flow by RSMES is superior to that of CSMES.

5. Conclusions

A robust SMES controller design based on inverse additive perturbation in interconnected power systems with wind farms has been proposed. The inverse additive perturbation model has been applied to represent unstructured system uncertainties. The control parameters of SMES active and reactive power controllers are optimized based on the enhancement of the robust stability margin against system uncertainties. Simulation studies confirm that the robustness of the proposed SMES under various situations such as heavy line flow, weak line, wind power fluctuations and system faults is much superior to that of the SMES designed without considering robustness.

Acknowledgements

This work was supported by the Thailand Research Fund under the Basic Research Grant No. BRG5080019 and the King Mongkut's Institute of Technology Ladkrabang Research Funds.

References

[1] Ackermann T. Wind power in power systems. John Wiley & Sons Ltd.; 2005.
[2] Slootweg JG, Kling WL. The impact of large scale wind power generation on power system oscillations. Electr Pow Syst Res 2003;67(1):9–20.
[3] Tripathy SC, Kalantar M, Balasubramanian R. Dynamics and stability of a hybrid wind–diesel power system. Energy Convers Manage 1992;33(12): 1063–72.
[4] Fernández RD, Mantz RJ, Battaiotto PE. Impact of wind farms on a power system. An eigenvalue analysis approach. Renew Energy 2007;32(10): 1676–88.
[5] Bansal RC, Bhatti TS, Kothari DP. On some of the design aspects of wind energy conversion systems. Energy Convers Manage 2002;43(16):2175–87.
[6] Fernandez RD, Battaiotto PE, Mantz RJ. Impact of wind farms voltage regulation on the stability of the network frequency. Int J Hydrogen Energy 2008;33(13): 3543–8.
[7] Boom RW, Perterson H. A superconducting energy storage for power systems. IEEE Trans Magn 1972;8:701–3.
[8] Boenig HJ, Hauer JF. Commissioning tests of the Bonneville Power administration 30 MJ superconducting magnetic energy storage unit. IEEE Trans Power Appl Syst 1985;10:302–9.
[9] Rabbani MG, Devotta JBX, Elangovan S. An adaptive fuzzy controlled superconducting magnetic energy storage unit for power systems. Energy Convers Manage 1998;39(9):931–42.
[10] Devotta JBX, Rabbani MG. Application of superconducting magnetic energy storage unit in multi-machine power systems. Energy Convers Manage 2000;41(5):493–504.
[11] Tripathy SC. Dynamic simulation of hybrid wind–diesel power generation system with superconducting magnetic energy storage. Energy Convers Manage 1997;38(9):919–30.

[12] Tripathy SC, Balasubramanian R, Chandramohanan Nair PS. Effect of superconducting magnetic energy storage on automatic generation control considering governor deadband and boiler dynamics. IEEE Trans Power Syst 1992;7(3):1266–73.
[13] Chu X, Jiang X, Lai Y, Wu X, Liu W. SMES control algorithms for improving customer power quality. IEEE Trans Appl Supercon 2001;11(1):1769–72.
[14] Devotta JBX, Rabbani MG, Elangovan S. Application of superconducting magnetic energy storage unit for damping of subsynchronous oscillations in power systems. Energy Convers Manage 1999;40(1):23–37.
[15] Abdelsalam MK, Boom RW, Perterson HA. Operation aspects of Superconducting Magnetic Energy Storage (SMES). IEEE Trans Magn 1987;23: 3275–7.
[16] Chen SS, Wang L, Lee WJ, Chen Z. Power flow control and damping enhancement of a large wind farm using a superconducting magnetic energy storage unit. IET Renew Power Gener 2009;3:23–38.
[17] Nomura S, Ohata Y, Hagita T, Tsutsui H, Tsuji-Iio S, Shimada R. Wind farms linked by SMES systems. IEEE Trans Appl Supercon 2005;15:1951–4.
[18] Shameem AL, Mairaj UDM. Power quality improvement of a stand-alone power system subjected to various disturbances. J Power Sources 2006;163:604–15.
[19] Gu P, Petkov Hr, Konstantinov MM. Robust control design with MATLAB. Springer; 2005.
[20] Kundur P. Power system stability and control. McGraw Hill; 1994.
[21] Martin N, Lima LTG. Determination of suitable locations for power system stabilizers and static var compensators for damping electromechanical oscillation in large power systems. IEEE Trans Power Syst 1990;5(4):1455–69.
[22] Dechanupaprittha S, Hongesombut K, Watanabe M, Mitani Y, Ngamroo I. A practical design of a fuzzy SMES controller based on synchronized phasor measurement for interconnected power systems. Int J Emerg Electric Power Syst 2008;9(3):5.
[23] Haupt RL, Hault SE. Practical genetic algorithm. 2nd ed. Wiley-interscience; 2004.
[24] Abdel-Magid YL, Abido MA. Optimal multiobjective design of robust power system stabilizers using genetic algorithms. IEEE Trans Power Syst 2003;18(3):1125–32.

IEEJ TRANSACTIONS ON ELECTRICAL AND ELECTRONIC ENGINEERING
IEEJ Trans 2010; 5: 000–000
Published online in Wiley InterScience (www.interscience.wiley.com). DOI:10.1002/tee.20556

Paper

Wide-Area Robust SMES Controller Design using Synchronized PMUs for Stabilization of Interconnected Power System with Wind Farms

AQ2

Issarachai Ngamroo*[a], Non-member•
Cuk Supriyadi Ali Nanda*, Non-member
Sanchai Dechanupaprittha**, Member
Masayuki Watanabe**, Member
Yasunori Mitani**, Member

The high penetration of wind power into interconnected power system may cause the severe problem of inter-area oscillations. To stabilize power oscillations, superconducting magnetic energy storage (SMES), which is capable of controlling active and reactive powers simultaneously, can be applied. To achieve the practical SMES controller design, this paper focuses on a robust SMES controller design based on wide-area synchronized phasor measurement units (PMUs) in an interconnected power system with wind farms. The structure of active and reactive power controllers of SMES is the first-order lead/lag compensator. Assuming that multiple PMUs are located in an interconnected power system, the steady-state phasor data are obtained by applying the small load perturbation. Using the phasor data, the simplified oscillation model (SOM) included with SMES power controllers can be identified and applied to estimate the dominant inter-area oscillation modes. In the design, unstructured system uncertainties such as various operating conditions, system parameters variation, random wind patterns, etc., are represented by the inverse additive perturbation. To enhance the system robust stability margin, the optimization of SMES control parameters is solved by genetic algorithm in the SOM. Simulation studies in the West Japan six-machine power system confirm that the robustness of the proposed SMES is much superior to that of the conventional SMES against various operating conditions. © 2010 Institute of Electrical Engineers of Japan. Published by John Wiley & Sons, Inc.

Keywords: wide-area stability and control, synchronized phasor measurement units, inter-area oscillations, superconducting magnetic energy storage, power system oscillations, robust control, system uncertainties, wind farms

AQ1 *Received 6 January 2009; Revised 6 June 2009•*

1. Introduction

Nowadays, the penetration of wind power into power systems has significantly increased because of its low impact on the environment and infinite availability. Nevertheless, wind power is unpredictable and intermittent in nature. The fluctuation of wind power generation may cause a severe problem of tie-line power oscillations [1,2]. Besides, the power oscillations due to wind power fluctuation may violate the transmission capability margin and deteriorate the system stability [3,4].

To stabilize the inter-area oscillation, superconducting magnetic energy storage (SMES), which is able to supply and absorb active and reactive power simultaneously [5,6], can be applied. In the past, an SMES unit has been successfully applied to improve system stability and stabilize power oscillations due to wind power fluctuations [7,8]. Nevertheless, the SMES power controllers proposed in these works have been designed in detailed power systems with the requirement of all system parameters and exact mathematical models. This makes the design difficult, inflexible, and impractical for actual systems. In addition, system uncertainties such as a deregulated environment with complex power contracts, various generating and loading conditions, system parameter variation and unpredictable wind power fluctuations, etc. have not been considered in the SMES controller design, and so the robustness of SMES controller against such system uncertainties cannot be guaranteed. As a result, the stabilizing effect of SMES on the inter-area power oscillation is significantly deteriorated under some operating conditions. To tackle these problems, a proper grasp of the present system state with the wide-area monitoring in combination with the robust control theory becomes the key issue to keep the power system stability successfully.

Recently, the wide-area monitoring of power systems using multiple phasor measurement units (PMUs) which are synchronized by the global positioning system (GPS) [9,10], have been applied to power systems such as transmission capacity enhancement [11], wide-area protection and emergency control [12], wide-area stabilization [13,14] etc. Synchronized PMUs with GPS provide the opportunity of data synchronization at a common time reference with high accuracy. Moreover, oscillation modes, especially the inter-area low-frequency oscillation mode with poor damping, can be detected from PMU data by modeling as a simplified oscillation model (SOM) [14].

This paper applies the wide-area synchronized phasor measurements to design the robust power controllers of SMES in an interconnected power system with large wind farms. The configuration of both active and reactive power controllers is a practical lead/lag compensator. Assuming that multiple PMUs have been located in the power system, the steady-state phasor data can be obtained by applying a small load perturbation to some load buses. DFT filtering is applied to extract the time series signal embedded with the dominant inter-area oscillation modes from the phasor data. The extracted signal is used for system identification and to

[a] Correspondence to: Issarachai Ngamroo. E-mail: ngamroo@gmail.com

* Center of Excellence for Innovative Energy Systems (CInES), King Mongkut's Institute of Technology Ladkrabang (KMITL), Bangkok 10520, Thailand

** Department of Electrical Engineering, Graduate School of Engineering, Kyushu Institute of Technology, Fukuoka 804-8550, Japan

construct the SOM embedded with the dominant modes. In addition, by integrating the SMES controllers into the SOM, control parameters can be tuned. To enhance the robustness of SMES against system uncertainties, the inverse additive perturbation [15] is applied to represent unstructured system uncertainties such as various generating and loading conditions, system parameters variation, etc., and included in the SOM. The optimization problem of SMES control parameters is formulated on the basis of an enhancement of the system robust stability margin. To achieve the SMES parameters automatically, the genetic algorithm (GA) is applied to solve the problem. Nonlinear simulation study is carried out by the Dymola software package with ObjectStab [16]. Simulation results in the West Japan six-machine interconnected power system confirm that the robustness of the proposed SMES is much superior to that of the conventional SMES designed without considering robustness under heavy tie-line power flow, weak line, random wind patterns, and severe faults.

2. Problem Formulation

2.1. Study system The six-area interconnected power system [17] is used as the study system as depicted in Fig. 1. This system represents the 60-Hz interconnected areas of Western Japan. The area capacity ratio of areas 1 to 6 is 20:13:7:40:7:33 with a 1000-MVA base. Assume that the wind farms located in area 1 have the maximum generation capacity of 500 MW. Normally, the electric power is transferred from areas 1 to 6. For the study purpose, it is assumed that power flows in tie-lines are in the heavy condition and the system disturbances such as line faults, load fluctuations, etc. occasionally occur. These situations cause inter-area oscillations with poor damping. Based on modal analysis results in Ref. 18, two inter-area oscillation modes tend to be dominant and interact with each other in this system. One of the modes is associated with the oscillation between both end generators (G1 and G6), while the other mode is associated between both end and middle generators (G1 and G4, G4 and G6). To stabilize both oscillation modes, an SMES is applied. Using the residue method in Ref. 19, buses 1 and 6 are the most effective locations of SMES for power system stabilization. As a result, an SMES is placed at buses 1 and 6. The SMES has specifications 800 MJ, 40 kA, 1000 MVA [18].

To install the PMU, two observation sites at buses 1 and 6 which significantly participate in these two modes are selected, while another site of PMU at bus 14 is used as the reference of the phase angle. Note that phasor data are stored with the observed time using PMUs synchronized by the GPS signal. Therefore, the measured phasor data are directly comparable with each other without considering the delay in communication. In this study, small load variations at some load buses are assumed to simulate the phasor fluctuations measured in the power system.

2.2. SMES model Figure 2 shows the SMES model with simultaneous active and reactive power (P–Q) controllers

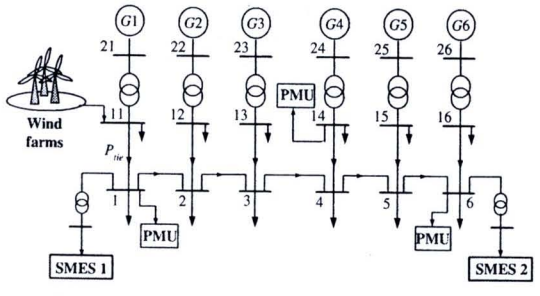

Fig. 1. Six-area interconnected power system with wind farms

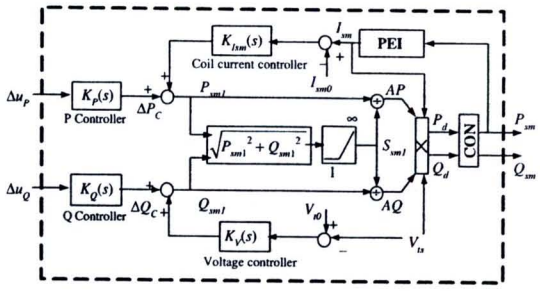

Fig. 2. SMES with active and reactive (P–Q) controllers

[18]. In the model, $K_P(s)$ and $K_Q(s)$ are represented by

$$K_P(s) = K_{PD}\left(\frac{1+T_{P1}s}{1+T_{P2}s}\right) \tag{1}$$

$$K_Q(s) = K_{QD}\left(\frac{1+T_{Q1}s}{1+T_{Q2}s}\right) \tag{2}$$

where $K_P(s)$ and $K_Q(s)$ are active and reactive power controllers, respectively; K_{PD}, K_{QD} are controller gains; and T_{P1}, T_{P2}, T_{Q1}, T_{Q2} are time constants. The input signals of active power controller (Δu_P) and reactive power controller (Δu_Q) of SMES1 and SMES2 are the active power deviation (ΔP_{tie}) and reactive power deviation (ΔQ_{tie}) in a tie line from bus 11 to bus 1 and from bus 16 to bus 6, respectively. Here, gains and time constants of both controllers are optimized by the proposed design method. As shown in Fig. 2, the SMES coil current controller $K_{Ism}(s)$, which is a proportional integral (PI) controller, can be represented by

$$K_{I\text{sm}}(s) = \left(K_P + \frac{1}{T_I s}\right) K_{\text{sm}}(I_{\text{sm}} - I_{\text{sm0}}) \tag{3}$$

where K_P and T_I are the proportional gain and the time constant of PI controller, K_{sm} is the gain of SMES coil controller, I_{sm} is the SMES coil current (pu), and I_{sm0} is the initial coil current. In the SMES model, the effect of I_{sm} is considered, since the dynamic behavior of I_{sm} significantly affects the overall performance of SMES. In practice, I_{sm} is not allowed to reach zero to prevent the possibility of discontinuous conduction under unexpected disturbances. On the other hand, high I_{sm} which is above the maximum allowable limit may lead to loss of superconducting properties. Based on the hardware operational constraints, the lower and upper coil current limits are considered and assigned as $0.30I_{\text{sm0}}$ and $1.38I_{\text{sm0}}$, respectively. Here, I_{sm} can be calculated from the •PEI block which has a relation

$$I_{\text{sm}} = \sqrt{I_{\text{sm0}}^2 - \frac{2E_{\text{out}}}{L_{\text{sm}} I_{\text{sm,base}}^2}} \tag{4}$$

$$E_{\text{out}} = \left(\int P_{\text{sm}} \mathrm{d}t\right) S_{\text{sm,base}} \tag{5}$$

where E_{out} is the SMES energy output (J), L_{sm} is the SMES coil inductance (H), $I_{\text{sm,base}}$ is the SMES current base (A), P_{sm} is the SMES active power output (pu), Q_{sm} is the SMES reactive power output (pu), and $S_{\text{sm,base}}$ is the SMES MVA base. Subsequently, the energy stored in a SMES unit and the initial energy stored can be determined by

$$E_{\text{sm}} = E_{\text{sm0}} - E_{\text{out}} \tag{6}$$

$$E_{\text{sm0}} = 0.5 L_{\text{sm}} I_{\text{sm0}}^2 \cdot I_{\text{sm,base}}^2 \tag{7}$$

where E_{sm} is the energy stored in a SMES unit (J) and E_{sm0} is the initial stored energy. Besides, $K_V(s)$ can be represented by

$$K_V(s) = K_{V\text{sm}}(V_{t0} - V_{ts}) \tag{8}$$

where K_{Vsm} is the gain of SMES voltage controller, V_{t0} is the initial value of a terminal bus voltage of a SMES unit (pu), and V_{ts}

is the bus voltage of SMES (pu). The desired active and reactive power outputs of SMES can be expressed as

$$P_d = V_{ts} I_{\mathrm{sm}} AP \tag{9}$$

$$Q_d = V_{ts} I_{\mathrm{sm}} AQ \tag{10}$$

where P_d is the desired active power output of SMES (pu), Q_d is the desired reactive power output of SMES (pu), AP is the active power fraction, *and* AQ is the reactive power fraction. In Fig. 2, P_{sm} and Q_{sm} are the output of the SMES controlled converter (CONV). The converter transfer function can be represented by the first-order time-lag compensator as

$$CONV = 1/(1 + T_c s) \tag{11}$$

where T_c is the time constant of converter(s).

3. Proposed Control Design

An overview of the control design is depicted in Fig. 3. Based on the synchronized PMUs, the dominant inter-area oscillation modes can be identified by modeling the measured oscillation data as an SOM. Besides, the SOM can be extended to include the effects of P–Q controllers of SMES. By tuning the controller parameters by GA in the extended SOM, the damping of the dominant modes and the robustness of the SMES controllers against system uncertainties can be improved. The effect of the designed controller can be evaluated in the power system with the detailed model. The proposed designed method is described as follows.

3.1. Modal analysis with SOM The power swing equations of generators in an n-machine power system are represented by [20]:

$$M_i \dot{\omega}_i = -D_i(\omega_i - 1) + P_{mi} + P_{ei} \tag{12}$$

$$\dot{\delta}_i = \omega_r(\omega_i - 1) \tag{13}$$

where $i = 1, 2, \ldots, n$; ω_i is the angular velocity of generator i; δ_i is the rotor angle of generator i; M is the inertia constant; D is the damping coefficient, P_m is the mechanical input to the generator, P_e is the electrical output, $\omega_r = 2\pi f$ is the rated angular velocity, f is the system frequency; and '$\cdot$' is the derivative of variable with respect to time.

The number of oscillation modes to be considered for applying SOM depends on the number of dominant modes in the target system. The SOM can be extended to represent the system with any number of oscillations modes. This makes the SOM general, practical, and robust. Based on simulation results in Section 4, it can be observed that two dominant inter-area oscillation modes always occur at various operating conditions in this system.

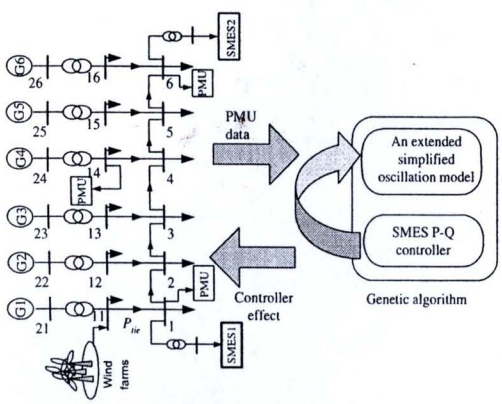

Fig. 3. Controller design overview

Accordingly, the SOM is used to represent the interaction of two dominant inter-area oscillation modes. These modes are assumed to oscillate in keeping with the dynamics of power swing equations. The first SOM corresponds to the most dominant mode, while the other corresponds to the second dominant mode. The dynamic of SOM is represented by the polynomial approximation of the phase angle and the angular velocity as follows.

$$\dot{x}_1 = \frac{\omega_r}{M_1}(-D_1(\omega_1 - 1) + P_{m1} - P_{e1}) \tag{14}$$

$$\approx F_1(x_1, x_2, x_3, x_4) \tag{15}$$

$$\dot{x}_2 = x_1 \tag{16}$$

$$\dot{x}_3 = \frac{\omega_r}{M_2}(-D_2(\omega_2 - 1) + P_{m2} - P_{e2}) \tag{17}$$

$$\approx F_2(x_1, x_2, x_3, x_4) \tag{18}$$

$$\dot{x}_4 = x_3 \tag{19}$$

where, F_1 and F_2 are assumed to consist of linear terms. Equations (14)–(19) can be represented in the matrix form as:

$$\begin{bmatrix} \dot{x}_1 \\ \dot{x}_2 \\ \dot{x}_3 \\ \dot{x}_4 \end{bmatrix} = \begin{bmatrix} a_1 & a_2 & a_3 & a_4 \\ 1 & 0 & 0 & 0 \\ b_1 & b_2 & b_3 & b_4 \\ 0 & 0 & 1 & 0 \end{bmatrix} \begin{bmatrix} x_1 \\ x_2 \\ x_3 \\ x_4 \end{bmatrix} \tag{20}$$

where $x_1 = \dot{\delta}_1 - \dot{\delta}_s$; $x_2 = \delta_1 - \delta_s - (\delta_{1e} - \delta_{se})$; $x_3 = \dot{\delta}_2 - \dot{\delta}_s$; $x_4 = \delta_2 - \delta_s - (\delta_{2e} - \delta_{se})$. Subscripts 1 and 2 of δ denote numbers of selected sites, the subscripts s denotes the reference size, and the subscript e denotes the initial value of the phase angle. The coefficients a_i and b_i $(i = 1\text{–}4)$ can be evaluated by applying the least-squares method to time series datasets of x_j $(j = 1\text{–}4)$ obtained from the wide-area phasor measurement. Oscillation characteristics are directly investigated by •(20) since eigenvalues of the coefficient matrix represent the damping and frequency of two oscillatory modes. Note that not only a longitudinal interconnected power system is considered here; the SOM is applicable to other systems with any structure where the oscillatory characteristics are observed. In addition, the SOM can be extended to the system with more than two dominant modes: that is, by increasing state variables and choosing the corresponding sites according to the number of the dominant modes.

By applying the small load changes at load buses 4, 11, and 16, the phase difference between buses 1 and 14 as well as buses 6 and 14 can be measured by PMUs as shown in Fig. 4. Applying fast Fourier transform (FFT) to the phase difference data shows two dominant frequencies of inter-area oscillation modes. On the other hand, the phase difference data include many frequency components associated with inter-area oscillations, local oscillations, and many noises. To extract the dominant inter-area mode frequency (f_c) from the measured phase difference data, the DFT filtering is applied as shown in Fig. 5. Initially, the measured phase difference data in Fig. 5(a) are filtered by a DFT filter with a bandwidth of 0.2–0.8 Hz. As a result, the considered frequency of dominant modes 1 and 2 (f_{c1} and f_{c2}) can be evaluated as shown in Fig. 5(b).

Subsequently, the bandwidths of $f_{c1} \pm 0.1$ and $f_{c2} \pm 0.1$ Hz are extracted to obtain the inter-area oscillation frequency component as depicted in Fig. 5(c). By applying the inverse discrete Fourier transform (IDFT) to the inter-area component, the signal embedded with inter-area oscillation can be achieved as shown in Fig. 5(d). Meanwhile, the unwanted frequency components such as local oscillation data and noises with higher frequencies can be eliminated. Consequently, the coefficient matrix of (20) can be evaluated by applying the least-squares method to the time series dataset, which includes mostly the considered inter-area frequency component. Thus, the damping characteristic of the dominant inter-area modes can be evaluated from the SOM.

AQ4

Color Figure - Online only

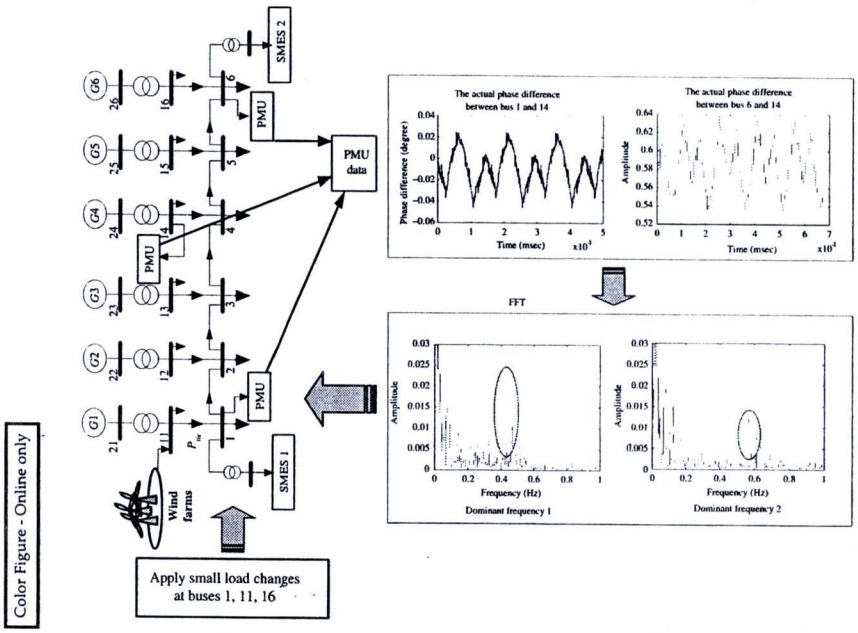

Fig. 4. Dominant mode verification by FFT analysis

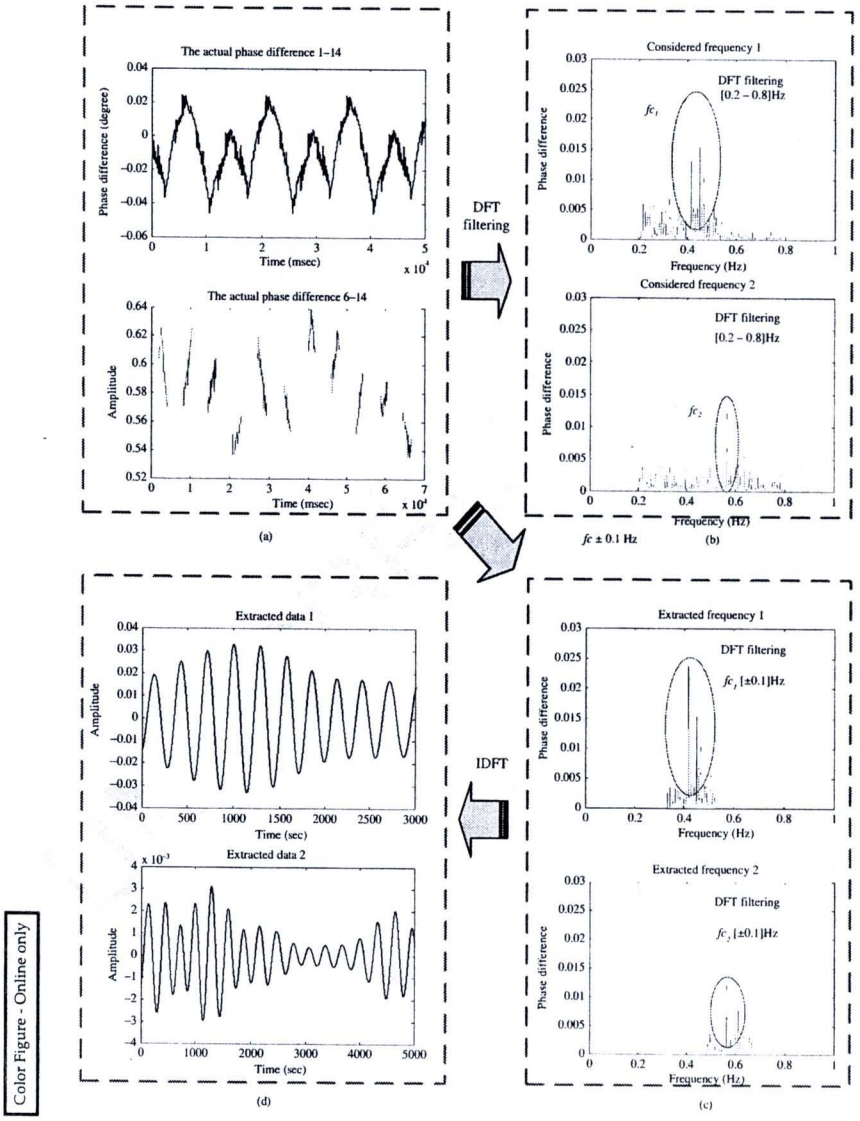

Fig. 5. Extraction of considered frequency component by DFT filtering

3.2. Extended SOM including SMES controller effects

Here, the SOM is extended to include the effect of SMES controller. The output signal of SMES power controller can be expressed by

$$\Delta P_C = K_P(s)\Delta u_P \tag{21}$$

$$\Delta Q_C = K_Q(s)\Delta u_Q \tag{22}$$

where ΔP_C and ΔQ_C are the output signals of the active and reactive power controllers, respectively. Thus, the SOM (20) is modified to include state variables of SMES controllers. As a result, the extended SOM can be expressed as

$$\begin{bmatrix} \dot{x}_1 \\ \dot{x}_2 \\ \dot{x}_3 \\ \dot{x}_4 \\ \dot{x}_{P1} \\ \dot{x}_{P2} \\ \dot{x}_{Q1} \\ \dot{x}_{Q2} \end{bmatrix} = \begin{bmatrix} a'_1 & a'_2 & a'_3 & a'_4 & a'_5 & a'_6 & a'_7 & a'_8 \\ 1 & 0 & 0 & 0 & 0 & 0 & 0 & 0 \\ b'_1 & b'_2 & b'_3 & b'_4 & b'_5 & b'_6 & b'_7 & b'_8 \\ 0 & 0 & 1 & 0 & 0 & 0 & 0 & 0 \\ c_1 & c_2 & c_3 & c_4 & c_5 & c_6 & c_7 & c_8 \\ d_1 & d_2 & d_3 & d_4 & d_5 & d_6 & d_7 & d_8 \\ e_1 & e_2 & e_3 & e_4 & e_5 & e_6 & e_7 & e_8 \\ f_1 & f_2 & f_3 & f_4 & f_5 & f_6 & f_7 & f_8 \end{bmatrix} \begin{bmatrix} x_1 \\ x_2 \\ x_3 \\ x_4 \\ x_{P1} \\ x_{P2} \\ x_{Q1} \\ x_{Q2} \end{bmatrix} \tag{23}$$

The state variables x_2 and x_4 are directly measured by PMUs, while x_1 and x_3 can be calculated from (16) and (19), respectively. The coefficients a'_i and b'_i, $i = 1, \ldots, 8$, can be determined by the least-squares method. The characteristics of a power system including SMES controllers can be estimated by (23). The coefficients c_i and $e_i, i = 1, \ldots, 8$, can be derived in terms of K_{PD}, T_{P1}, T_{P2} of SMES1 and SMES2, respectively. The coefficients d_i and $f_i, i = 1, \ldots, 8$, can be derived in terms of K_{QD}, T_{Q1}, T_{Q2} of SMES1 and SMES2, respectively. The desired damping of the dominant modes can be evaluated by eigenvalues of the coefficient matrix in (23). Control parameters of two SMESs are tuned on the basis of the extended SOM (23) since c_i, d_i, e_i, and f_i include the parameters of SMES. Accordingly, the change of SMES parameters affects eigenvalues directly. Tuned parameter sets are expected to stabilize at least two modes, although they cannot be the optimum sets. The effectiveness of tuning can be assessed more properly by evaluating the eigenvalues of (23) again after the tuned SMES is applied. Note that, without the requirement of the exact system modeling and parameters, the SMES control parameters can be tuned in the SOM with oscillation data from PMU. This makes the design more flexible and significantly reduces the computation time in comparison to the conventional SMES design. Additionally, the advantage of the proposed method is that steady-state phasor fluctuations are available for identifying the dominant modes in the normal condition, tuning the SMES parameters, and evaluating the effect of tuned SMES parameters. In other words, large disturbances such as line faults are not necessary for the identification of dominant modes. The identification process does not require the information of an input to the system for perturbation, while ordinary methods based on the system identification require both input and output of the system [21,22]. In addition, it can be observed that state variables of coil current controller and CONV have not been included in the SOM. This is because the dynamic characteristics of both components are already included in the measured phase difference data obtained from PMUs. Therefore, the dynamics of both components have been taken into account in the control design by SOM.

3.3. Parameters optimization of SMES

To enhance the robustness of SMES controllers against system uncertainties such as various generating and loading conditions, unpredictable network structures, variations of system parameters, random wind power generations, etc., the inverse additive perturbation [15] is applied to represent such unstructured system uncertainties.

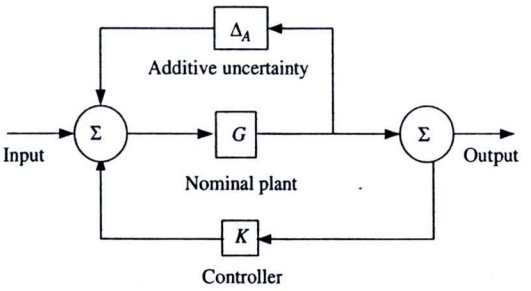

Fig. 6. Feedback system with inverse additive perturbation

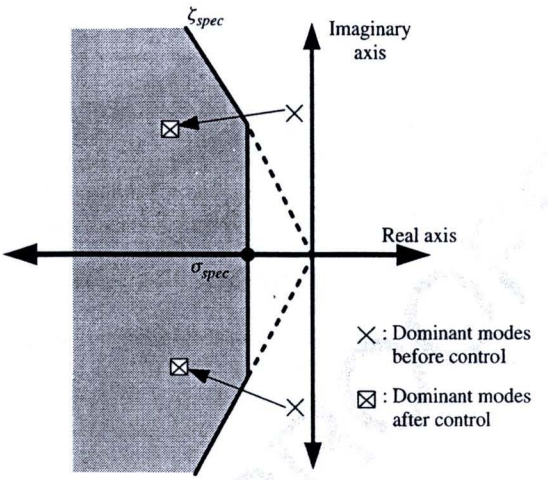

Fig. 7. D-stability region

The feedback control system with inverse additive perturbation is shown in Fig. 6. G is the nominal plant. K is the designed controller. For unstructured system uncertainties, they are represented by Δ_A, which is the additive uncertainty model. Based on the small gain theorem, for a stable additive uncertainty Δ_A, the system is stable if

$$|\Delta_A G/(1 - GK)| < 1 \tag{24}$$

$$\text{Then } |\Delta_A| < 1/|G/(1 - GK)| \tag{25}$$

The right-hand side of (25) implies the size of system uncertainties or the robust stability margin against system uncertainties. By minimizing $|G/(1 - GK)|$, the robust stability margin of the closed-loop system becomes maximum. In order to enhance the system damping, the dominant inter-area modes are designed to move to the D-stability region with the specified damping ratio ζ_{spec} and the specified real part σ_{spec} as shown in Fig. 7.

Based on this concept, the optimization problem of SMES control parameters can be formulated as

$$\text{Minimize } ||G/(1 - GK)||_\infty \tag{26}$$

$$\text{subject to } \zeta \geq \zeta_{\text{spec}},\ \sigma \geq \sigma_{\text{spec}}$$

$$K_{PD,\min} \leq K_{PD} \leq K_{PD,\max},$$

$$K_{QD,\min} \leq K_{QD} \leq K_{QD,\max},$$

$$T_{P,\min} \leq T_P \leq T_{P,\max}, T_{Q,\min} \leq T_Q \leq T_{Q,\max}$$

where $||\cdot||_\infty$ is the infinite norm of transfer function, ζ is the actual damping ratio of the dominant mode, σ is the actual real part of the eigenvalues corresponding to the dominant modes, $K_{PD,\max}$ and $K_{PD,\min}$ are the maximum and minimum gains of active power controller, respectively, $K_{QD,\max}$ and $K_{QD,\min}$ are the maximum and minimum gains of reactive power controller, respectively, $T_{P,\max}$ and $T_{P,\min}$ are the maximum and minimum

Table I. SMES parameters

Capacity: 800 MJ (220 kWh), 40 kA, 1000 MVA
$K_p = 40$, $T_i = 0.4$, $K_{sm} = 1.0$, $K_{Vsm} = 1.0$, $T_c = 0.01$, $I_{sm0} = 0.675$ pu, $L_{sm} = 10.0$ H, $S_{sm,base} = 1000$ MVA, $V_{tbase} = 25$ kV, $V_{t0} = 0.95$ pu

time constants of active power controller, respectively, and $T_{Q,\max}$ and $T_{Q,\min}$ are the maximum and minimum time constants of the reactive power controller, respectively. This optimization problem is solved by GA [23].

4. Simulation Study

The parameters of SMES model in Fig. 2 are given in Table I. Simulation study is carried out on the basis of five case studies in Table II. By applying FFT to phase difference between bus 1 and bus 6 under five cases, it can be observed in Fig. 8 that two dominant modes (first mode and second mode) always appear in the study system. Therefore, the SOM is applied to represent these two dominant modes. The proposed SMES is designed to improve the damping of these two modes.

The proposed control design is developed by MATLAB programming. The search parameters for GA are set as follows: $K_{PD,\min}$ and $K_{QD,\min} = 0.1$, $K_{PD,\max}$ and $K_{QD,\max} = 10.0$, $T_{P,\min}$ and $T_{Q,\min} = 0.01$, $T_{P,\max}$ and $T_{Q,\max} = 1.0$, $\zeta_{spec} = 0.045$, $\sigma_{spec} = -0.25$, crossover probability $= 0.9$, mutation probability $= 0.1$ and maximum generation $= 100$. Based on the operating condition in case 1, the designed robust P and Q controllers of SMES, which is referred to as •RSMES, are obtained as

AQ5

$$RSMES1: \quad K_{P1}(s) = 4.7524\frac{(0.7853s+1)}{(0.1976s+1)} \qquad K_{Q1}(s) = 6.4432\frac{(0.7658s+1)}{(0.2619s+1)} \tag{27}$$

$$RSMES2: \quad K_{P2}(s) = 3.1725\frac{(0.8277s+1)}{(0.1935s+1)} \qquad K_{Q2}(s) = 7.3942\frac{(0.7580s+1)}{(0.2685s+1)} \tag{28}$$

The robustness of RSMES is compared with the SMES designed without considering the robustness, which is referred to as 'CSMES'. Same as in previous research works, CSMES is designed in the detailed power system model to yield the damping ratio and the real part of the dominant modes the same as the design specification of RSMES. Based on [24], the optimization problem of CSMES is formulated as

$$\text{Minimize} \sum_{\zeta \le \zeta_{spec}} |\zeta_{spec} - \zeta| + \sum_{\sigma \ge \sigma_{spec}} |\sigma_{spec} - \sigma| \tag{29}$$

$$\text{subject to } K_{PD,\min} \le K_{PD} \le K_{PD,\max}, \quad K_{QD,\min} \le K_{QD} \le K_{QD,\max}, \quad T_{P,\min} \le T_P \le T_{P,\max}, T_{Q,\min} \le T_Q \le T_{Q,\max}$$

Note that the objective of the optimization problem (29) is to move the dominant modes to the D-stability region as shown in Fig. 7. Solving (29) by GA, the active and reactive power controllers of CSMES based on the same condition in case 1 are obtained as

$$CSMES1: \quad K_{P1}(s) = 5.6967\frac{(0.2971s+1)}{(0.1885s+1)} \qquad K_{Q1}(s) = 5.6167\frac{(0.9758s+1)}{(0.7819s+1)} \tag{30}$$

$$CSMES2: \quad K_{P2}(s) = 4.8728\frac{(0.9027s+1)}{(0.5910s+1)} \qquad K_{Q2}(s) = 7.4551\frac{(0.7457s+1)}{(0.4894s+1)} \tag{31}$$

It should be note that both RSMES and CSMES are designed under case 1, which is assumed to be the nominal operating condition of the study system. In other words, this power system always operates at this condition. For severe operating conditions in cases 2–5, it is assumed that they rarely occur in this system. Therefore, it is a good engineering practice to design a controller at a nominal operating condition. The designed controller can achieve its control objective for a wide range of time operation. Nevertheless, to evaluate and compare whether CSMES and RSMES can work well and tolerate severe operating conditions, simulation studies in cases 2–5 will be carried out.

Next the effective frequency band of designed controllers of CSMES and RSMES is compared. For example, the frequency band $K_{p1}(s)$ can be calculated by

$$\text{CSMES: Frequency band} = (1/0.1885)/2\pi - (1/0.2971)/2\pi = 0.83 - 0.53 = 0.30$$

$$\text{RSMES: Frequency band} = (1/0.1976)/2\pi - (1/0.7853)/2\pi = 0.80 - 0.20 = 0.60$$

From the calculation results, the effective frequency band of CSMES is found to be narrower than that of RSMES. Although better damping can be obtained by tuning the CSMES gain to be larger, the robustness of CSMES controller may be deteriorated. This occurs because the tuning of CSMES controller does not take the trade-off between damping performance and robustness into account. On the other hand, because the RSMES controller is optimized based on the frequency-domain-based objective function $||G/(1-GK)||_\infty$ and specified damping ratio constraint, the robustness and damping performance has been considered simultaneously. This results in a wider effective frequency band as well as a better damping effect of the RSMES controller.

In the simulation study, each generator is represented by a fifth-order model [20] and is equipped with a simplified exciter [25] and

Table II. Operating conditions (1000 MVA base)

Case	P_{tie}(pu)	Network condition	Applied disturbance in nonlinear simulation
1	2.3	No change	Temporary three-phase fault to ground at bus 2 at $t = 5$ s for 50 ms and is cleared naturally
2	3.0	No change	Same as case 1
3	3.0	One circuit of line 2–3 is opened	Same as case 1
4	4.0	No change	Same as case 1
5	4.0	One circuit of line 2–3 is opened	Temporary three-phase fault to ground at bus 6 at $t = 5$ s for 50 ms and is cleared naturally

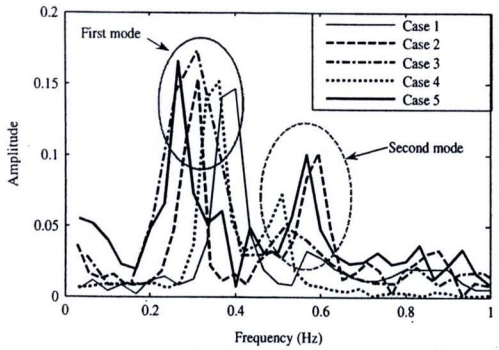

Fig. 8. FFT results of phase difference in cases 1–5

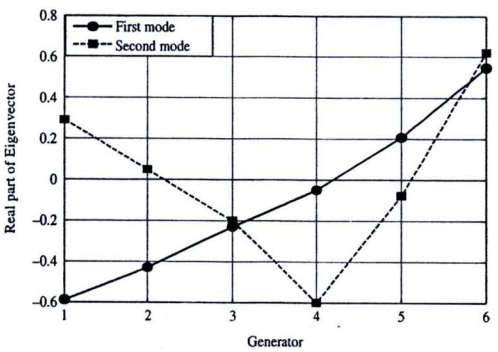

Fig. 10. Mode shapes of dominant modes 1 and 2

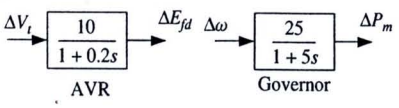

Fig. 9. AVR and governor models

a governor [25] as shown in Fig. 9, where ΔV_t is the generator terminal voltage deviation, ΔE_{fd} is the field voltage deviation, $\Delta\omega$ is the generator speed deviation, and ΔP_m is the mechanical power deviation. Note that the governor model is simplified from the detailed governor model of thermal and nuclear power plants [17].

Applying the designed CSMES and RSMES to the power system with a full, detailed model, the eigenvalues and damping ratios of two dominant inter-area modes for five case studies can be calculated as shown in Table III. Here, the first and second modes are initially defined from the eigenvalues $-0.074 \pm j2.713$ and $-0.104 \pm j3.679$, respectively, in case 1 with no SMES. Without SMES, the damping ratios of two modes are very poor in case 1 and become negative in cases 2–5 with heavy tie-line flow. However, both oscillation modes are stabilized by both CSMES and RSMES in cases 1–4. In case 5 with heavy line flow and weak line condition, CSMES loses the stabilizing effect and the first mode becomes unstable. On the other hand, RSMES is robustly capable of damping both oscillation modes. Figure 10 shows the real part of the right eigenvectors corresponding to the generator rotor angle, which implies the mode shape. This shows that mode 1 oscillates in the opposite direction between both end generators 1 and 6, while mode 2 oscillates between both end generators 1, 6 and the middle generator 4.

It should be noted that even though the RSMES is designed in the simplified model, it also has the same damping effect as the CSMES designed in the full model. However, the CSMES design requires an accurate mathematical model and exact system parameters which may not be available in practice. On the other hand, the RSMES can be designed with the simplified model by phase difference data. Without the full knowledge of system parameters and exact modeling, the proposed design can be easily implemented in the actual power system.

Table IV. Values of $||G/(1-GK)||_\infty$

Case	CSMES	RSMES
1	7.66	4.24
2	11.82	6.53
3	13.90	7.25
4	16.36	8.39
5	19.45	10.67

Based on (25), the robustness of system with each SMES is evaluated by the infinite norm of $|G/(1-GK)|$ under five case studies. As shown in Table IV, the $||G/(1-GK)||_\infty$ in case of RSMES is lower than that of CSMES. This signifies that the robustness of the system with RMES against system uncertainties is higher than that of the system with CSMES.

Next, nonlinear simulations of five case studies are performed by Dymola software package with ObjectStab [16]. Each pattern of wind power generations W1, W2, and W3 as depicted in Fig. 11 is separately injected to bus 11. Note that, here the three-phase fault to ground is not yet applied to the system.

Figure 12 shows tie-line power deviation (ΔP_{tie}) of case 4 with wind power W1. Without SMES, since two dominant modes are unstable as shown in Table III, the tie-line power gradually increases and eventually diverges (not shown here). On the contrary, the power fluctuation is significantly alleviated by either CSMES or RSMES. Nevertheless, RSMES provides better damping effect than CSMES. Figure 13 shows the tie-line power deviations in case 4 with wind power W2. The stabilizing effect

Table III. Eigenvalues [σ (1/s) $\pm j\omega$ (rad/s)]

Case	No SMES	CSMES	RSMES
1	$-0.074 \pm j2.713$ $\zeta = 0.027$	$-0.334 \pm j2.79$ $\zeta = 0.119$	$-0.874 \pm j2.84$ $\zeta = 0.294$
	$-0.104 \pm j3.679$ $\zeta = 0.028$	$-0.225 \pm j3.68$ $\zeta = 0.0612$	$-0.315 \pm j3.71$ $\zeta = 0.0846$
2	$+0.1001 \pm j2.387$ $\zeta = -0.040$	$-0.344 \pm j3.03$ $\zeta = 0.113$	$-0.869 \pm j3.68$ $\zeta = 0.230$
	$-0.036 \pm j3.413$ $\zeta = 0.011$	$-0.225 \pm j3.70$ $\zeta = 0.0607$	$-0.466 \pm j3.84$ $\zeta = 0.121$
3	$+0.184 \pm j1.960$ $\boldsymbol{\zeta = -0.094}$	$-0.204 \pm j2.52$ $\zeta = 0.0808$	$-0.858 \pm j2.39$ $\zeta = 0.337$
	$-0.037 \pm j3.313$ $\zeta = 0.011$	$-0.278 \pm j3.70$ $\zeta = 0.075$	$-0.490 \pm j3.79$ $\zeta = 0.128$
4	$+0.1687 \pm j2.143$ $\boldsymbol{\zeta = -0.078}$	$-0.254 \pm j2.78$ $\zeta = 0.0912$	$-1.24 \pm j2.23$ $\zeta = 0.486$
	$+0.017 \pm j3.223$ $\boldsymbol{\zeta = -0.005}$	$-0.183 \pm j3.541$ $\zeta = 0.0518$	$-0.449 \pm j3.59$ $\zeta = 0.124$
5	$+0.273 \pm j1.500$ $\boldsymbol{\zeta = -0.179}$	$+0.016 \pm j2.03$ $\boldsymbol{\zeta = -0.0771}$	$-0.232 \pm j2.05$ $\zeta = 0.112$
	$+0.014 \pm j3.121$ $\boldsymbol{\zeta = -0.0438}$	$-0.214 \pm j3.44$ $\zeta = 0.062$	$-0.404 \pm j3.49$ $\zeta = 0.115$

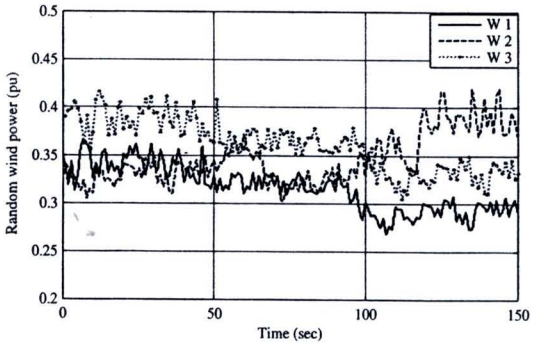

Fig. 11. Wind power generation

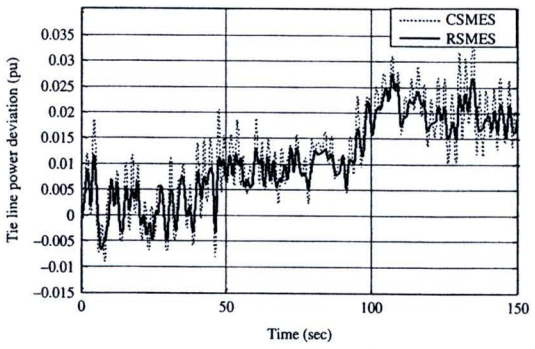

Fig. 12. Tie-line power deviation in case 4 with wind power W1

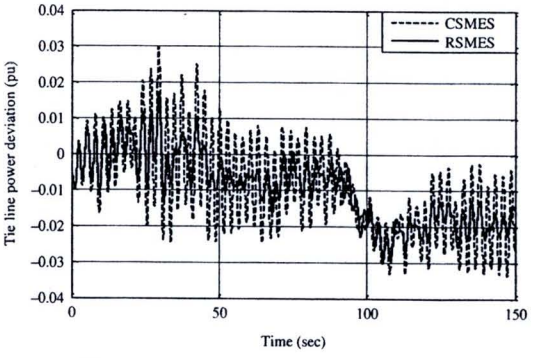

Fig. 13. Tie-line power deviation in case 4 with wind power W2

of CSMES is deteriorated. On the other hand, RSMES is still able to suppress the power oscillation effectively. Figure 14 depicts the tie-line power deviations in case 5 with wind power W3. Clearly, CSMES completely loses the stabilizing effect. The tie-line power severely oscillates and diverges. In contrast, RSMES is robustly capable of damping the power oscillation. This simulation result is consistent with the eigenvalue result of case 5.

Figures 15–17 show the comparison of the maximum ΔP_{tie} for wind powers W1, W2, and W3, respectively. From cases 1 to 5, the maximum power deviation in case of CSMES highly increases with any wind pattern. The damping effect of CSMES is sensitive to high power flow and weak line condition. On the other hand, RSMES is very robust to any operating condition and wind patterns. The maximum power deviation rarely changes. These results signify that the robust stabilizing effect of RSMES against wind power fluctuations and severe operating conditions is much superior to that of CSMES.

Next, simulation results of the phase difference between bus 1 and bus 6, which represents the inter-area oscillation, under both

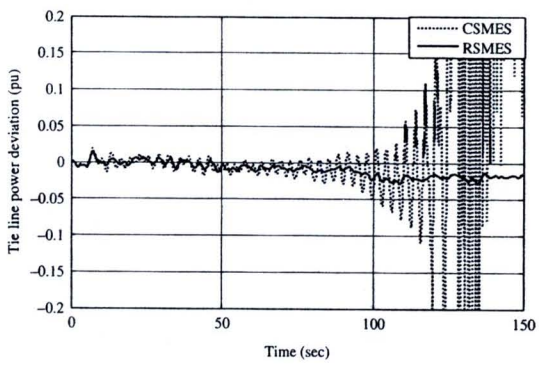

Fig. 14. Tie-line power deviation in case 5 with wind power W3

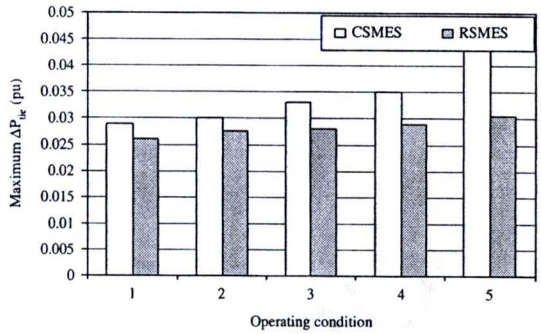

Fig. 15. Maximum ΔP_{tie} with wind power W1

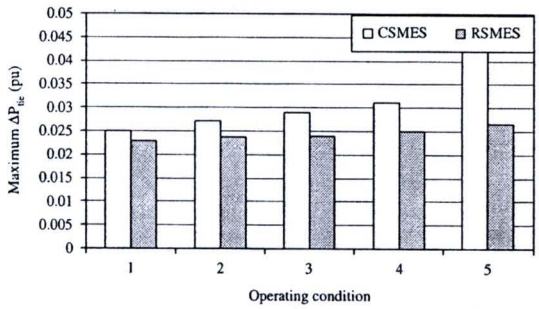

Fig. 16. Maximum ΔP_{tie} with wind power W2

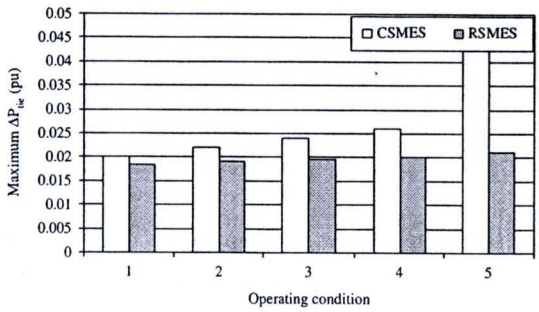

Fig. 17. Maximum ΔP_{tie} with wind power W3

wind power W1 and applied fault as given in Table II are shown in Figs 18–22. Note that the applied fault in all cases is the temporary three-phase fault to ground (3ph–G) at the specified bus for 50 ms. The 3ph–G fault is naturally cleared without fault-line rejection and re-closure operation.

In case 1, as shown in Fig. 18, the inter-area oscillation in case of no SMES is very severe and takes a long time to damp out. On the other hand, both CSMES and RSMES are able to damp out

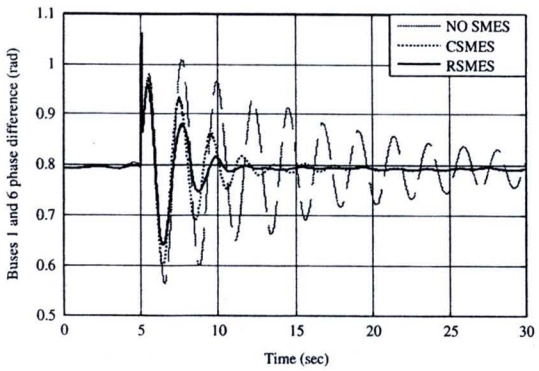

Fig. 18. Phase difference between buses 1 and 6 for case 1

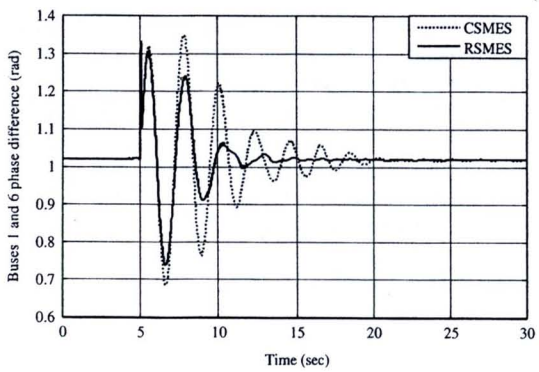

Fig. 19. Phase difference between buses 1 and 6 for case 2

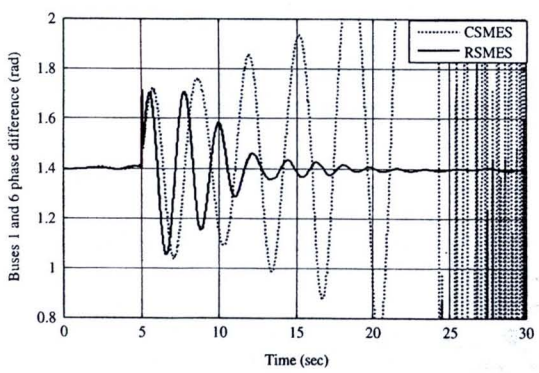

Fig. 20. Phase difference between buses 1 and 6 for case 3

power oscillation. In case 2 with higher line flow and the same fault as depicted in Fig. 19, the stabilizing effect of CSMES is deteriorated.

In contrast, RSMES is capable of damping the oscillation effectively. In case 3 with high line flow and weak line condition, as illustrated in Fig. 20, CSMES completely loses the stabilizing effect. The system stability cannot be maintained. On the contrary, RSMES is capable of damping the inter-area oscillation. Moreover, in cases 4 and 5 with heavy line flow and weak line condition as delineated in Figs 21 and 22, respectively, CSMES cannot tolerate these conditions. It fails to stabilize the system. In contrast, RSMES can robustly handle these severe conditions. The coil currents in case 5 of SMES1 and SMES2 are shown in Figs 23 and 24, respectively. Clearly, the fluctuation of coil currents in case of CSMES is very large and severe. This indicates that CSMES absolutely loses stabilizing effect. It cannot tolerate the operating condition of case 5. On the other hand, the coil current of RSMES

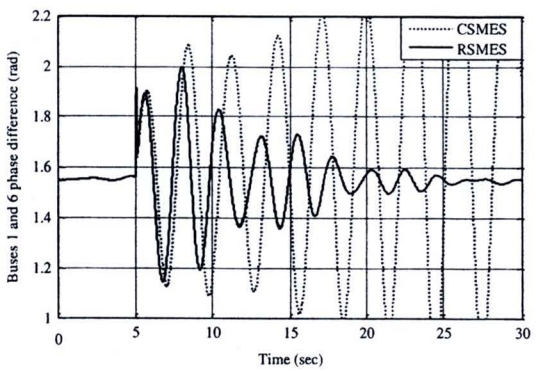

Fig. 21. Phase difference between buses 1 and 6 for case 4

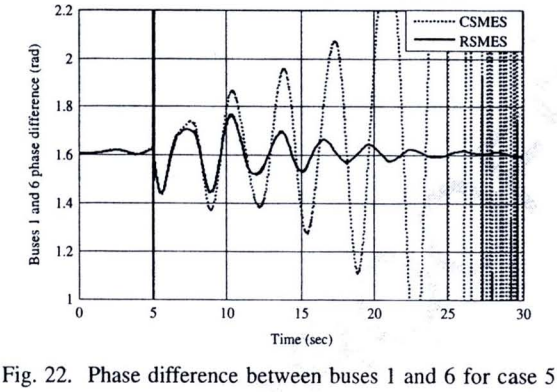

Fig. 22. Phase difference between buses 1 and 6 for case 5

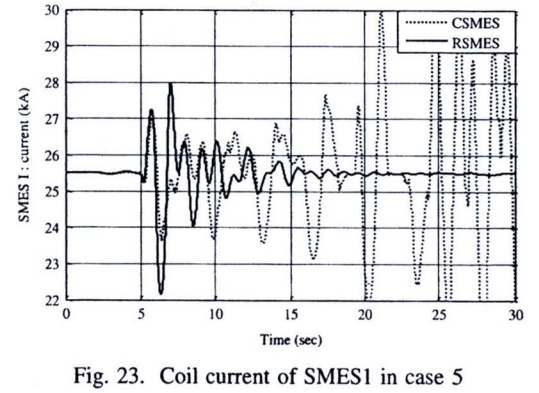

Fig. 23. Coil current of SMES1 in case 5

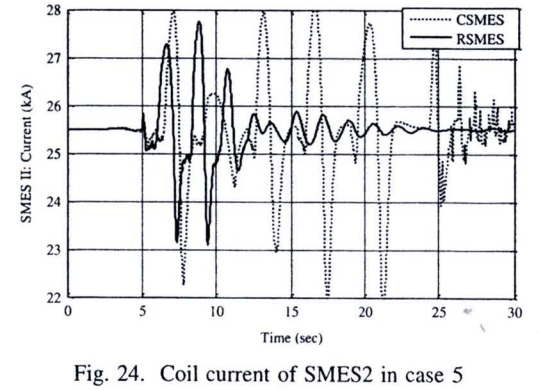

Fig. 24. Coil current of SMES2 in case 5

can properly remain within the allowable limits. This confirms that RSMES can appropriately supply and receive the larger amount of electrical energy with the power system. Accordingly, the stabilizing effect of RSMES is superior to that of CSMES.

5. Conclusions

In this paper, a practical wide-area robust SMES controller design using synchronized PMUs for stabilization of interconnected power system with wind farms has been proposed. Without the availability of all system parameters and exact system modeling, the steady-state phasor data obtained from wide-area phasor measurements can be used to establish the SOM, identify the inter-area modes, and tune robust SMES controllers. This significantly reduces the time of computation and increases the flexibility of the design. Besides, the SOM can be extended to represent the system with any number of dominant modes. This shows the generality, practicality, and robustness of the SOM. The structure of SMES power controller is the practical first-order lead/lag compensator with a single input. The inverse additive perturbation has been applied to represent unstructured system uncertainties. Based on the robust stability improvement, the SMES parameters have been automatically optimized by GA in the SOM. The designer can use the most recent PMU data to tune the controller in order to achieve the desired damping of the dominant inter-area modes. Simulation results in the West Japan six-machine longitudinal interconnected power system confirm that the proposed SMES is very robust against various line flow conditions, network structures, random wind power, and fault locations.

Acknowledgements

This work was supported by the Thailand Research Fund under the Basic Research Grant No.BRG5080019 and the KMITL Research Funds.

References

(1) Slootweg JG, Kling WL. The impact of large scale wind power generation on power system oscillations. *Electric Power System Research* 2003; **67**:9–20.

(2) Fernández RD, Mantz RJ, Battaiotto PE. Impact of wind farms on a power system, an eigenvalue analysis approach. *Renewable Energy* 2007; **32**:1676–1688.

(3) Ackermann T. *Wind• Power in Power Systems*, John Wiley & Sons Ltd; 2005.

(4) Jenkins N,• Allan R, Crossley P, Kirschen D, Strbac G. Embedded generation. *IEE Power Energy Series* 2000; **31**.

(5) Boom RW, Perterson H. A superconducting energy storage for power systems. *IEEE Transactions on Magnetics* 1972; **8**:701–703.

(6) Ise T, Mitani Y, Tsuji K. Simultaneous active and reactive power control of superconducting magnetic energy storage to improve power system dynamic performance. *IEEE Transactions on Power Delivery* 1986; **1**:143–150.

(7) Nomura S, Ohata Y, Hagita T, Tsutsui H, Tsuji-ito S, Shimada R. Wind farms linked by SMES systems. *IEEE Transactions on Applied Superconductivity* 2005; **15(2)**:1951–1954.

(8) Shi J, Tang YJ, Ren L, Li JD, Chen SJ. Application of SMES in wind farm to improve voltage stability. *Physica C: Superconductivity and its Applications* 2008; **468(15–20)**:2100–2103.

(9) Phadke AG. Synchronized phasor measurements in power systems. *IEEE Computer Application in Power* 1993; **6(2)**:10–15.

(10) Phadke AG, Thorp JS. *Synchronized Phasor Measurements and Their Applications*. Springer; 2008.

(11) Rehtanz C. Tack force on wide area monitoring and control for transmission capability enhancement, CIGRE WG C4.6.01, 2006.

(12) Begovic M, Novosel D, Karlsson D, Henville C, Michel G. Wide-area protection and emergency control. *Proceedings of the IEEE* 2005; **93(5)**:876–891.

(13) Kanwa I, Grondin R, Hebert Y. Wide-area measurement based stabilizing control of large power systems—a decentralized/hierarchical approach. *IEEE Transactions on Power Systems* 2001; **16(1)**:136–153.

(14) Wanatabe M, Izumi T, Hashiguchi T, Mitani Y. An approach for tuning of power system stabilizer based on the wide area phasor measurements, *Proceedings of 15th Power System Computation Conference*, 2005.

(15) Gu P,• Petkov Hr, Konstantinov MM. *Robust Control Design with MATLAB*. Springer; 2005.

(16) Larsson M. ObjectStab—an educational tool for power system stability studies. *IEEE Transactions on Power Systems* 2004; **19(1)**:56–63.

(17) Technical Committee of the Institute of Electrical Engineers of Japan (IEEJ). Japanese Power System Models, Online available at: http://www.iee.or.jp/pes/model/english/index.html.

(18) Dechanupaprittha S, Hongesombut K, Watanabe M, Mitani Y, Ngamroo I. Stabilization of tie-line power flow by robust SMES controller for interconnected power system with wind farms. *IEEE Transactions on Applied Superconductivity* 2007; **17(2)**:2365–2368.

(19) Martin N, Lima LTG. Determination of suitable locations for power system stabilizers and static var compensators for damping electromechanical oscillation in large power systems. *IEEE Transactions on Power Systems* 1990; **5(4)**:1455–1469.

(20) Kundur P. *Power System Stability and Control*. McGraw Hill; 1994.

(21) Kamwa I, Trudel G, Gerin-Lajoie L. Low order black-box models for control system design in large power systems. *IEEE Transactions on Power Systems* 1996; **11(1)**:301–311.

(22) Hasanovic A, Feliachi A, Hasanovic A, Bhatt NB, DeGroff AG. Practical robust PSS design through identification of low-order transfer functions. *IEEE Transactions on Power Systems* 2004; **19(3)**:1492–1500.

(23) Haupt RL, Hault SE. *Practical Genetic Algorithm*, 2nd edition. Wiley-interscience; 2004.

(24) Abdel-Magid YL, Abido MA. Optimal multiobjective design of robust power system stabilizers using genetic algorithms. *IEEE Transactions on Power Systems* 2003; **18(3)**:1125–1132.

(25) Tada M, Mitani Y, Tsuji K. Power control by superconducting magnetic energy storage for load change compensation and power system stabilization in interconnected power system. *IEEE Transactions on Applied Superconductivity* 1995; **5(2)**:250–253.

Issarachai Ngamroo (Non-member) received the B.Eng. degree in electrical engineering from King Mongkut's Institute of Technology Ladkrabang (KMITL), Bangkok, Thailand, in 1992. He continued his education under the Monbusho Scholarship from the Japanese Government at Osaka University, Japan, where he earned the M.Eng. and Ph.D. degrees in electrical engineering in 1997 and 2000, respectively. Currently, he is an Associate Professor in the Electrical Engineering Department, Faculty of Engineering and Center of Excellence for Innovative Energy Systems (CInES), KMITL. His research interests are in the areas of power system stability, dynamics, and control.

Cuk Supriyadi Ali Nandar (Non-member) received the B.Eng degree in electrical engineering from Gadjah Mada University, Yogyakarta, Indonesia, in 2002, and the M.Eng. degree in electrical engineering from KMITL, Thailand, in 2009. He is currently a Researcher at The Agency for the Assessment and Application of Technology (BPPT), Indonesia. His research interests include power system stability and renewable energy.

Sanchai Dechanupaprittha (Member) received the B.Eng. and M.Sc. degrees in electrical engineering from Sirindhorn International Institute of Technology, Thammasat University, Thailand, in 2000 and 2003, respectively. He continued his education under the Monbusho Scholarship from the Japanese Government at Kyushu Institute of Technology, Japan, where he earned the Ph.D. degree in electrical engineering in 2008. He is currently a Researcher at the Department of Electrical Engineering, Faculty of Engineering, Kyushu Institute of Technology, Fukuoka, Japan. His research interests include power system stability, dynamics, and control.

Masayuki Watanabe (Member) received the B.Sc., M.Sc., and D.Eng. degrees in electrical engineering from Osaka University, Japan, in 2001, 2002, and 2004, respectively. He is currently Associate Professor at the Department of Electrical Engineering, Faculty of Engineering, Kyushu Institute of Technology, Fukuoka, Japan. His research interests are in the areas of analysis and control of power systems.

Yasunori Mitani (Member) received the B.Sc., M.Sc., and D.Eng. degrees in electrical engineering from Osaka University, Japan, in 1981, 1983, and 1986, respectively. He is currently a Professor at the Department of Electrical Engineering, Faculty of Engineering, Kyushu Institute of Technology, Fukuoka, Japan. His research interests are in the areas of analysis and control of power systems.

Electrical Power and Energy Systems 32 (2010) 478–487

Contents lists available at ScienceDirect

Electrical Power and Energy Systems

journal homepage: www.elsevier.com/locate/ijepes

Ant colony optimisation for economic dispatch problem with non-smooth cost functions

Saravuth Pothiya [a], Issarachai Ngamroo [b,*], Waree Kongprawechnon [a]

[a] School of Communication, Instrumentation and Control, Sirindhorn International Institute of Technology, Thammasat University, P.O. Box 22, Pathumthani, Thailand
[b] Center of Excellence for Innovative Energy Systems, Faculty of Engineering, King Mongkut's Institute of Technology Ladkrabang, Bangkok 10520, Thailand

ARTICLE INFO

Article history:
Received 28 September 2008
Received in revised form 8 July 2009
Accepted 25 September 2009

Keywords:
Ant colony optimisation
Economic dispatch problem
Genetic algorithm
Particle swarm optimisation
Tabu search

ABSTRACT

This paper presents a novel and efficient optimisation approach based on the ant colony optimisation (ACO) for solving the economic dispatch (ED) problem with non-smooth cost functions. In order to improve the performance of ACO algorithm, three additional techniques, i.e. priority list, variable reduction, and zoom feature are presented. To show its efficiency and effectiveness, the proposed ACO is applied to two types of ED problems with non-smooth cost functions. Firstly, the ED problem with valve-point loading effects consists of 13 and 40 generating units. Secondly, the ED problem considering the multiple fuels consists of 10 units. Additionally, the results of the proposed ACO are compared with those of the conventional heuristic approaches. The experimental results show that the proposed ACO approach is comparatively capable of obtaining higher quality solution and faster computational time.

1. Introduction

The economic dispatch (ED) problem is one of the optimisation problems in power system operation. The objective of ED problem is to schedule the optimal combination of outputs of all generating units and to minimise the operating cost while satisfying the load demand and system equality and inequality constraints. Improvements in scheduling of the unit power outputs can lead to significant cost savings.

Generally, the input–output characteristics of modern power generating units are inherently high nonlinear because of valve-point loading effects, multi-fuel effects, etc. To take these effects into consideration, the ED problem can be represented as a non-smooth optimisation problem. These effects may lead to multiple local minimum points of the cost functions. This makes the problem of finding the global or near global optimum difficult.

Over the past few years, a number of approaches have been developed for solving this problem using mathematical programming, i.e. lambda iteration method, gradient method, and linear programming, etc. However, these methods may not be able to provide an optimal solution because they usually get stuck at a local optimum.

Recently, modern heuristic optimisation techniques have been applied to solve ED problem due to their abilities of finding an almost global optimal solution. The simulated annealing (SA) [1,2] is a powerful optimisation technique and it has the ability to find near global optimum solutions for the optimisation problem. However, appropriate setting of the control parameters of the SA based algorithm is a difficult task and the convergence speed of the algorithm is slow when applied to a real power system.

Evolutionary algorithms (EAs), such as genetic algorithm (GA) [2–5], evolutionary strategy (ES) and evolutionary programming (EP) [6,7], are faster than simulated annealing (SA) because of their inherent parallel search technique. The genetic algorithm (GA) is a stochastic optimisation technique, which is based on the principle of natural selection and genetics. It combines solution evaluation with randomized, structured exchanges of genetic information between solutions to obtain optimality. Also it searches multiple solutions simultaneously in contrast to conventional optimal algorithms. Therefore, the possibility of finding global optimal solution is increased. The main advantage of GA is that it finds near optimal solution in relatively short time compared with other random searching methods.

A conventional TS algorithm, an iterative search algorithm, has been developed in [8,9]. It has been applied to solve combinatorial optimisation problems. The main advantages of the TS algorithm are its ability to escape from local optima and fast convergence to the global optimum. However, a conventional TS algorithm might have problems with reaching the global optimum solution in a reasonable computational time when the initial solution is far away from the region where the optimum solution exists.

* Corresponding author.
E-mail address: ngamroo@gmail.com (Issarachai Ngamroo).

0142-0615/$ - see front matter © 2009 Elsevier Ltd. All rights reserved.
doi:10.1016/j.ijepes.2009.09.016

The ED problems have recently been solved by Particle Swarm Optimisation (PSO) approaches [10,11]. The PSO originally developed by Eberhart and Kennedy in 1995 is a population-based stochastic algorithm. The PSO is an evolutionary optimisation tool of swarm intelligence field based on a swarm (population), where each member is seen as a particle, and each particle is a potential solution to the problem under analysis. Each particle in PSO has a randomized velocity associated to it, which moves through the space of the problem. PSO, however, allows each particle to maintain a memory of the best solution that it has found and the best solution found in the particle's neighborhood is swarm.

Furthermore, other methods, i.e. the combining of chaotic differential evolution and quadratic programming [12], Taguchi method [13] and direct search [14] have been applied to ED problems. Studies based on these methods show satisfactory results. Nevertheless, the new algorithm which is able to provide higher quality solution and faster computational time is highly expected.

In this respect, the algorithms inspired by the observation of natural phenomena to help solving combinatorial problems have been paid attentions by many researchers. One of these algorithms is the ant colony optimisation (ACO), which has become a candidate for many optimisation applications. The first ACO was introduced by Dorigo [15,16]. The ACO algorithm is inspired by the behaviours of real ant colonies. In analyzing the behaviours of real ants, it was found that the ants are capable of finding the shortest path from the nest to the food source without using cues. The ACO has been applied to solve the travelling salesman problem [17,18], the quadratic assignment problem [19], the vehicle routing problem [20], and the job-shop scheduling problem. For an application to ED problem, there are a few literatures [21,22]. In these works, the simple ACO algorithm has been used to solve a traditional ED problem with small-scale power systems. Besides, the non-smooth cost function due to valve-point loading and multiple fuels effects have not been taken into consideration.

The goal of this paper is to develop the ACO algorithm for solving the ED problem with non-smooth cost functions. To improve the search performance of the ACO, three techniques i.e. priority list, variable reduction and zoom feature have been added. Two types of ED problems with non-smooth cost functions are used to evaluate the effect of ACO. Firstly, the ED problem consisting of 13 and 40 generating units which considers the effect of valve-point loading is used. Secondly, the ED problem considering the multiple fuels with 10 generating units is studied. The results optimised by the proposed ACO are compared to those obtained by the conventional approaches, i.e. GA, TS, PSO and ACO in terms of solution quality and computational efficiency.

The paper is organised as follows. Section 2 gives the mathematical model of the ED problem with non-smooth cost functions. Section 3 mentions the principle of ACO algorithm. Section 4 presents the detailed procedures of the ACO approach for solving the ED problem. Besides, case studies and comparison results with the traditional methods are given. Conclusion is finally given in Section 5.

2. Problem formulation

The objective of the ED problem is to find the optimal combination of power generation that minimises the total generation costs while satisfying an equality constraint and an inequality constraint.

2.1. Objective function

In reality, the objective function of an ED problem has non-differentiable points according to valve-point effects and multiple fuels. Therefore, the objective function is composed of a set of non-smooth cost functions.

2.1.1. Non-smooth cost functions with valve-point effects

To take account for the valve-point effects, sinusoidal functions are added to the quadratic cost functions as follows:

$$F_t = \sum_{i=1}^{n} F_i(P_i) = a_i + b_i P_i + c_i P_i^2 + |e_i \times \sin(f_i \times (P_i^{\min} - P_i))| \tag{1}$$

where F_t is the total generation costs; $F_i(P_i)$ is the generation cost function of the ith generator which is usually expressed as a quadratic polynomial; a_i, b_i, and c_i are the cost coefficients of the ith generator; e_i and f_i are the coefficients of generator reflecting valve-point effects. P_i is the power output of the ith generator and n is the number of generators committed to the operating system.

2.1.2. Non-smooth cost functions with multiple fuels

Generally, a piecewise quadratic function is used to represent the input–output curve of a generator with multiple fuels [11]. The piecewise quadratic function is described by

$$F_i(P_i) = \begin{cases} a_{i1} + b_{i1} P_i + c_{i1} P_i^2 & P_i^{\min} \leqslant P_i \leqslant P_{i1} \\ a_{i2} + b_{i2} P_i + c_{i2} P_i^2 & P_{i1} \leqslant P_i \leqslant P_{i2} \\ \quad \vdots & \quad \vdots \\ a_{ik} + b_{ik} P_i + c_{ik} P_i^2 & P_{ik-1} \leqslant P_i \leqslant P_i^{\max} \end{cases} \tag{2}$$

where a_{ij}, b_{ij}, and c_{ij} are the cost coefficients of the ith generator for the jth power level.

The ED problem is given by

$$\text{Minimize} \quad J = \sum_{i=1}^{n} F_i(P_i) \tag{3}$$

The goal is to determineP_i, $i = 1, 2, \ldots, n$, so that the cost function J is minimised subject to the following two constraints.

2.2. Constraints

2.2.1. Equality constraint

While minimising the total generation costs, the total generations should be equal to the total demands plus the transmission network losses. However, the network losses are not considered in this paper for simplicity. Therefore, the equality constraint is given by

$$\sum_{i=1}^{n} P_i = P_D \tag{4}$$

where P_D is the load demand.

2.2.2. Inequality constraint

The generation output of each unit is between its minimum and maximum limits. This provides the following inequality constraint for each generator:

$$P_i^{\min} \leqslant P_i \leqslant P_i^{\max} \tag{5}$$

where $P_i^{\min}$, $P_i^{\max}$: minimum, maximum output of the ith generator.

3. Ant colony optimisation

3.1. Basic principle of ant colony

The ACO algorithm is inspired by the collective behaviour of a real ant colony. Marco Dorigo first introduced the ACO in his Ph.D. thesis in 1992. Further studies have been carried out [15,16]. The characteristics of an artificial ant colony include

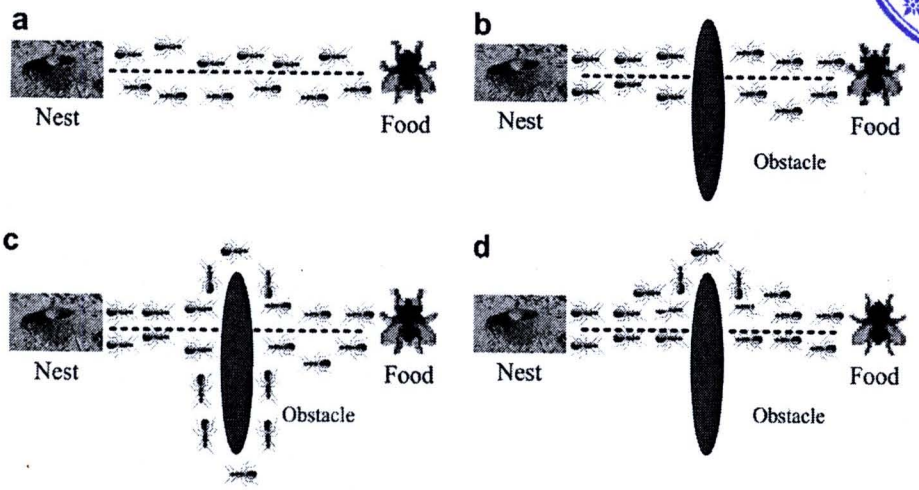

Fig. 1. Behaviour of ants: (a) Ants follow a path between nest and food source. (b) An obstacle appears on the path: ants choose whether to turn left or right with equal probability. (c) Pheromone is deposited more quickly on the shorter path. (d) All ants have chosen the shorter path.

positive feedback, distributed computation, and the use of a constructive greedy heuristic. Positive feedback accounts for rapid discovery of good solutions. Distributed computation avoids premature convergence. The greedy heuristic helps to find acceptable solutions in the early stages of the search process.

ACO is an evolutionary meta-heuristic algorithm based on a graph representation. The main idea of ACO is to model the problem as the search for a minimum cost path in a graph. Artificial ants walk through this graph and look for good paths. Better paths are found as the emergent result of the global cooperation among ants in the colony.

Naturally, an ant deposits pheromone while walking. It probabilistically prefers to follow a direction which enriches pheromone. This behaviour can be explained how ants can find the shortest path that reconnects a line broken by an obstacle.

For example, finding the new shortest path once the old one is no longer feasible due to the new obstacle. This can be clearly illustrated by Fig. 1a. Ants are on a straight line that connects a food source to their nests. In Fig. 1b, those ants are just in front of the obstacle and they cannot continue to go. Therefore, they have to choose between turning right or left. Half the ants choose to turn right and another half choose to turn left. A similar situation arises on another side of the obstacle in Fig. 1c. Ants choosing the shorter path more rapidly reconstitute the interrupted pheromone trail compared with those choosing the longer path. Thus, the shorter path receives a greater amount of pheromone per time unit and, in turn, a larger number of ants choose the shorter path. Due to this positive feedback, all ants rapidly choose the shorter path in Fig. 1d. All ants move at approximately the same speed and deposit a pheromone trail at approximately the same rate. The time consumed on the longer side of an obstacle is greater than the shorter one. This makes the accumulation of pheromone trail more quickly on the shorter side.

3.2. ACO algorithm for solving ED problem

In this section, the ACO algorithm is described for solving the ED problem. Especially, a suggestion is given how to improve the search process. The detailed of the ACO algorithm can be described in the following steps:

Step 0 Pre-Initialization
  Applied the Priority list technique
  Applied the Variable reduction technique
  Set stage = 1
Step 1 Initialization of stage
  Divide the search space to n nodes
Step 2 Initialization of ACO
  Set NC = 0 /* NC: cycle counter */
  For every combination (i,j)
    Set an initial value $\tau_{ij}(0) = \tau_0$ and $\Delta\tau_{ij} = 0$
End
Step 3 Construct feasible solutions
  For $k = 1$ to m /* m: number of ants */
    For $i = 1$ to $N - 1$ /* N: number of units */
      Choose a power of ith unit with transition probability given by Eq. (13).
    End
    Last power calculate by Eq. (8)
    Calculate cost C_k
      /* C_k: generation cost for each ant */
  End
  Update the best solution
Step 4 Global updating rules
  For every combination (i,j)
    For $k = 1$ to m
      Find $\Delta\tau_{ij}^k$ according to Eq. (17)
  End
  Update $\Delta\tau_{ij}$ according to Eq. (16)
  End
  Update the trail values according to Eq. (15)
  Update the transition probability according to Eq. (13)
Step 5 Next search of ACO
  Set NC = NC + 1
  For every combination (i,j)
    $\Delta\tau_{ij} = 0$
  End
Step 6 Termination of ACO
  If (NC < NC_{max})
    Then
      Goto step 3
    Else
      Print the best feasible solution
    End
  End
Step 7 Next search of stage
  Set stage = stage + 1
Step 8 Termination of stage

If (stage < stage_{max})
Then
Goto step 1
Else
Print the best feasible solution
End
End

To improve the performance of ACO, this paper proposes three techniques, i.e. priority list, variable reduction, and zoom feature. Informally, the ACO algorithm works as follows: m ants are initially positioned on the node representing the first direction. Each ant constructs one possible structure of the entire system. In fact, each ant builds a feasible solution (called a tour) by repeatedly applying a stochastic greedy search, called, the state transition rule.

The amount of pheromone is modified by applying the global updating rule. Ants are guided, in building their tours, by both heuristic information and pheromone information. Generally, a direction with a high amount of pheromone is a very desirable choice. The pheromone updating rules are designed to give more pheromone to directions which are visited by ants. In the subsequent sections, the detailed implementation strategies of the proposed ACO are described.

3.2.1. Structure of individuals

In this paper, the structure of an individual for ED problem is composed of a set of power generation outputs. Therefore, the individual j's ant at the zero iteration (initial) can be represented as the vector of $X_j^0 = (P_{1j}^0, \ldots, P_{nj}^0)$. Note that it is very important to create a set of individuals satisfying the equality and inequality constraints.

3.2.2. Graph representation

In order to build a graph for representation of the problem, suppose that the ACO algorithm deals with an objective function bounded over a fixed interval of variables P_i. The lower and upper ends of the initial interval for each variable are denoted by their corresponding lower and upper limits. The search space is divided into N zones. Each zone has the fixed interval of variables P_i. The width of each zone is given by

$$Z_i^j = \frac{P_i^{max} - P_i^{min}}{N} \quad j = 1,2,\ldots,N \tag{6}$$

where Z_i^j is the jth zone for the ith generator, and N is a number of zones and nodes.

The individual of each variable is set to be a half interval of each zone. The formulation of each individual node can be obtained by

$$P_i^j = P_i^{min} + \frac{Z_i^j}{2} + Z_i^j \times (j-1) \quad j = 1,2,\ldots,N \tag{7}$$

Then, each variable has N individuals to be bracketed in the closed interval. The best value of the objective function occurs in one of N individuals. In ACO, it is convenient to represent the problem by a graph $G = (N, E)$, where N is number of nodes of power outputs and E is the set of directions. Ants use the indirect form of communication mediated by pheromone. They deposit pheromone on the directions of the graph G while building solutions. This system can be represented by a graph of the routes between the nest and the food source as shown in Fig. 2.

3.2.3. Priority list

One of the important problems for finding the optimal solution is the generation of new solutions which satisfy both equality and inequality constraints. To improve the performance of generating the new solutions, this paper proposes the priority list which is the technique for ranking the effects of the generating units for creating the new solutions. This technique helps to increase the performance of finding the new solutions which satisfy the constraints. Furthermore, it reduces the searching time. Here, the difference between the maximum and minimum power outputs of ith generator ($P_i^{max} - P_i^{min}$) is used for ranking the generating units. The algorithm of priority list is given as follows:

Step 1 Find the difference of maximum and minimum power output of each generating unit
For $i = 1$ to n
The ith difference of power output = $P_i^{max} - P_i^{min}$
End
Step 2 Sort (form min to max) the generating units depend on the interval.
Step 3 Exit

3.2.4. Variable reduction

For the ED problem without considering the network losses, the summation of all generation power outputs should be equal to the total system demands. Although, the problem can be solved without reducing the variables, it is necessary to develop a new strategy. To improve the accuracy of the solution and reduce the search space, the variable reduction technique is proposed. This

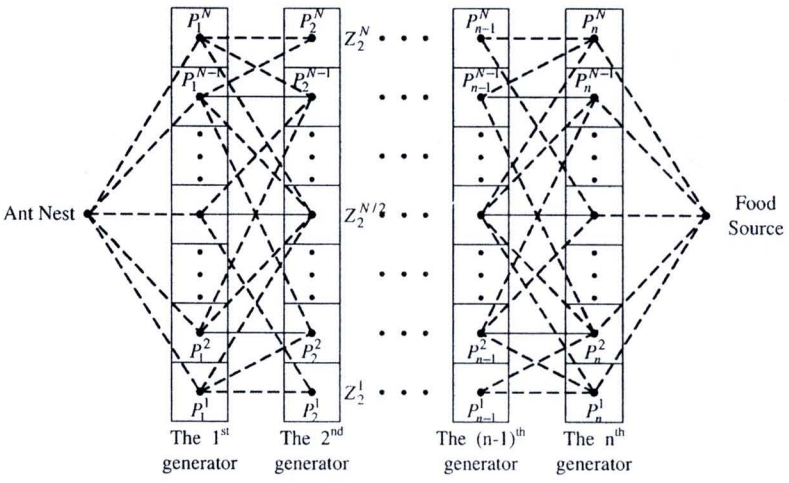

Fig. 2. Graph of ACO.

technique reduces one variable. The values of $n-1$ generation power outputs after the priority list are determined randomly from the interval of $[P_i^{min}, P_i^{max}]$. The value of the last generation power output which is reduced, can be determined by

$$P_n = P_D - \sum_{j=1}^{n-1} P_j \tag{8}$$

3.2.5. Zoom feature

To accelerate the convergence speed to the optimal solution, the zoom feature technique is presented. The search procedure is divided into K stages. This technique is used for reducing the search space. The search space is dynamically reduced based on the best solution which is found by the ACO at the previous stage.At the first stage, a large interval of zone is selected. When the upper and lower bounds of the i\{th\} generating unit are $UB_i^1 = P_i^{max}$ and $LB_i^1 = P_i^{min}$, respectively. As a result, the fixed interval of the zone at the first stage can be calculated by

$$\Delta_i^1 = \frac{P_i^{max} - P_i^{min}}{N} \tag{9}$$

where N is a number of nodes, UB_i^j and LB_i^j are the upper and lower bounds of the ith generating unit at stage jAfter the first stage, the upper and lower bounds of the ith generating unit are determined by

$$UB_i^j = \min(Z_i^{best} + \Delta_i^{j-1}, P_i^{max}) \tag{10}$$

$$LB_i^j = \max(Z_i^{best} - \Delta_i^{j-1}, P_i^{min}) \tag{11}$$

where Z_i^{best} is the zone where the best solution exists. This zone is found by ACO at the previous stage. The UB_i^j are the minimum value of $Z_i^{best} + \Delta_i^{j-1}$ and P_i^{max}. The LB_i^j are the maximum value of $Z_i^{best} - \Delta_i^{j-1}$ and P_i^{min}. Therefore, the interval of power output of each generator is successively reduced by

$$\Delta_i^j = \frac{UB_i^j - LB_i^j}{N} \tag{12}$$

Note that, the search space is also reduced when the interval of power output is reduced.

3.2.6. State transition rule

The state transition rule used by the ant colony is given in (13). This represents the probability that the ant k selects the jth power output of the ith generator:

$$p_{ij}^k(t) = \frac{[\tau_{ij}(t)]^\alpha [\eta_{ij}(t)]^\beta}{\sum_{m=1}^{M_i} [\tau_{im}(t)]^\alpha [\eta_{im}(t)]^\beta} \tag{13}$$

where τ_{ij} and η_{ij} are the pheromone intensity and the heuristic information between the jth power output of the ith generator, respectively. α is the relative importance of the trail and β is the relative importance of the heuristic information η_{ij}. The heuristic information can be formulated by

$$\eta_{ij} = \frac{1}{C_{ij}} \tag{14}$$

where C_{ij} represents the associated cost. That is, the node with smaller cost has greater probability to be chosen.

3.2.7. Global updating rule

During the construction process, it can not guarantee that an ant can construct a feasible solution which obeys the equality and inequality constraints. The unfeasibility of solutions is treated in the pheromone update. The amount of pheromone deposited by an ant is set to a high value if the generated solution is feasible and to a low value if the generated solution is infeasible. These values are dependent of the solution quality. Infeasibilities can then be handled by assigning penalties which are proportional to the amount of cost violations. In the case of feasible solutions, an additional penalty proportional to the obtained solution is introduced to improve the solution's quality.

Following the above remarks, the trail intensity is updated as follows:

$$\tau_{ij}(new) = \rho\tau_{ij}(old) + \Delta\tau_{ij} \tag{15}$$

ρ is a coefficient such that $(1-\rho)$ represents the evaporation of trail and $\Delta\tau_{ij}$ is:

$$\Delta\tau_{ij} = \sum_{k=1}^{m} \Delta\tau_{ij}^k \tag{16}$$

where m is the number of ants and $\Delta\tau_{ij}^k$ is given by:

$$\Delta\tau_{ij}^k = \begin{cases} Q \times penalty_k & \text{if the } k\text{th ant chooses power output } j \text{ for unit } i \\ 0 & \text{otherwise} \end{cases} \tag{17}$$

where Q is a positive number, and $penalty_k$ is defined as follows:

$$penalty_k = \left(\frac{C^*}{C_k}\right)^a \tag{18}$$

C_k is the cost obtained by an ant k, C^* is the best obtained solution. Parameter a represents the relative importance of penalties.

3.2.8. Stopping criteria

There are several possible conditions for stop searching. Here, the termination of search process is used if any following two conditions are satisfied. Firstly, the accuracy of the best solution is lower than the expected value. Secondly, the maximum allowable number of iterations is achieved.

3.3. Example of the ACO for solving ED problem

To describe the procedure of the ACO algorithm for solving the ED problem, the small-scale system with three generating units is used. The load demand is 850 MW. As studied in [8], the global optimum solution is $P_1 = 300.26$ MW, $P_2 = 400$ MW, and $P_3 = 149.74$ MW and the minimum generation cost is 8,234.07 \$/h.The generation outputs (P_1, P_2, and P_3) are coded by the number of nodes which depend on the resolution. A large number of nodes are used for increasing the resolution of the solution. Therefore, the resolution (RS) can be found by

$$RS = \frac{P_i^{max} - P_i^{min}}{N} \tag{19}$$

In case of the resolution is equal to 0.01 MW. From (19), the number of nodes (N) for the 1st , 2nd , and 3rd generating units are 5×10^4, 3×10^4, and 1.5×10^4, respectively. It is a large number of nodes. Accordingly, the search space for this problem is $(5 \times 10^4) \times (3 \times 10^4) \times (1.5 \times 10^4) = 2.25 \times 10^{13}$. Therefore, it is not easy to find the optimum solution due the very large search space.The ACO algorithm for solving the three generating units system can be illustrated in following. In this system, the interval $(P_i^{max} - P_i^{min})$ of the 1st , 2nd , and 3rd generating units are 500 MW, 300 MW, and 150 MW, respectively. When the priority list technique is applied, the ranking of generating units is ordered as (P_3, P_2, P_1)For the variable reduction, the 1st generating unit (P_1) which has the maximum interval, is reduced. The remaining variables are equal to 2. Therefore, the set of solution is (P_3, P_2). Furthermore, the search

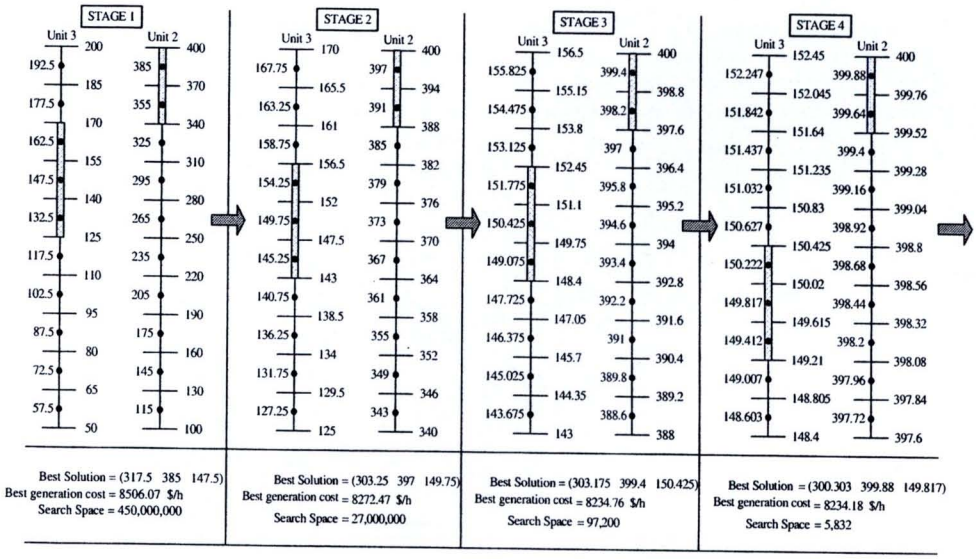

Fig. 3. Results of ACO for solving 3 generating units system.

Table 1
Best result obtained by proposed ACO for 13-unit system.

Unit	P_i^{min} (MW)	P_i^{max} (MW)	P_i (MW)
1	0	680	628.32
2	0	360	299.06
3	0	360	299.17
4	60	200	159.73
5	60	200	159.73
6	60	200	159.73
7	60	200	159.73
8	60	200	159.72
9	60	200	159.72
10	40	120	75.47
11	40	120	77.33
12	55	120	92.10
13	55	120	90.59
	Total power output (MW)		2,520.00
	Total generation cost ($/h)		24,169.63

Table 2
Best result obtained by proposed ACO for 40-unit system.

Unit	P_i^{min} (MW)	P_i^{max} (MW)	P_i (MW)	Unit	P_i^{min} (MW)	P_i^{max} (MW)	P_i (MW)
1	36	114	110.80	21	254	550	524.60
2	36	114	111.80	22	254	550	523.70
3	60	120	97.80	23	254	550	523.70
4	80	190	179.84	24	254	550	524.20
5	47	97	92.70	25	254	550	524.00
6	68	140	139.96	26	254	550	524.00
7	110	300	299.96	27	10	150	13.20
8	135	300	299.88	28	10	150	10.00
9	135	300	284.48	29	10	150	11.60
10	130	300	131.80	30	47	97	90.80
11	94	375	168.00	31	60	190	189.50
12	94	375	94.28	32	60	190	189.50
13	125	500	214.22	33	60	190	186.50
14	125	500	393.44	34	90	200	199.00
15	125	500	304.16	35	90	200	197.50
16	125	500	304.76	36	90	200	198.30
17	220	500	489.00	37	25	110	109.70
18	220	500	490.60	38	25	110	109.90
19	242	550	511.44	39	25	110	108.90
20	242	550	511.20	40	242	550	511.44
	Total power output (MW)						10,500
	Total generation cost ($/h)						121,532.41

space is reduced from 2.25×10^{13} to $(1.5 \times 10^4) \times (3 \times 10^4) = 4.5 \times 10^8$. For this problem, a number of nodes is equal to 10. At the first stage, the interval of each zone can be determined by (6). The individual's node is set to a half interval of each zone which is determined by (7). Therefore, the graph which represents the problem after applying the priority list and the variable reduction is given in Fig. 3.At the first stage, the best solution which is found by ACO is (317.5, 385, 147.5). The best generation cost is 8,506.07 $/h. When the zoom feature is applied, the search space for the second stage is reduced from 4.5×10^8 to 2.7×10^7.

The processes are carried out until they satisfy the termination criteria. As seen in Fig. 3, the ACO converges to the near optimal solution very fast. It achieves the near optimum solution at the 4th stage.

4. Numerical results

To assess the feasibility of the ACO approach, two cases studies of ED problems with non-smooth objective function considering

Table 3
Convergence results for 13-unit system.

Method	Load demand = 2520 MW				
	Worst	Average	Best	Std.	CPU time
GA	24328.23	24258.28	24186.02	40.61	112.27
TS	24304.62	24243.37	24180.31	37.24	45.38
PSO	24241.83	24208.05	24171.70	20.23	30.40
ACO	24243.90	24211.09	24174.39	21.10	32.47
Proposed ACO	24195.91	24182.79	24169.63	7.86	14.35

Table 4
Convergence results for 40-unit system.

Methods	Load demand = 10,500 MW				
	Worst	Average	Best	Std.	CPU time
GA	123807.97	122919.77	121996.40	492.11	320.31
TS	122590.89	122424.81	122288.38	88.10	238.35
PSO	122000.80	121899.57	121800.13	59.28	84.21
ACO	122048.06	121930.58	121811.37	67.02	92.54
Proposed ACO	121679.64	121606.45	121532.41	45.58	52.45

valve-point effects and multiple fuels are used. All optimisation methods (GA, TS, PSO, and ACO) were implemented in MATLAB®. These programs were run on a Pentium 4, 2.6 GHz personal microcomputer with 1 GB RAM under Windows XP.

In each case study, 100 independent runs are carried out for each optimisation method. In addition, 100 different initial trial solutions are used for each method.

4.1. ED problem considering valve-point effects

The ACO is applied to two ED problems with 13 and 40 generating units where valve-point effects are considered. The input data for 13 generating units system are given in [7] with 2520 MW load demand. Another, the input data for 40 generating units system are given in [6] with 10,500 MW load demand. The global solutions for these systems are not discovered yet. The best local solutions reported until now for 13 and 40 generating units are 24,169.92 $/h [14] and 121,741.98 $/h [12], respectively. After performing 100 trials, the best solutions obtained by ACO for 13 and 40 units are 24,169.63 $/h and 121,532.41 $/h, as given in Tables 1 and 2, respectively. These solutions are better than those reported in the literatures, especially in the case of 40 units.

The comparison results of the ACO with other three methods are given in Tables 3 and 4. The results show that the ACO succeeds

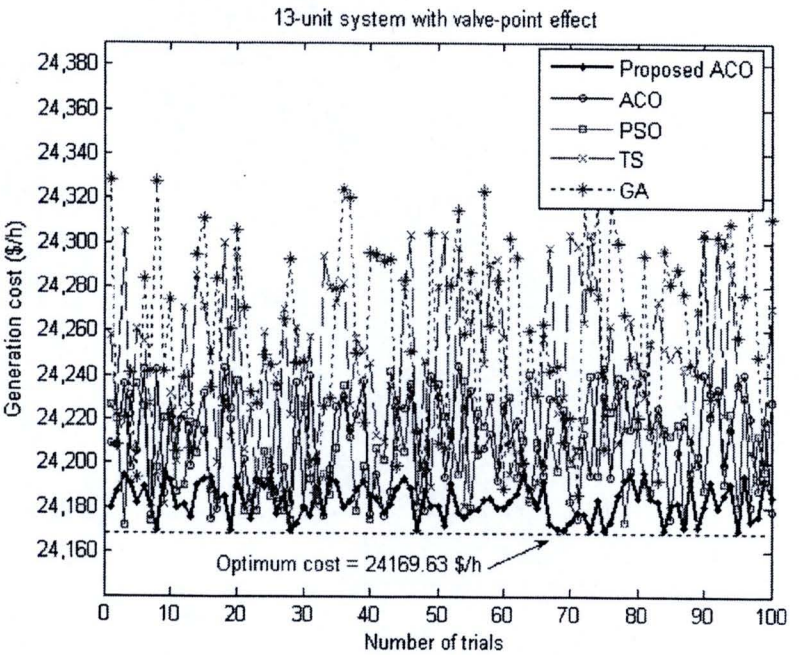

Fig. 4. Distribution of generation costs of 13 generating units.

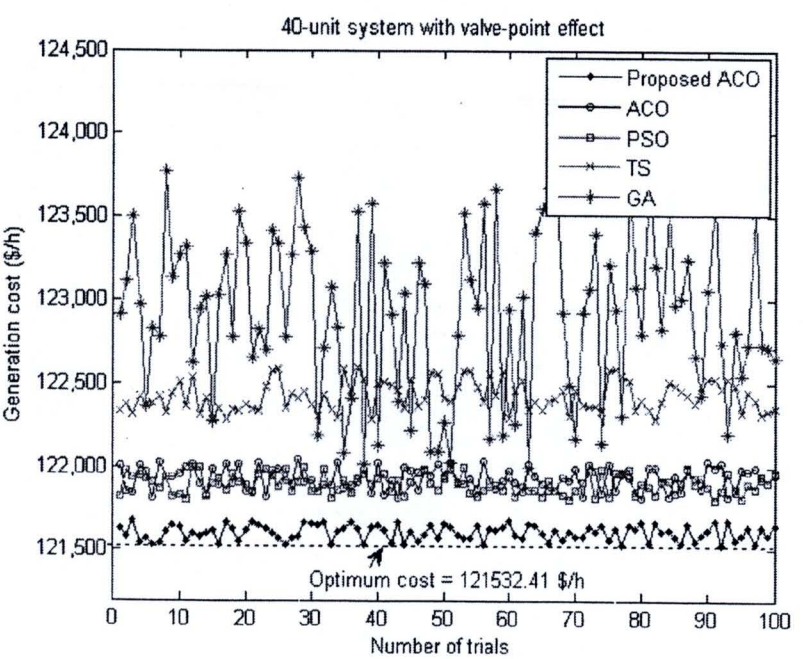

Fig. 5. Distribution of generation costs of 40 generating units.

in finding the best solution. The worst, average, and best values of the generation costs achieved by ACO for 100 runs are much better than those of other methods. Besides, the lowest standard deviation (Std.) in case of ACO indicates the highest robustness of the solutions obtained by ACO.

The distribution outlines of the best solution of each trial for each method are depicted in Figs. 4 and 5. The distribution of the solutions of ACO is smaller than that of other methods especially in case of 40 generating units. These results confirm that the ACO always provides higher quality of solution than other methods.

The convergent characteristics of the ACO in comparison with other methods for two case studies are shown in Figs. 6 and 7, respectively. Clearly, the ACO converges to the optimal solution faster than other methods. As provided in Tables 3 and 4, the average computational time (CPU time) of ACO is shorter than that of other methods.

Table 5 compares the results achieved by ACO with those of other studies reported in the literatures. The generation costs minimized by the ACO are lowest among the results from other methods especially in the 40 units system. These comparison results explicitly confirm the higher solution quality of the ACO.

4.2. ED problem considering multiple-fuel effects

The ACO is applied to the ED problem with 10 generators where the multiple-fuel effects are considered. In this case, the objective

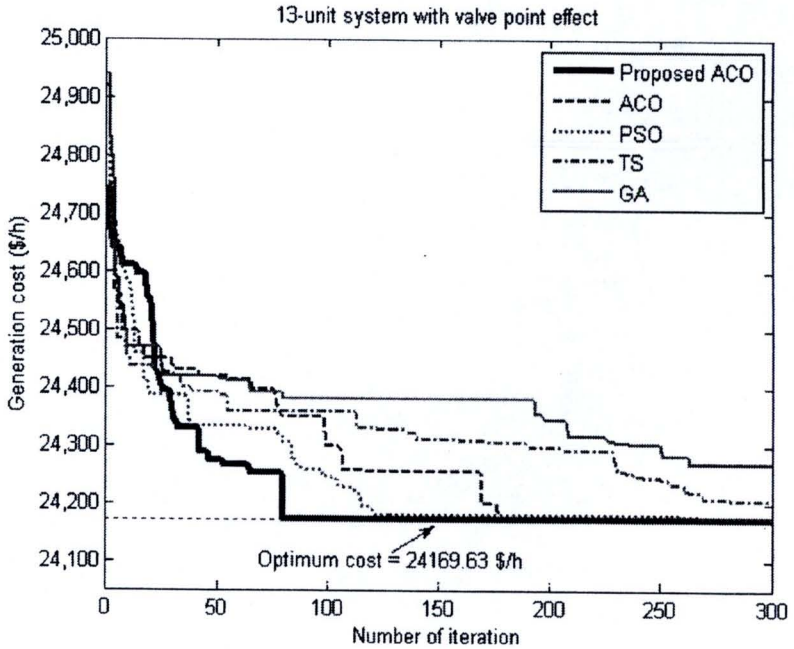

Fig. 6. Convergence curves of 13 generating units.

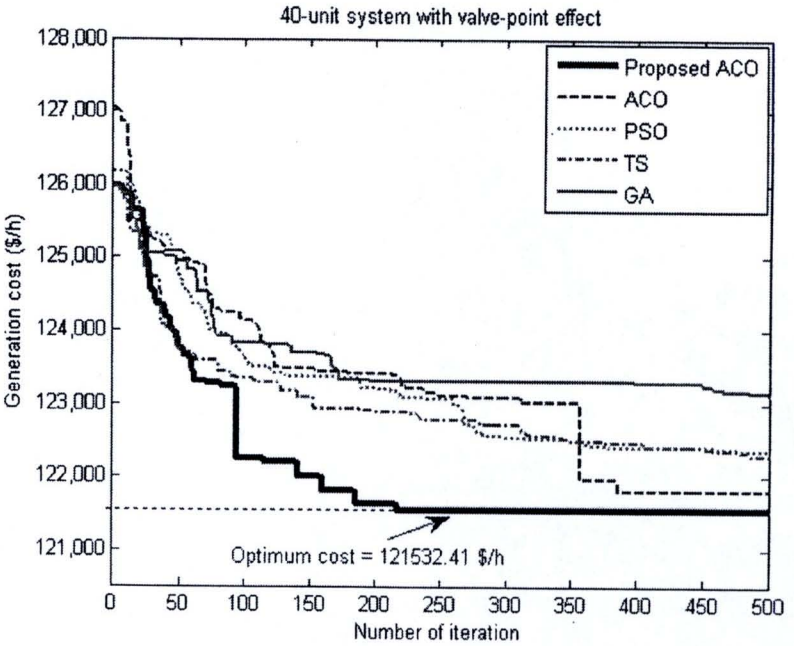

Fig. 7. Convergence curves of 40 generating units.

Table 5
Comparisons results of generation cost presented in the former literatures.

Optimisation technique	13-unit	40-unit
	P_D = 2520 MW	P_D = 10,500 MW
PSO-SQP [10]	24,261.05	–
EP-SQP[10]	24,266.44	–
GA [10]	24,398.23	–
GA-SA [10]	24,275.71	–
IFEP [7]	–	122624.35
FEP [7]	–	122679.71
MPSO [11]	–	122,252.26
DEC(2)-SQP(1) [12]	–	121,741.98
TM [13]	–	122,477.78
EDSA [14]	24,169.92	–
Proposed ACO	24,169.63	121,532.10

Table 6
Best result obtained by ACO for 10-unit system (P_D = 2400 MW).

Unit	Fuel	P_i (MW)	Unit	Fuel	P_i (MW)
1	1	190.3	6	3	232.5
2	1	203.1	7	1	252.8
3	1	253.3	8	3	233.1
4	3	233.1	9	1	320.1
5	1	241.5	10	1	240.2
	Total power output (MW)				2400
	Total generation cost ($/h)				481.6

Table 7
Best results obtained by ACO for 10-unit system (P_D = 2700 MW).

Unit	Fuel	P_i (MW)	Unit	Fuel	P_i (MW)
1	2	221.45	6	3	239.11
2	1	211.53	7	1	284.76
3	1	281.62	8	3	240.70
4	3	239.90	9	3	429.61
5	1	276.99	10	1	274.31
	Total power output (MW)				2700
	Total generation cost ($/h)				623.7

Table 8
Convergence results for 10-unit system (P_D = 2400 MW).

Method	Load demand = 2400 MW				
	Worst	Average	Best	Std.	CPU time
GA	491.28	489.54	488.01	0.95	58.26
TS	491.16	487.53	483.96	2.06	47.45
PSO	481.91	481.81	481.72	0.05	18.32
ACO	482.04	481.93	481.82	0.05	24.15
Proposed ACO	481.70	481.64	481.60	0.02	8.42

Table 9
Convergence results for 10-unit system (P_D = 2700 MW).

Method	Load demand = 2700 MW				
	Worst	Average	Best	Std.	CPU time
GA	626.80	625.41	623.92	0.82	50.22
TS	624.96	624.51	624.01	0.28	18.51
PSO	624.89	624.39	623.81	0.30	7.28
ACO	624.78	624.35	623.90	0.24	8.35
Proposed ACO	624.09	623.90	623.70	0.11	5.16

function is represented by the piecewise quadratic cost function. The input data and related constraints of the test system are given in [13]. In this case, the total system demands are 2400 MW and 2700 MW.

Table 10
Comparisons of case study results for generation cost presented in the literature.

Optimisation technique	2400 MW	2700 MW
IGA [5]	–	624.50
MPSO[11]	481.70	623.81
TM [13]	481.70	623.70
Proposed ACO	481.60	623.70

For cases of load demands 2400 MW and 2700 MW, after performing 100 trials, the best solutions obtained by ACO are given in Table 6 and Table 7. The comparison results of the ACO with other three methods are given in Table 8 and Table 9, respectively. These results signify that the ACO always provides better high quality of solution than other methods. Additionally, the ACO converges to the optimum solution much faster than other methods.

In Table 10, the optimised results obtained by ACO are compared to those of former studies. The generation costs minimized by ACO are lowest among the results from other methods. These comparison results confirm that the ACO provides highest solution quality.

5. Conclusion

In this paper, the ACO algorithm has been proposed to solve the dynamic ED problem with non-smooth cost functions. To improve the search process, three techniques, i.e. priority list, variable reduction, and zoom feature are added to the ACO. Two types of ED problems with the valve-point loading and multiple fuels effects have been used to evaluate the performance of ACO. Additionally, the results of ACO are compared with those obtained by the conventional heuristic approaches, i.e. GA, TS, PSO and ACO. Studied results confirm that the proposed ACO is much superior to other conventional methods in terms of high-quality solution, stable convergence characteristic, and good computation efficiency.

Acknowledgement

This work was supported by the Thailand Research Fund under Basic Research Grant (TRF Advanced Research Scholar) No. BRG 5080019 and the King Mongkut's Institute of Technology Ladkrabang Research Fund.

References

[1] Wang KP, Fung CC. Simulate annealing base economic dispatch algorithm. IEE Proc C 1993;140(6):507–13.
[2] Wong KP, Wong YW. Genetic and genetic/simulated-annealing approaches to economic dispatch. Proc Inst Elect Eng C 1994;141(5):507–13.
[3] Walters DC, Sheble GB. Genetic algorithm solution of economic dispatch with valve point loading. IEEE Trans Power Syst 1993;8:1325–32.
[4] Chen P-H, Chang H-C. Large-scale economic dispatch by genetic algorithm. IEEE Trans Power Syst 1995;10:1919–26.
[5] Chiang C-L. Improved genetic algorithm for power economic dispatch of units with valve-point effects and multiple fuels. IEEE Trans Power Syst 2005;20(4):1690–9.
[6] Yang HT, Yang PC, Huang CL. Evolution programming based economic dispatch for units with non-smooth fuel cost functions. IEEE Trans Power Syst 1996;11(1):112–8.
[7] Sinha N, Chakrabarti R, Chattopadhyay PK. Evolutionary programming techniques for economic load dispatch. IEEE Trans Evolut Comput 2003;7(1):83–94.
[8] Lin W-M, Cheng F-S, Tsay M-T. An improved tabu search for economic dispatch with multiple minima. IEEE Trans Power Syst 2002;17(1):108–12.
[9] Ongsakul W, Dechanupaprittha S, Ngamroo I. Parallel tabu search algorithm for constrained economic dispatch. IEE Proc Gener Transm Distrib 2004;151(2):157–66.
[10] Victoire TAA, Jeyakumar AE. Hybrid PSO-SQP for economic dispatch with valve-point effect. Elect Power Syst Res 2004;71(1):51–9.

[11] Park J-B, Lee K-S, Shin J-R, Lee KY. A particle swarm optimisation for economic dispatch with nonsmooth cost function. IEEE Trans Power Syst 2005;20(1):34–42.
[12] Coelho LS, Mariani VC. Combining of chaotic differential evolution and quadratic programming for economic dispatch optimisation with valve-point effect. IEEE Trans Power Syst 2006;21(2):989–96.
[13] Liu D, Cai Y. Taguchi method for solving the economic dispatch problem with nonsmooth cost functions. IEEE Trans Power Syst 2005;20(4): 2006–14.
[14] Chen C. Non-convex economic dispatch: a direct search approach. Energ Conver Manage 2007;48:219–25.
[15] Coloni A, Dorigo M, Maniezzo V. Distributed optimisation by ant colonies. In: Proceedings of the European Conference on Artificial Life, 1991. p. 134–42.
[16] Dorigo M, Maniezzo V, Colorni A. Ant system: optimisation by a colony of cooperative agents. IEEE Trans Syst Man Cybern B 1996;26(1):29–41.
[17] Dorigoand M, Gambardella LM. Ant colonies for the traveling saleman problem. Biosystems 1997;43:73–81.
[18] Dorigoand M, Gambardella LM. Ant colony system: a cooperative learning approach to the travelling salesman problem. IEEE Trans Evolut Comput 1997;1(1):53–66.
[19] Gambardella LM, Taillard E, Dorigo M. Ant colonies for the quadratic assignment problem. J Oper Res Soc 1999;50:167–76.
[20] Bell J, McMullen P. Ant colony optimisation techniques for the vehicle routing problem. Adv Eng Inform 2004;18:41–8.
[21] Sum-Im T. Economic dispatch by ant colony search algorithm. In: Proceedings of the 2004 IEEE conference on cybernetics and intelligent systems, Singapore, December 2004.
[22] Hou Y-H, Wu Y-W, Lu L-J, Xiong X-Y. Generalized ant colony optimisation for economic dispatch of power systems. In: Proceedings of the International Conference on Power System Technology 2002 (PowerCon 2002), vol. 1; 2002. p. 225–9.

Energy Conversion and Management 51 (2010) 2383–2393

Contents lists available at ScienceDirect

Energy Conversion and Management

journal homepage: www.elsevier.com/locate/enconman

Coordinated SVC and AVR for robust voltage control in a hybrid wind-diesel system

Sitthidet Vachirasricirikul [a,*], Issarachai Ngamroo [b], Somyot Kaitwanidvilai [b]

[a] Department of Electrical Engineering, Faculty of Engineering, King Mongkut's Institute of Technology Ladkrabang, Bangkok 10520, Thailand
[b] Center of Excellence for Innovative Energy Systems, Department of Electrical Engineering, Faculty of Engineering, King Mongkut's Institute of Technology Ladkrabang, Bangkok 10520, Thailand

ARTICLE INFO

Article history:
Received 19 October 2008
Received in revised form 20 August 2009
Accepted 5 May 2010
Available online 3 June 2010

Keywords:
Voltage control
Hybrid wind-diesel power system
Static Var Compensator
Automatic Voltage Regulator
Robust control
Genetic algorithm

ABSTRACT

This paper proposes a robust control of voltage fluctuation due to the variation of reactive loads in an isolated wind-diesel hybrid power system using Static Var Compensator (SVC) and Automatic Voltage Regulator (AVR). The structure of the voltage controller of SVC and AVR is the proportional integral (PI) controller with single input. In the system modeling, a normalized coprime factorization is applied to represent possible unstructured uncertainties in the power system such as variation of system parameters and generating and loading conditions. Based on the H_∞ loop shaping, the performance and robust stability conditions of the control system are formulated as the optimization problem. The genetic algorithm is applied to solve an optimization problem and to achieve PI control parameters of SVC and AVR simultaneously. Simulation studies show the control effect and robustness of the proposed coordinated SVC and AVR.

1. Introduction

Wind power systems are considered economically for supply of electrical energy to remote and isolated areas where utility lines are uneconomical to install due to high costs, right-of-way difficulties or environmental concerns [1,2]. Nevertheless, wind energy is intermittent and fluctuating in nature, power generation from the wind is variable. To alleviate this problem, the wind power generations are generally designed to operate in parallel with diesel generators [3,4]. A wind-diesel hybrid power system is very reliable because the diesel acts as a cushion to take care of variation in wind speed. Currently, there are many projects about the wind-diesel hybrid power system such as the Ramea wind-diesel project [5,6], the wind-diesel power systems in Alaska [7], 525 kW wind-diesel hybrid CHP system [8]. In general, the induction generator is used as an energy conversion device in wind power generation [9]. The major disadvantage of the induction generator is the requirement of reactive power for its operation. Besides, most of loads in the system are naturally inductive. The unbalance in generation and demand of reactive power can cause the severe problem of large voltage fluctuation at the generator terminal. The voltage fluctuation will affect the quality of supply and even may damage the system stability in absence of the proper voltage control.

To overcome this problem, the SVC has been expected to be the cost-effective device for voltage control [10,11]. In the previous works, SVC has been applied to prevention of voltage instability and voltage collapse in power systems [12], enhancement of power system dynamics [13], etc. Especially, in [14–19], SVC has been used to control the generator terminal voltage in the wind-diesel hybrid power system due to the mismatch between reactive power generation and load. In these works, the PI based-voltage controller of SVC optimized by the Lyapunov technique shows satisfactorily control effects. Nevertheless, the control parameters of SVC have been optimized while the control parameters of AVR equipped with the exciter of the diesel generator are fixed. This cannot guarantee the well coordinated control between SVC and AVR. To enhance the coordinated control, the simultaneous optimization of SVC and AVR is expected. Besides, these works do not take system uncertainties such as variation of system parameters, several generating and load conditions, into account in the optimization of control parameters. As a result, the robustness of the SVC controller against system uncertainties cannot be guaranteed. The SVC controller may fail to operate and eventually cannot maintain the system stability.

To enhance the robustness of SVC against system uncertainties, H_∞ control has been applied to design robust controller of SVC [20,21]. The resulted H_∞ controller is complicated, high order and impractical. In power system applications, simple structures such as PI and lead-lag compensator are preferred, because of their simple structure, less number of tuning parameters and low-order. However, tuning of controller parameters to achieve a good performance and robustness is difficult. To tackle this problem, this paper proposes a fixed-structure robust H_∞ loop shaping control to coordinated design of SVC and AVR for robust stabilization of voltage fluctuation in an isolated wind-diesel hybrid power

* Corresponding author. Tel./fax: +66 2326 4550.
E-mail address: sitthidetv@hotmail.com (S. Vachirasricirikul).

0196-8904/$ - see front matter © 2010 Elsevier Ltd. All rights reserved.
doi:10.1016/j.enconman.2010.05.001

Nomenclature

SVC	Static Var Compensator
AVR	Automatic Voltage Regulator
IG	induction generator
DG	diesel generator
SG	synchronous generator
PI	proportional integral
E_M	electromagnetic energy stored in IG
ΔE_M	small change in the stored electromagnetic energy of IG
ΔE_{fd}, ΔE_q, $\Delta E'_q$	small change in the voltages of the exciter, internal armature emf under steady state and transient conditions, respectively
K_A, K_E, K_F, K_R, K_α	voltage regulator, exciter, stabilizer, var regulator and thyristor firing gain constants, respectively
K_P, K_I	proportional and integral controller gain of the VAR regulator, respectively
η_{IG}	efficiency of IG
P_{in}, P_{IG}, Q_{IG}	real power input, real power generated by IG and reactive power required by IG, respectively
P_{SG}, Q_{SG}	real and reactive powers generated by SG, respectively
P_L, Q_L	real and reactive power load demand, respectively
Q_{SVC}	reactive power generated by SVC
B_{SVC}	reactive susceptance of the SVC
ΔB_{SVC}	small change in reactive susceptance of the SVC
T_d	SVC average dead time of zero crossing in a three phase system
T_α	thyristor firing delay time
α, α°	thyristor firing angle and nominal thyristor firing angle
$\Delta\alpha$	small deviation in thyristor firing angle
δ	power angle between terminal voltage and armature internal emf
r_1, x_1, r'_2, x'_2	stator resistance, stator reactance, rotor resistance and rotor reactance referred to the primary side of IG, respectively
R_{eq}, X_{eq}, X_M	equivalent resistance, equivalent reactance and magnetizing reactance of the IG, respectively
S_{IG}	apparent power delivered by the IG
s	slip of the IG
T_E, T_F, T_R	exciter, stabilizer and regulator time constants, respectively
T'_{d0}	direct axis open circuit transient time constant
V	system terminal voltage
ΔV, ΔV_{ref}, ΔV_a, ΔV_f	small change in the voltages of terminal voltage, reference voltage, amplifier output voltage and exciter feedback voltage, respectively
X_d, X'_d	direct axis reactance of SG under steady state and transient state conditions, respectively
Q_c	rating of the SVC
Q_R	system reactive power rating

system. The structure of robust controller of SVC and AVR is specified by a PI controller with single input. To take the robust stability of system into consideration, system uncertainties are modeled by normalized coprime factor [22,23]. To obtain the optimal parameters of PI controllers, the performance and robust stability conditions in the H_∞ loop shaping technique are formulated as the objective function. The genetic algorithm (GA) [24] is applied to solve the optimization problem. Simulation studies show the superior robustness and stabilizing effect of the proposed coordinated SVC and AVR in comparison with that of SVC and AVR in [14].

This paper is organized as follows. First, Section 2 describes the problem of voltage stabilization in the study system. Next the system modeling is explained in Section 3. Subsequently, the proposed fixed-structure robust H_∞ loop shaping control is given in Section 4. Section 5 shows simulation studies. Finally, the conclusion is provided.

2. Problem formulation

Fig. 1 shows the basic configuration of the wind-diesel hybrid power system [14]. The SG equipped with exciter and AVR is considered as the DG set. The IG is connected to the wind energy-conversion system. It is assumed that reactive loads with sudden change have been placed in this isolated system. The change in reactive loads results in a serious problem of large voltage fluctuation in the system. Such voltage fluctuation severely affects the system stability. Furthermore, the life time of machine apparatuses on the load side is reduced. To overcome this problem, the SVC and AVR are installed in the system to control reactive power and minimize voltage fluctuation.

3. System modeling

The linearized model of this system in Fig. 1 is illustrated in Fig. 2. Mathematical modeling of wind-diesel hybrid power system and system parameters are provided in Appendices A and B, respectively. The linearized state equation in Fig. 2 can be expressed as

$$\Delta\dot{X} = A\Delta X + B\Delta U \tag{1}$$

$$\Delta Y = C\Delta X + D\Delta U \tag{2}$$

$$\Delta B_{SVC} = K_{PSVC}(s)\frac{K_\alpha}{1+sT_\alpha}\frac{1}{1+sT_d}(\Delta V_{ref} - \Delta V) \tag{3}$$

$$\Delta V'_a = K_{PAVR}(s)(\Delta V_{ref} - \Delta V - \Delta V_f) \tag{4}$$

$$K_{PSVC}(s) = K_{P1} + \frac{K_{I1}}{s} \tag{5}$$

$$K_{PAVR}(s) = K_{P2} + \frac{K_{I2}}{s} \tag{6}$$

where the state vector $\Delta X = [\Delta E_{fd}, \Delta V_a, \Delta V_f, \Delta E'_q, \Delta V]^T$. ΔE_{fd} is a small change in the voltage of the exciter. ΔV_a is a small change in the amplifier output voltage. ΔV_f is a small change in the exciter

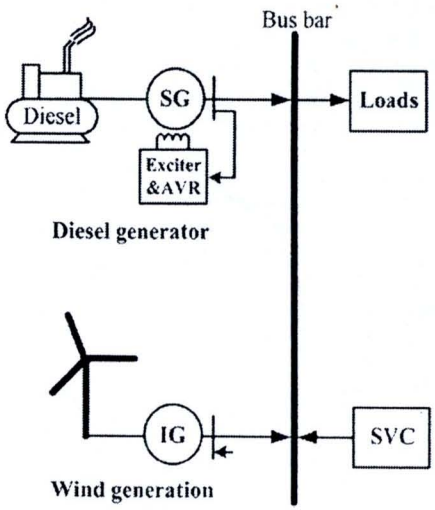

Fig. 1. An isolated wind-diesel hybrid power system.

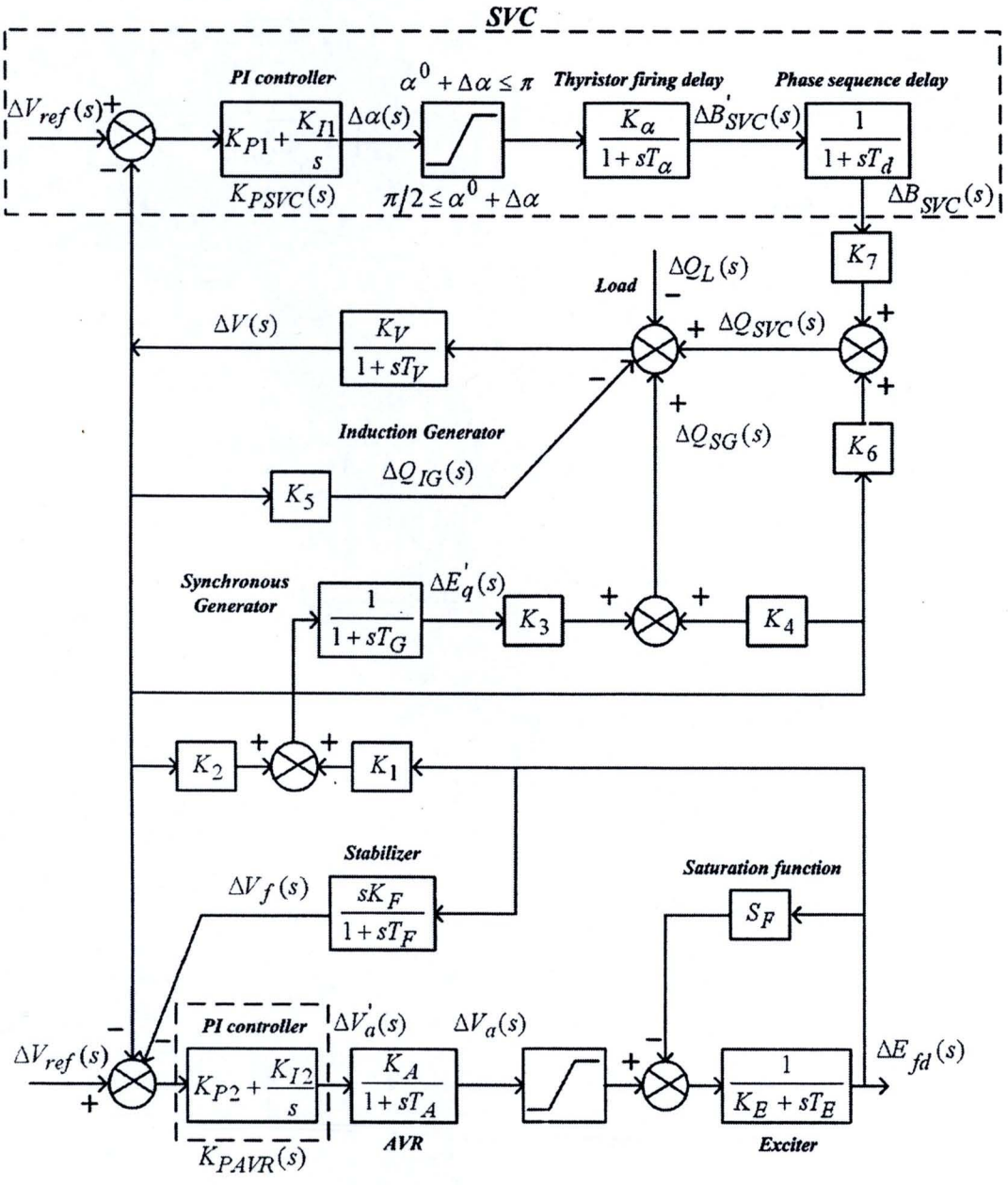

Fig. 2. Linearized block diagram of the wind-diesel hybrid power system.

feedback voltage. $\Delta E'_q$ is a small change in the internal armature emf proportional to the change in the direct axis field flux under transient condition. ΔV is a small change in the terminal voltage. ΔU is the control vector. ΔB_{SVC} and $\Delta V'_a$ are the control signal from SVC and AVR, respectively. ΔY is the output vector. In this paper, the optimization technique based on H_∞ loop shaping is applied to tune the PI controllers of both SVC and AVR simultaneously. The system Eq. (1) is referred to the nominal plant G.

4. Fixed-structure robust H_∞ loop shaping control

It is well known that the order of H_∞ controller depends on that of the plant [22,23]. Generally, H_∞ control design in a large scale power system results in a complicated controller with high order [20,21]. Consequently, it is difficult to implement H_∞ controller in practical power systems. To tackle this problem, the robust control design based on a fixed-structure robust H_∞ loop shaping control is proposed. Here, the robust controller of SVC and AVR is specified by the PI controller. The optimization problem of control parameters is formulated by H_∞ loop shaping technique. Then, GA is used to tune the PI control parameters of SVC and AVR. The flow chart of the proposed design is shown in Fig. 3. Each step is explained as follows.

Step 1. Selection of weighting functions.

The shaped plant G_S is established by weighting functions as shown in Fig. 4. Because the nominal plant is a multi-input single-output (MISO) system, the weighting functions W_1 and W_2 are chosen as

$$W_1 = \begin{bmatrix} K_{W1}\frac{s+a}{s+b} & 0 \\ 0 & K_{W2}\frac{s+c}{s+d} \end{bmatrix}, \quad W_2 = I \tag{7}$$

where K_{W1}, a, b, K_{W2}, c and d are positive values. Because the peak resonance of the nominal plant is in the low frequency range, W_1 is set as a high-pass filter ($a < b, c < d$).

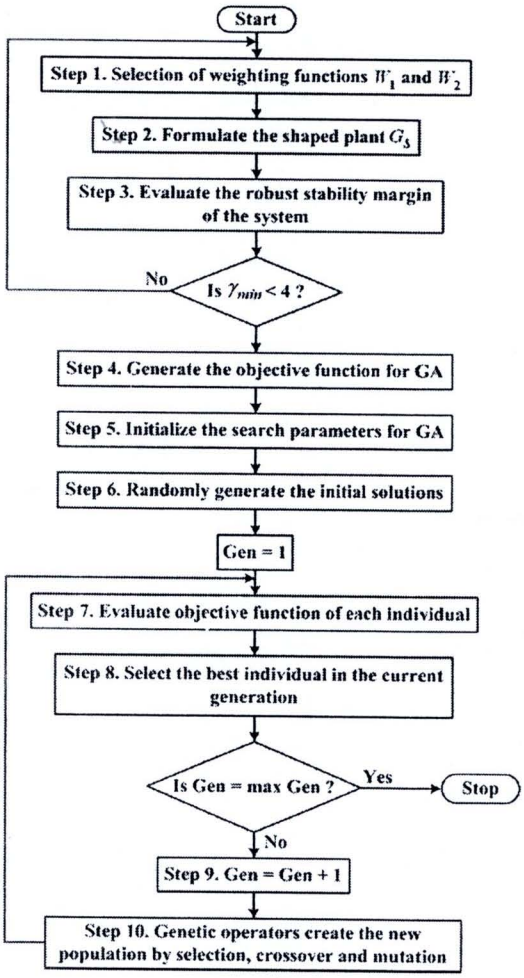

Fig. 3. Flowchart of the proposed design.

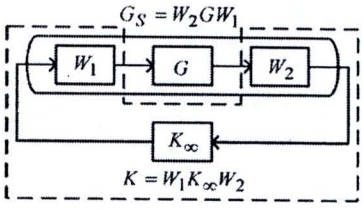

Fig. 4. Shaped plant G_S and robust controller K.

Step 2. Formulate the shaped plant G_S.

As shown in Fig. 4, a pre-compensator, W_1 and a post-compensator, W_2 are employed to form the shaped plant $G_S = W_2GW_1$, which is enclosed by the solid line. The designed robust controller $K = W_1K_\infty W_2$ is enclosed by the dotted line where K_∞ is the H_∞ controller.

Step 3. Evaluate the robust stability margin of the system.

In this work, variation of system parameters, generating and loading conditions, etc., are defined as unstructured system uncertainties. Because these uncertainties cannot be clearly represented by mathematic equations, the coprime factorization is used to represent these unstructured uncertainties. Consequently, a shaped plant G_S is expressed in form of normalized left coprime factor $G_S = M_S^{-1}N_S$, when the perturbed plant G_Δ is defined as [22,23],

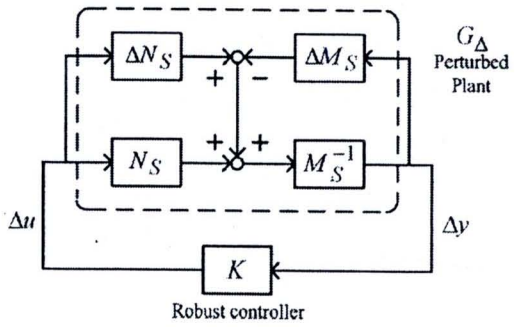

Fig. 5. H_∞ robust stabilization problem.

$$G_\Delta = \{(M_S + \Delta M_S)^{-1}(N_S + \Delta N_S) \ : \ \| \Delta N_S \quad \Delta M_S \| \leqslant 1/\gamma\} \tag{8}$$

where ΔM_S and ΔN_S are stable unknown transfer functions which represent unstructured uncertainties in the nominal plant model G. Based on this definition, the robust stabilization problem can be established by G_Δ and K as depicted in Fig. 5. The objective of the robust control design is to stabilize not only the nominal plant G but also the family of the perturbed plant G_Δ. In Eq. (8), $1/\gamma$ is defined as the robust stability margin. The maximum stability margin in the face of system uncertainties is given by the lowest achievable value of γ, i.e. $\gamma_{\min}$. Hence, $\gamma_{\min}$ implies the largest size of system uncertainties that can exist without destabilizing the closed-loop system in Fig. 5. The value of $\gamma_{\min}$ can be easily calculated from

$$\gamma_{\min} = \sqrt{1 + \lambda_{\max}(XZ)} \tag{9}$$

where $\lambda_{\max}(XZ)$ denotes the maximum eigenvalue of XZ. For minimal state-space realization (A, B, C, D) of G_S, the values of X and Z are unique positive solutions to the generalized control algebraic Riccati equation

$$(A - BS^{-1}D^TC)^TX + X(A - BS^{-1}D^TC) - XBS^{-1}B^TX + C^TR^{-1}C = 0 \tag{10}$$

and the generalized filtering algebraic Riccati equation

$$(A - BS^{-1}D^TC)Z + Z(A - BS^{-1}D^TC)^T - ZC^TR^{-1}CZ + BS^{-1}B^T = 0 \tag{11}$$

where $R = I + DD^T$ and $S = I + D^TD$. Note that no iteration on γ is needed to solve for $\gamma_{\min}$. To ensure the robust stability of the nominal plant, the weighting function is selected so that $\gamma_{\min} < 4.0$ [22,23]. If $\gamma_{\min}$ is not satisfied, then go to step 1, adjust the weighting functions.

Step 4. Generate the objective function for GA optimization.

As shown in Fig. 4, the designed controller K can be represented as

$$K = W_1K_\infty W_2 \tag{12}$$

or

$$K_\infty W_2 = W_1^{-1}K \tag{13}$$

Selecting $W_2 = I$ yields

$$K_\infty = W_1^{-1}K \tag{14}$$

As given in [22,23], the necessary and sufficient condition of the robust controller $K(s)$ is

$$\left\| \begin{bmatrix} I \\ K_\infty \end{bmatrix} (I - G_SK_\infty)^{-1} [I \quad G_S] \right\|_\infty \leqslant \gamma \tag{15}$$

Substituting Eq. (14) in Eq. (15) yields

$$\left\| \begin{bmatrix} I \\ W_1^{-1}K \end{bmatrix} (I - G_SW_1^{-1}K)^{-1} [I \quad G_S] \right\|_\infty \leqslant \gamma \tag{16}$$

As a result, Eq. (16) can be formulated as the objective function in the optimization problem as

$$\text{Minimize} \quad \left\| \begin{bmatrix} I \\ W_1^{-1}K \end{bmatrix} \left(I - G_S W_1^{-1} K\right)^{-1} [I \quad G_S] \right\|_\infty \tag{17}$$

$$\text{Subject to} \quad \begin{aligned} K_{P1,\min} \leqslant K_{P1} \leqslant K_{P1,\max} \\ K_{I1,\min} \leqslant K_{I1} \leqslant K_{I1,\max} \\ K_{P2,\min} \leqslant K_{P2} \leqslant K_{P2,\max} \\ K_{I2,\min} \leqslant K_{I2} \leqslant K_{I2,\max} \end{aligned} \tag{18}$$

where $K_{P1,\min}$ and $K_{P1,\max}$ are minimum and maximum proportional gains of SVC, respectively, $K_{I1,\min}$ and $K_{I1,\max}$ are minimum and maximum integral gains of SVC, respectively. $K_{P2,\min}$ and $K_{P2,\max}$ are minimum and maximum proportional gains of AVR, respectively, $K_{I2,\min}$ and $K_{I2,\max}$ are minimum and maximum integral gains of AVR, respectively.

Step 5. Initialize the search parameters for GA [24].

Define genetic parameters such as population size, crossover, mutation rate and maximum generation.

Step 6. Randomly generate the initial solution. Set the first generation, Gen = 1.

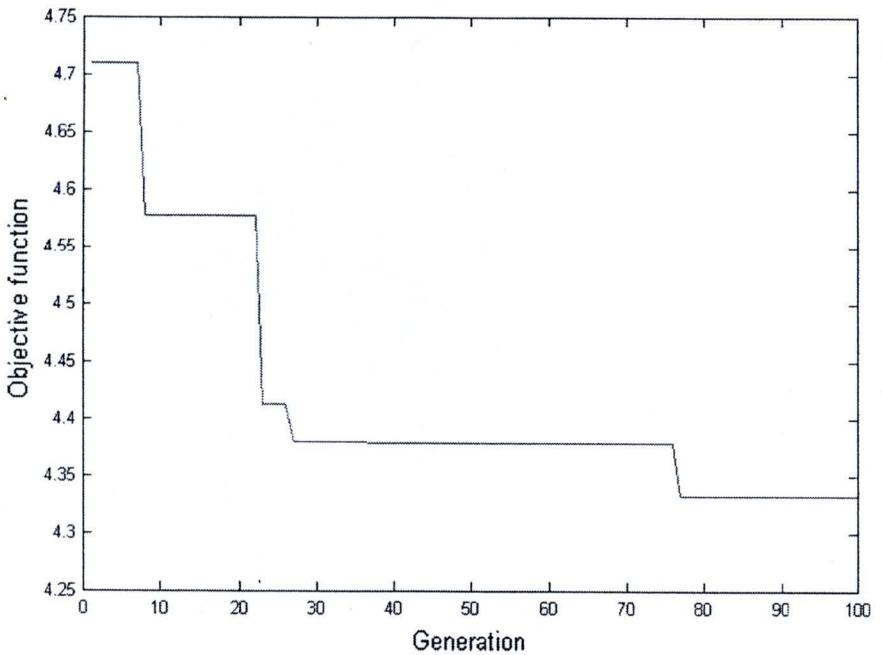

Fig. 6. Convergence curve.

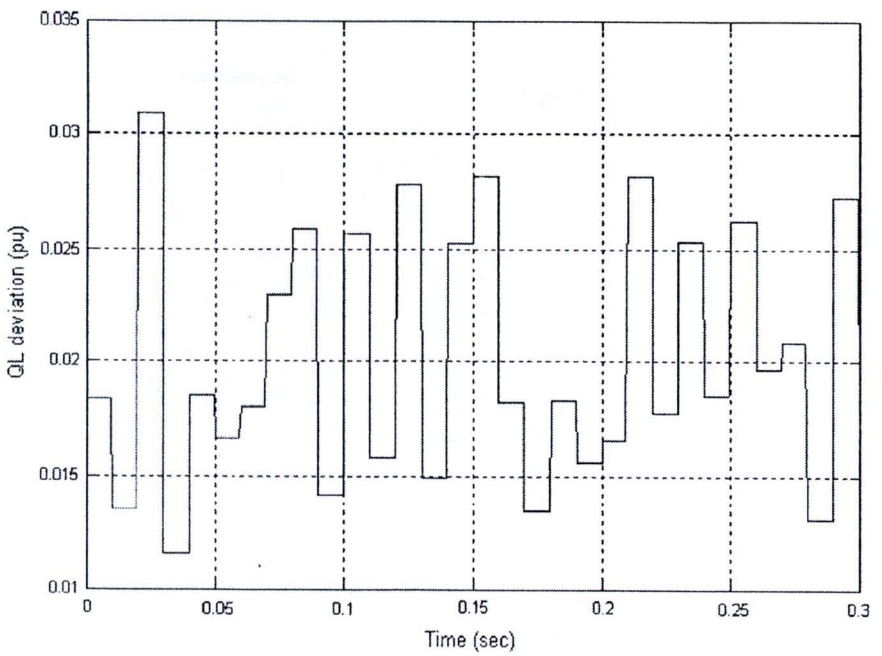

Fig. 7. Random load change.

Step 7. Evaluate objective function of each individual in Eq. (17).

Step 8. Select the best individual in the current generation.

Check the maximum generation. If the current generation is the maximum generation, then stop. If the current generation is less than the maximum generation then go to Step 9.

Step 9. Increase the generation, i.e. Gen = Gen + 1.

Step 10. Create new population using genetic operators and go to step 7.

5. Simulation studies

Here, the designed results of the proposed controller are given as follows. Based on Eq. (7), the weighting functions are appropriately selected as

$$W_1 = \begin{bmatrix} 250\frac{s+20}{s+50} & 0 \\ 0 & 150\frac{s+30}{s+40} \end{bmatrix}, \quad W_2 = I \tag{19}$$

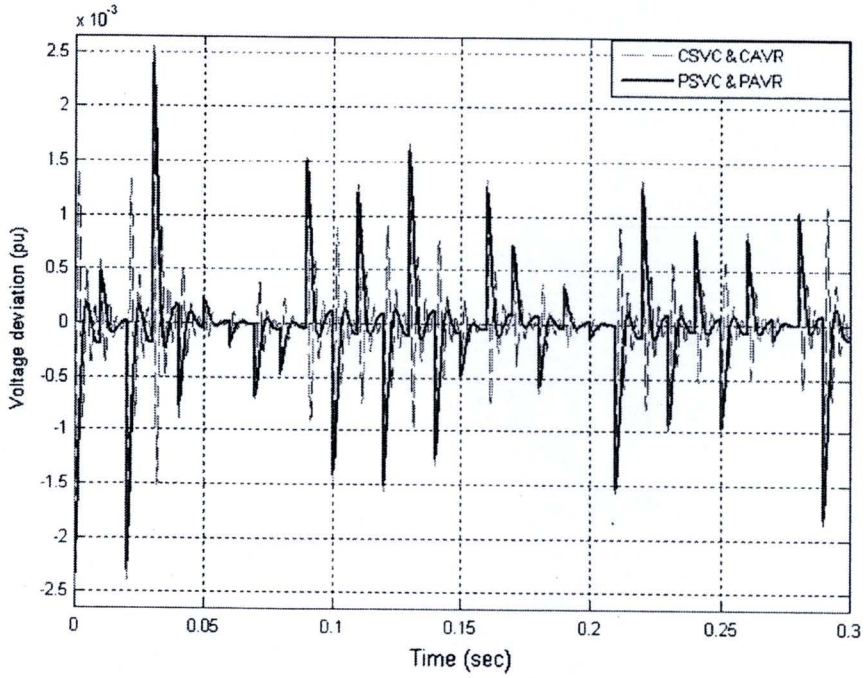

Fig. 8. Transient response of ΔV under the random load change (normal parameters).

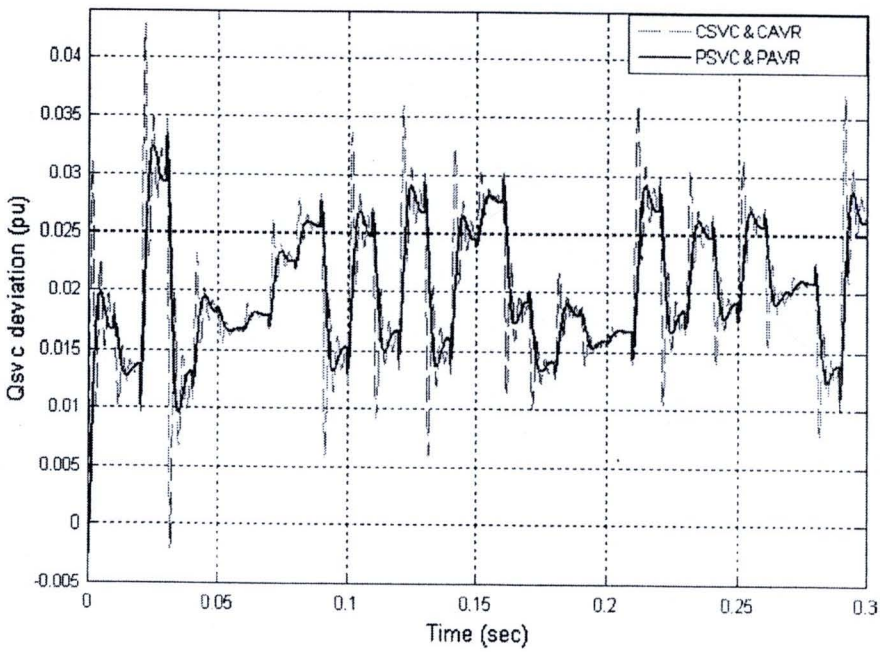

Fig. 9. Transient response of ΔQ_{SVC} under the random load change (normal parameters).

Therefore, the shaped plant G_S can be established. As a result, $\gamma_{min} = 2.7419$. In the GA optimization [24], the ranges of search parameters [14] and GA parameters are set as follows: $K_{P1} \in [1 \quad 575]$, $K_{I1} \in [1 \quad 24{,}000]$, $K_{P2} \in [0.0001 \quad 100]$, $K_{I2} \in [0.0001 \quad 100]$, arithmetic crossover, uniform mutation, population size is 100 and maximum generation is 100. The convergence curve of the objective function is shown in Fig. 6. As a result, the designed PI controllers of SVC and AVR are

$$K_{PSVC}(s) = 80.008 + \frac{8999.8}{s} \tag{20}$$

$$K_{PAVR}(s) = 0.1004 + \frac{0.0099}{s} \tag{21}$$

In simulation studies, the performance and robustness of the proposed SVC and AVR (PSVC & PAVR) are compared with the SVC and AVR in [14] called as "CSVC & CAVR". Note that the PI controller of SVC in [14] is optimized by Lyapunov technique while the AVR parameters are fixed. In addition, the AVR in [14] is not equipped with the PI controller.

Next, it is supposed that the random load change (ΔQ_L) shown in Fig. 7 is applied to the system. Simulation results are depicted in Figs. 8 and 9.

Fig. 8 shows the transient response of a change in the terminal voltage. With random load change, the voltage fluctuation of CSVC & CAVR is very severe. On the other hand, the voltage fluctuation can be stabilized effectively by the PSVC & PAVR. This signifies that the coordinated control effect of the PSVC & PAVR is superior to that of CSVC & CAVR. Fig. 9 also shows that the transient response of reactive power deviation of the proposed SVC is better than that of CSVC.

Next, the robustness of the PSVC & PAVR against the variation of system parameters is evaluated by an integral absolute error (IAE). For 0.3 s of simulation results under random load change in Fig. 7, the IAE of voltage deviation (ΔV) is defined as.

$$\text{IAE of} \Delta V = \int_0^{0.3} |\Delta V| dt \tag{22}$$

Fig. 10 shows the variation of IAE against a change in reactive power required by IG (Q_{IG}). Note that the normal value of Q_{IG} is 0.189 pu. Here, Q_{IG} is varied from 0.189 to 0.55 pu while other system parameters are fixed. Clearly, the IAE in case of CSVC & CAVR increases while Q_{IG} becomes larger. This implies that the large

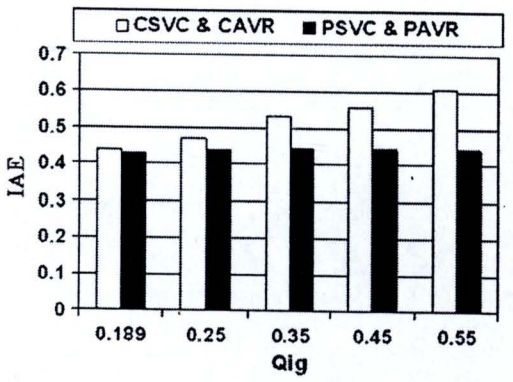

Fig. 10. Variation of IAE against a change in Q_{IG}.

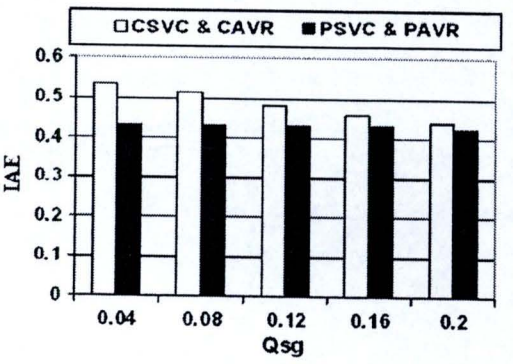

Fig. 11. Variation of IAE against a change in Q_{SG}.

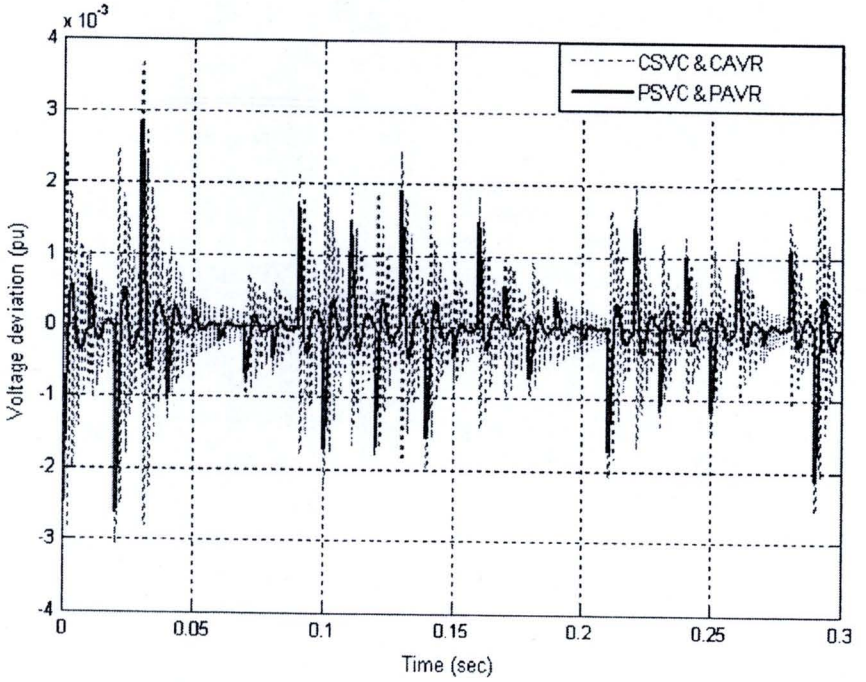

Fig. 12. Transient response of ΔV (changed parameters).

reactive power consumed by IG significantly deteriorates the stabilizing effect of CSVC & CAVR. On the other hand, the IAE of the PSVC & PAVR rarely changes. The stabilizing effect of the PSVC & PAVR is not affected by the large reactive power consumption of IG. This signifies that the PSVC & PAVR are robust to the variation of reactive power consumed by IG.

Fig. 11 depicts the variation of IAE against a change in reactive power generation by SG (Q_{SG}). Note that the normal value of Q_{SG} is 0.2 pu. Here, the reactive power generated by SG is reduced from 0.2 to 0.04 pu while other system parameters are fixed. Clearly, the IAE in case of CSVC & CAVR increases while Q_{SG} is reduced. This implies that the stabilizing effect of CSVC & CAVR is deteriorated at low reactive power generation of SG. On the other hand, the values of IAE of the PSVC & PAVR are almost constant. The robustness of the PSVC & PAVR is higher than that of CSVC & CAVR.

Finally, it is assumed that the reactive power consumptions of load and IG increase while the reactive power generation of SG decreases. This situation results in the voltage drop at the generator terminal. Then, the SVC injects more reactive power to the system. In addition, the AVR tries to increase the terminal voltage by increasing the field flux voltage. This causes an increase in E'_q of SG because E'_q changes proportionally to the change of field flux. Based on the reactive power balance equation, $Q_{SVC} = Q_{IG} + Q_L - Q_{SG}$ [14], it is assumed that the initial values of Q_L, Q_{IG} are increased by 50% while the initial value of Q_{SG} is reduced by 50%. As a result, Q_{SVC} is increased by 50% from the initial value. Besides, E'_q is increased by 5% while V is reduced by 5% from the initial values. Under this situation, the simulation result subjected to the random load in Fig. 7 is shown in Fig. 12. Clearly, the stabilizing effect of CSVC & CAVR is deteriorated. The fluctuation of voltage is very severe. On the other hand, the PSVC & PAVR are able to suppress voltage fluctuation robustly. This result explicitly confirms the superior robustness of the PSVC & PAVR beyond the CSVC & CAVR against system parameters variation.

6. Conclusions

In this paper, the robust voltage control in an isolated wind-diesel hybrid power system based on the fixed-structure robust H_∞ loop shaping control of SVC and AVR has been presented. The normalized coprime factor has been applied to model the power system with unstructured uncertainties. The optimization problem of control parameters based on H_∞ loop shaping control is formulated and solved by GA. The proposed method can be applied to parameter optimization of controller with any simple structure. The resulted controller is robust against system uncertainties. In this study, with simple structure of PI controller of SVC and AVR, the proposed robust voltage controller can be easily implemented in the practical power systems. Simulation results confirm that the robustness of the proposed robust SVC and AVR is much superior to that of the CSVC & CAVR under random load change and variations of system parameters.

Acknowledgements

This work was supported by the Thailand Research Fund under the Basic Research Grant No. BRG5080019 and the King Mongkut's Institute of Technology Ladkrabang Research Fund.

Appendix A

A.1. Mathematical modeling of wind-diesel hybrid power system

A wind-diesel hybrid power system [14–19] is considered for mathematical modeling, where a DG set acts as a local grid for the wind energy-conversion system connected to it. The system also has a SVC to provide the required reactive power in addition to the reactive power generated by SG. Small changes in real power are mainly dependent upon the frequency, whereas a small change in reactive power is mainly dependent on voltage [25]. The excitation time constant is much smaller than the prime-mover time constant, its transient decay much faster and does not affect the load–frequency-control (LFC) dynamic. Thus, cross coupling between the LFC and the automatic-voltage-regulator (AVR) loop is negligible. The reactive power balance equation of the system under steady-state condition is

$$Q_{SG} + Q_{SVC} = Q_L + Q_{IG} \tag{A.1}$$

where Q_{SG} = reactive power generated by SG, Q_{SVC} = reactive power generated by SVC, Q_L = reactive power load demand and Q_{IG} = reactive power required by IG.

For the incremental reactive power balance analysis of the hybrid system, let the hybrid system experiences a reactive power load change of magnitude ΔQ_L. Due to the action of the AVR and SVC controllers, the system reactive power generation increases by an amount $\Delta Q_{SG} + \Delta Q_{SVC}$. The reactive power required by the system will also change due to change in voltage by ΔV. The net reactive power surplus in the system, therefore, equals $\Delta Q_{SG} + \Delta Q_{SVC} - \Delta Q_L - \Delta Q_{IG}$, and this power will increase the system voltage in two ways:

- By increasing the electromagnetic energy absorption (E_M) of the IG at the rate dE_M/dt.
- By an increased reactive load consumption of the system due to increase in voltage.

This can be expressed mathematically as

$$\Delta Q_{SG} + \Delta Q_{SVC} - \Delta Q_L - \Delta Q_{IG} = d\Delta E_M/dt + D_V \Delta V \tag{A.2}$$

The electromagnetic energy stored in the winding of the IG is given by

$$E_M = \frac{1}{2} L_M I_M^2 = \frac{1}{2} L_M (V/X_M)^2 \tag{A.3}$$

where I_M, L_M and X_M are the current drawn, inductance and reactance of the IG, respectively. Considering approximate equivalent circuit model [26], Eq. (A.3) can be further written as

$$E_M = \frac{1}{2} \frac{2\pi f L_M}{2\pi f} (V/X_M)^2 = \frac{X_M}{4\pi f} (V/X_M)^2 = \frac{V^2}{4\pi f X_M} \tag{A.4}$$

where f is system frequency. For nominal conditions, Eq. (A.4) can be written as

$$E_M^0 = \frac{1}{4\pi f X_M} (V^0)^2 \tag{A.5}$$

Dividing Eq. (A.4) by Eq. (A.5), we get

$$\frac{E_M}{E_M^0} = \left(\frac{V}{V^0}\right)^2 \tag{A.6}$$

Now $V = V^0 + \Delta V$ and ΔV is small. Therefore, Eq. (A.6) can be written by neglecting ΔV^2 terms as

$$\frac{E_M}{E_M^0} = \frac{(V^0 + \Delta V)^2}{(V^0)^2} = 1 + 2\frac{\Delta V}{V^0} \tag{A.7}$$

From Eq. (A.7), ΔE_M can be written as

$$\Delta E_M = E_M - E_M^0 = 2\left(\frac{E_M^0}{V^0}\right)\Delta V \tag{A.8}$$

where V^0 and E_M^0 are the nominal values of terminal voltage and electromagnetic energy stored in the IG.

With the increase in voltage, all the connected reactive power loads experience an increase by $D_V = \partial Q_L/\partial V$ (pu kVAR/pu kV). The parameter D_V can be found empirically. The reactive power loads can be expressed in the exponential voltage form as [27,28]

$$Q_L = C_1 V^q \tag{A.9}$$

where C_1 is the constant of the load and the exponent q depends upon the type of load. For small perturbations, Eq. (A.9) can be written as

$$\Delta Q_L/\Delta V = q\left(Q_L^0/V^0\right) \tag{A.10}$$

where Q_L^0 is the nominal value of the reactive power load demand. In Eq. (A.2), D_V can be calculated empirically using Eq. (A.10). Let Q_R be the system reactive power rating. Dividing by Q_R and using Eq. (A.8), Eq. (A.2) can be written as

$$\Delta Q_{SG} + \Delta Q_{SVC} - \Delta Q_L \doteq \Delta Q_{IG} = \left(2E_M^0/\left(V^0 Q_R\right)\right) \times d\Delta V/dt + D_V \Delta V \tag{A.11}$$

In Eq. (A.11), Q_R divides only one term as the other terms are expressed in pu kVAR. The term E_M^0/Q_R can be written as

$$E_M^0/Q_R = 1/4\pi f k_R = H_R \tag{A.12}$$

where H_R is a constant of the system having units of sec and k_R is the ratio of the system reactive power rating to rated magnetizing reactive power of IG. Substituting the value of E_M^0/Q_R from Eq. (A.12) in Eq. (A.11), we get

$$\Delta Q_{SG} + \Delta Q_{SVC} - \Delta Q_L - \Delta Q_{IG} = (2H_R/V^0) \times d\Delta V/dt + D_V \Delta V \tag{A.13}$$

In Laplace form, the state differential equation from Eq. (A.13) can be written as

$$\Delta V(s) = K_V/(1 + sT_V) \times [\Delta Q_{SG}(s) + \Delta Q_{SVC}(s) - \Delta Q_L(s) - \Delta Q_{IG}(s)] \tag{A.14}$$

where

$$T_V = \frac{2H_R}{D_V V^0} \tag{A.15}$$

and

$$K_V = \frac{1}{D_V} \tag{A.16}$$

A.1.1. The flux linkage equation

The flux linkage equation [29] of the round rotor synchronous machine for small perturbation is given as

$$d\Delta E'_q/dt = (\Delta E_{fd} - \Delta E_q)/T'_{d0} \tag{A.17}$$

where ΔE_q = change in the internal armature emf proportional to the change in the direct axis field flux under steady-state condition.

In Eq. (A.17), ΔE_q is given by

$$\Delta E_q = \frac{X_d}{X'_d}\Delta E'_q - \frac{(X_d - X'_d)}{X'_d}(\cos\delta)\Delta V \tag{A.18}$$

For small changes Eq. (A.17), using Eq. (A.18) in Laplace transform form can be written as

$$(1 + sT_G)\Delta E'_q(s) = K_1 \Delta E_{fd}(s) + K_2 \Delta V(s) \tag{A.19}$$

where

$$T_G = X'_d T'_{d0}/X_d \tag{A.20}$$

$$K_1 = X'_d/X_d \tag{A.21}$$

$$K_2 = (X_d - X'_d)\cos\delta/X_d \tag{A.22}$$

A.1.2. The synchronous generator equation

Under transient condition, Q_{SG} is given by [25]

$$Q_{SG} = (E'_q V\cos\delta - V^2)/X'_d \tag{A.23}$$

For small perturbation, Eq. (A.23) can be written as

$$\Delta Q_{SG} = (V\cos\delta/X'_d)\Delta E'_q + \left(\left(E'_q\cos\delta - 2V\right)/X'_d\right)\Delta V \tag{A.24}$$

where $\Delta E'_q$ = change in the internal armature emf proportional to the change in the direct axis field flux under transient condition.

Taking Laplace transform of both sides, we get

$$\Delta Q_{SG}(s) = K_3 \Delta E'_q(s) + K_4 \Delta V(s) \tag{A.25}$$

where

$$K_3 = V\cos\delta/X'_d \tag{A.26}$$

and

$$K_4 = (E'_q\cos\delta - 2V)/X'_d \tag{A.27}$$

A.1.3. IEEE type-1 excitation system equation

As shown in Fig. A1, IEEE type-1 excitation system [30] is considered for the synchronous generator of the hybrid system. From the block diagram, the transfer function equations neglecting saturation function (SF) can be written as

$$\Delta E_{fd}(s) = \frac{1}{K_E + sT_E}\Delta V_a(s) \tag{A.28}$$

$$\Delta V_a(s) = \frac{K_A}{1 + sT_A}(-\Delta V(s) - \Delta V_f(s) + \Delta V_{ref}(s)) \tag{A.29}$$

$$\Delta V_f(s) = \frac{sK_F}{1 + sT_F}\Delta E_{fd}(s) \tag{A.30}$$

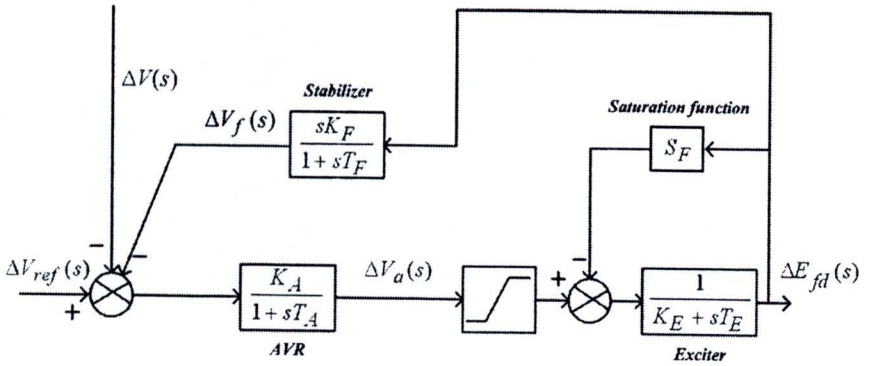

Fig. A1. IEEE type-1 excitation system.

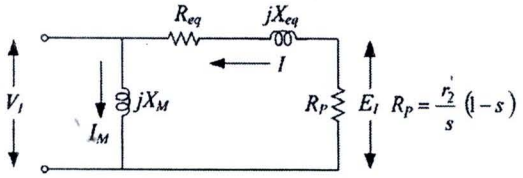

Fig. A2. Equivalent circuit of induction generator.

A.1.4. The induction generator equation

The mathematical model of induction generator [17] is derived as below.

From Fig. A2, the rated current I is given by

$$I = \frac{E - V}{R_{eq} + jX_{eq}} = \frac{E}{R_P} \tag{A.31}$$

Solving for E in Eq. (A.31), we get

$$E = \frac{R_P}{R_Y - jX_{eq}} V \tag{A.32}$$

$$R_Y = R_P - R_{eq} \tag{A.33}$$

Eq. (A.32) can be rewritten as

$$E = \left(\frac{R_P R_Y}{R_Y^2 + X_{eq}^2} + j \frac{R_P X_{eq}}{R_Y^2 - X_{eq}^2} \right) V \tag{A.34}$$

The apparent power delivered by the induction generator is given by

$$S_{IG} = P_{IG} + jQ_{IG} = V \left(\frac{E - V}{R_{eq} + jX_{eq}} \right)^* - j \frac{V^2}{X_M} \tag{A.35}$$

Substituting the value of E from Eq. (A.34) in Eq. (A.35), real and reactive power delivered by the induction generator are given by

$$P_{IG} = \frac{R_Y}{R_Y^2 + X_{eq}^2} V^2 \tag{A.36}$$

$$Q_{IG} = -\left[\frac{X_{eq}}{R_Y^2 + X_{eq}^2} + \frac{1}{X_M} \right] V^2 \tag{A.37}$$

The minus sign indicates the lagging power factor of the induction generator, i.e. the reactive power is absorbed by the induction generator. The real power input to the induction generator is given by

$$P_{in} = R_e E \left(\frac{E - V}{R_{eq} + jX_{eq}} \right)^* \tag{A.38}$$

Substituting the value of E from Eq. (A.32) in Eq. (A.38) and further solving it, we get

$$P_{in} = \frac{R_P}{R_Y^2 + X_{eq}^2} V^2 \tag{A.39}$$

The mechanical power input also account for core losses, friction and windage losses. The term V^2/X_M in Eq. (A.37) is taken care by the electromagnetic energy storage Eq. (A.3) for the modeling. The induction generator absorbs the remaining reactive power and it is given by

$$Q_{IG1} = \frac{V^2}{X_M} - Q_{IG} = \left\{ \frac{X_{eq}}{R_Y^2 + X_{eq}^2} \right\} V^2 \tag{A.40}$$

Now two conditions arise: constant slip and variable slip (in the present case only constant slip case has been considered for the wind-diesel hybrid system). For small perturbation, Eq. (A.40), in the case of constant slip, can be written as

$$\Delta Q_{IG1} = \frac{2VX_{eq}}{R_Y^2 + X_{eq}^2} \Delta V \tag{A.41}$$

Taking Laplace transform of sides of Eq. (A.41), we get

$$\Delta Q_{IG1}(s) = \frac{2VX_{eq}}{R_Y^2 + X_{eq}^2} \Delta V(s) \tag{A.42}$$

In Eq. (A.42), $\Delta Q_{IG1}(s)$ is given by Eq. (A.42) in the case of constant slip. Substituting for R_P and R_{eq} in Eq. (A.33), in terms of the induction generator parameters, we get

$$R_Y = \frac{r_2'}{s}(1 - s) - (r_1 + r_2') = \frac{r_2'}{s}(2r_2' + r_1) \tag{A.43}$$

Eq. (A.42) can be further written as

$$\Delta Q_{IG}(s) = K_5 \Delta V(s) \tag{A.44}$$

where

$$K_5 = \frac{2VX_{eq}}{R_Y^2 + X_{eq}^2} \tag{A.45}$$

$$R_Y = R_P - R_{eq} \tag{A.46}$$

and

$$R_P = \frac{r_2'}{s}(1 - s) \tag{A.47}$$

A.1.5. SVC equation

The reactive power supplied by the SVC is given by [31,32]

$$Q_{SVC} = V^2 B_{SVC} \tag{A.48}$$

For small perturbation, Eq. (A.48) can be written by taking Laplace transform as

$$\Delta Q_{SVC}(s) = K_6 \Delta V(s) + K_7 \Delta B_{SVC}(s) \tag{A.49}$$

where

$$K_6 = 2VB_{SVC} \tag{A.50}$$

and

$$K_7 = V^2 \tag{A.51}$$

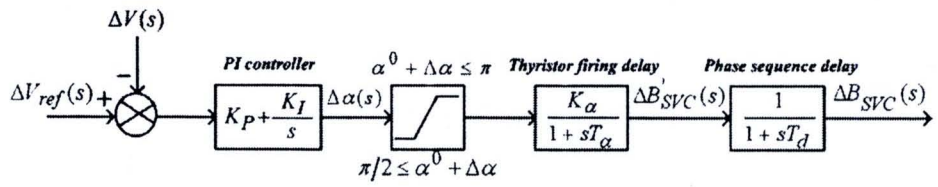

Fig. A3. SVC model.

From Fig. A3, the state equations of the SVC [14] can be written as

$$\Delta B_{SVC}(s) = \frac{1}{1+sT_d}\Delta B'_{SVC}(s) \quad (A.52)$$

$$\Delta B'_{SVC}(s) = \frac{K_\alpha}{1+sT_\alpha}\Delta\alpha(s) \quad (A.53)$$

$$\Delta\alpha(s) = K_P + \frac{K_I}{s}[\Delta V_{ref}(s) - \Delta V(s)] \quad (A.54)$$

Appendix B

See Table B1.

Table B1
Wind-diesel system data.

System parameter	Wind-diesel system
System load/capacity	
Wind capacity (kW)	150
Diesel capacity (kW)	150
Load capacity (kW)	250
Base power (kVA)	250
Synchronous generator	
P_{SG} (pu) (kW)	0.4
Q_{SG} (pu) (kVAR)	0.2
E_q (pu)	1.1136
δ (°)	21.05
E'_q (pu)	0.9603
V (pu)	1.0
X_d (pu)	1.0
X'_d (pu)	0.15
T'_{do} (s)	5.0
Induction generator	
P_{IG} (pu) (kW)	0.6
Q_{IG} (pu) (kVAR)	0.189
P_{in} (pu) (kW)	0.75
η_{IG} (%)	80
$r_1 = r'_2$ (pu)	0.19
$x_1 = x'_2$ (pu)	0.56
s (%)	-4.1
Load	
P_L (pu) (kW)	1
Q_L (pu) (kVAR)	0.75
pf (lag)	0.8
Reactive power data	
$Q_{SVC} = Q_{IG} + Q_L - Q_{SG}$ (pu) (kVAR)	0.739
Q_c (pu) (kVAR)	0.85
α (radians)	2.443985
IEEE type-1 excitation system	
K_A	40
T_A (s)	0.05
K_F	0.5
T_F (s)	0.715
K_E	1.0
S_F (s)	0.0
T_E (s)	0.55
SVC data	
T_α (s)	0.005
T_d (s)	0.001667

References

[1] Ackermann T. Wind power in power systems. John Wiley & Sons Ltd.; 2005.
[2] Mannwell JF, McGowan JG, Rogers AL. Wind energy explained: theory design and application. John Wiley & Sons; 2002.
[3] Hunter R, Elliot G. Wind-diesel systems a guide to technology and its implementation. Cambridge University Press; 1994.
[4] Lipman NH. Wind-diesel and autonomous energy systems. Elsevier Science Publishers Ltd.; 1989.
[5] Abbey C, Katiraei F, Brothers C, Dignard-Bailey L, Joos G. Integration of distributed generation and wind energy in Canada. IEEE Power Eng Soc Meet 2006:1–7.
[6] Barnes M, Ventakaramanan G, Kondoh J, Lasseter R, Asano H, Hatziargyriou N, et al. Real-world microgrids – an overview. IEEE Int Conf Syst Syst Eng 2007:1–8.
[7] http://www.energycentral.com/download/products/AVEC-20519-1.pdf.
[8] http://www.eere.energy.gov/de/pdfs/cs_tdx.pdf.
[9] Simoes MG, Farret FA. Renewable energy systems: design and analysis with induction generators. CRC Press; 2004.
[10] Miller TJE, editor. Reactive power control in electric power systems. John Wiley & Sons; 1982.
[11] Erinmez IA, editor. Static var compensators. CIGRE working group 38-01. Task force no. 2 on SVCs; 1986.
[12] Hammad AE, El-Sadek MZ. Prevention of transient voltage instabilities due to induction motor loads by static var compensators. IEEE Trans Power Syst 1989;4(3):1182–90.
[13] Mohan Mathur R, Varma Rajiv K. Thyristor-based FACTS controllers for electrical transmission systems. Wiley; 2002.
[14] Bansal RC. Automatic reactive-power control of isolated wind-diesel hybrid power systems. IEEE Trans Ind Electron 2006;53(4):1116–26.
[15] Bansal RC. Modelling and automatic reactive power control of isolated wind-diesel hybrid power systems using ANN. Energy Convers Manage 2008;49:357–64.
[16] Bansal RC. Reactive power compensation of wind-diesel hybrid power systems using matlab/simulink. J Energy Technol Policy 2005;3(3):237–52.
[17] Bansal RC, Bhatti TS, Kothari DP. A novel mathematical modelling of induction generator for reactive power control of isolated hybrid power systems. Int J Model Simul 2004;24(1):1–7.
[18] Bansal RC, Bhatti TS, Kothari DP. Automatic reactive power control of isolated wind-diesel hybrid power systems for variable wind speed/slip. Electric Power Compon Syst 2004;32:901–12.
[19] Bansal RC, Bhatti TS. Reactive power control of autonomous wind-diesel hybrid power systems using simulink. Electric Power Compon Syst 2007;35:1345–66.
[20] Zhao Q, Jiang J. Robust SVC controller design for improving power system damping. IEEE Trans Power Syst 1995;10(4):1927–32.
[21] Parniani M, Iravani MR. Optimal robust control design of static var compensator. IEE Proc Gener Trans Distrib 1998;145(3):301–7.
[22] Skogestad S, Postlethwaite I. Multivariable feedback control: analysis and design. 2nd ed. John Wiely; 2005.
[23] Mcfarlane DC, Glover K. Robust controller design using normalized coprime factor plant descriptions. Lecture notes in control and information sciences. Berlin: Springer Verlag; 1990.
[24] Haupt RL, Hault SE. Practical genetic algorithm. 2nd ed. Wiley; 2004.
[25] Elgerd OI. Electric energy system theory an introduction. New Delhi (India): Tata McGraw-Hill; 1982.
[26] Nagrath IJ, Gopal M. Contol systems engineering. 3rd ed. Delhi: New Age International Publishers; 1999.
[27] Ohyama T, Watanabe A, Nishimura K, Tsuruta S. Voltage dependence of composite loads in power systems. IEEE Trans Power Appa Syst 1985;104(1):3064–73.
[28] Al-Alawi SM, Ellithy KA. Tuning of SVC damping controllers over a wide range of load models using an artificial neural network. Electric Power Energy Syst 2000;22:405–20.
[29] Bhatti TS. Interactive excitation and speed governor control of power systems. Ph.D. Dissertation, Electr. Eng. Dept., Indian Inst. Technol., New Delhi, India; May 1984.
[30] IEEE special working group on modelling of excitation systems, excitation system models for power system stability studies. IEEE Trans Power Syst 1981;100(2):494–509.
[31] Padiyar KR. Power systems dynamics stability and control. Bangalore (India): Interline Publishing; 1996.
[32] Bansal RC. Automatic reactive power control of autonomous hybrid power systems. Ph.D. Dissertation, Centre Energy Studies, Indian Inst. Technol., New Delhi, India; December 2002.

International Journal of Emerging Electric Power Systems

Volume 10, *Issue* 2 2009 *Article* 3

Robust Frequency Control of Wind-Diesel Hybrid Power System Using Superconducting Magnetic Energy Storage

Issarachai Ngamroo*

*King Mongkut's Institute of Technology Ladkrabang, Bangkok, ngamroo@gmail.com

Robust Frequency Control of Wind-Diesel Hybrid Power System Using Superconducting Magnetic Energy Storage*

Issarachai Ngamroo

Abstract

In an isolated wind-diesel hybrid power system, the variable power consumptions as well as the intermittent wind power may cause a large fluctuation of system frequency. If the system frequency can not be controlled and kept in the acceptable range, the system may lose stability. To reduce system frequency fluctuation, a superconducting magnetic energy storage (SMES) which is able to supply and absorb active power quickly, can be applied. In addition, variation of system parameters, unpredictable power demands and fluctuating wind power etc., cause various uncertainties in the system. A SMES controller which is designed without considering such uncertainties may lose control effect. To enhance the robustness of SMES controller, this paper focuses on a new robust control design of SMES for frequency control in a wind-diesel system. The coprime factorization is used to represent the unstructured uncertainties in a system modeling. The structure of a SMES controller is the practical first-order lead-lag compensator. To tune the controller parameters, the optimization problem is formulated based on loop shaping technique. The genetic algorithm is applied to solve the problem and achieve the control parameters. Simulation results confirm the high robustness of the proposed SMES controller with small power capacity against various disturbances and system uncertainties in comparison with SMES in the previous research.

KEYWORDS: frequency control, wind-diesel power system, superconducting magnetic energy storage, system uncertainties, loop shaping control, genetic algorithm

---

*This work was supported by The King Mongkut's Institute of Technology Research Fund.

1. Introduction

Wind power systems are considered economically for supply of electrical energy to remote and isolated areas where utility lines are uneconomical to install due to high costs, right of way difficulties or environmental impacts [1,2]. Since wind power sources are naturally fluctuating or intermittent, they are generally integrated with the diesel generation [3,4]. The hybrid wind-diesel power generation provides high reliability of the system to supply power to the isolated load. Nevertheless, the active power demands of the isolated community change frequently, the mismatch between the generation and load causes the large and severe deviation of system frequency. If the frequency deviation can not be controlled and kept in the acceptable range, system equipments may get damaged. Furthermore, the system may lose stability [5,6].

Different technologies such as flywheel [7], battery energy storage [8], superconducting Magnetic Energy Storage (SMES) [9], etc., can be adopted to alleviate system frequency fluctuation in isolated systems [10,11] and a grid connected systems [12,13]. Among of them, a SMES unit which is able to supply and absorb active power rapidly, has been highly expected as one of the most effective controller of system frequency [14,15]. Especially, the application of SMES to control frequency in a hybrid wind-diesel power system due to load changes has been presented in [16,17]. Even the SMES in [16,17] shows satisfactorily frequency control effect, it may not be able to tolerate system uncertainties such as variation of system parameters, random load changes, fluctuating wind power input etc. As a result, the SMES may lose control effect and fail to reduce frequency fluctuation. To enhance the robustness of the SMES controller against system uncertainties, a robust frequency controller of SMES is highly expected.

This paper proposes a new robust frequency controller of SMES in a hybrid wind-diesel power system. To take system uncertainties mentioned above into account in the control design, the normalized coprime factorization [18,19] is applied to represent all unstructured uncertainties in the system modeling. In this study, the configuration of the frequency controller of SMES is the first-order lead/lag compensator. The performance and stability conditions in the H_∞ loop shaping method [18,19] are applied to formulate the optimization problem. To achieve the controller parameters, the genetic algorithm (GA) [20] is used to solve the optimization problem. Simulation studies are carried out to confirm the superior robustness of the proposed SMES against system uncertainties in comparison with the SMES in [16].

This paper is organized as follows. Section 2 describes the frequency control problem in the study system. Next, the mathematical modeling of the study system is explained in Section 3. Subsequently, Section 4 presents the

proposed control design. In Section 5, simulation studies are shown. Finally, the conclusion is given.

2. Problem Formulation

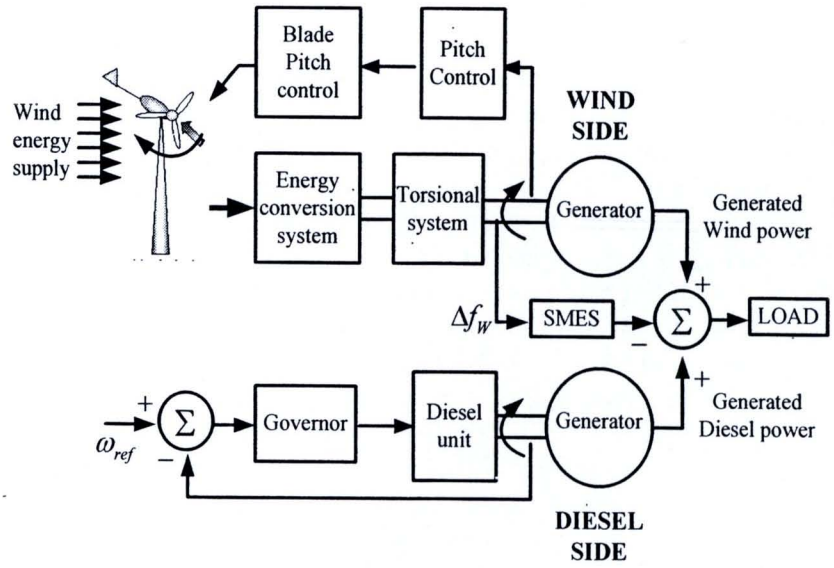

Fig. 1. Basic configuration of a hybrid wind-diesel power generation with SMES.

Fig. 1 shows the basic configuration of the hybrid wind-diesel power system which includes a SMES unit [16,17]. In addition to the random wind energy supply, it is assumed that loads with sudden change have been placed in this isolated system. Variation of wind power and load change results in a serious problem of large frequency fluctuation in the system. Such frequency fluctuation severely affects the system stability. Furthermore, the life time of machine apparatuses on the load side is reduced. To tackle this problem, the SMES is installed in the system to compensate for power variations and minimize frequency fluctuation.

3. Mathematical Modelling

The linearized model of a system in Fig.1 is shown in Fig.2 [16,17]. This model consists of a wind dynamic model, a diesel dynamic model, a SMES unit, a blade pitch control of wind turbine and a generator dynamic with governor model. The details of all subsystems are explained in [16,17]. The state equation of this system can be represented by

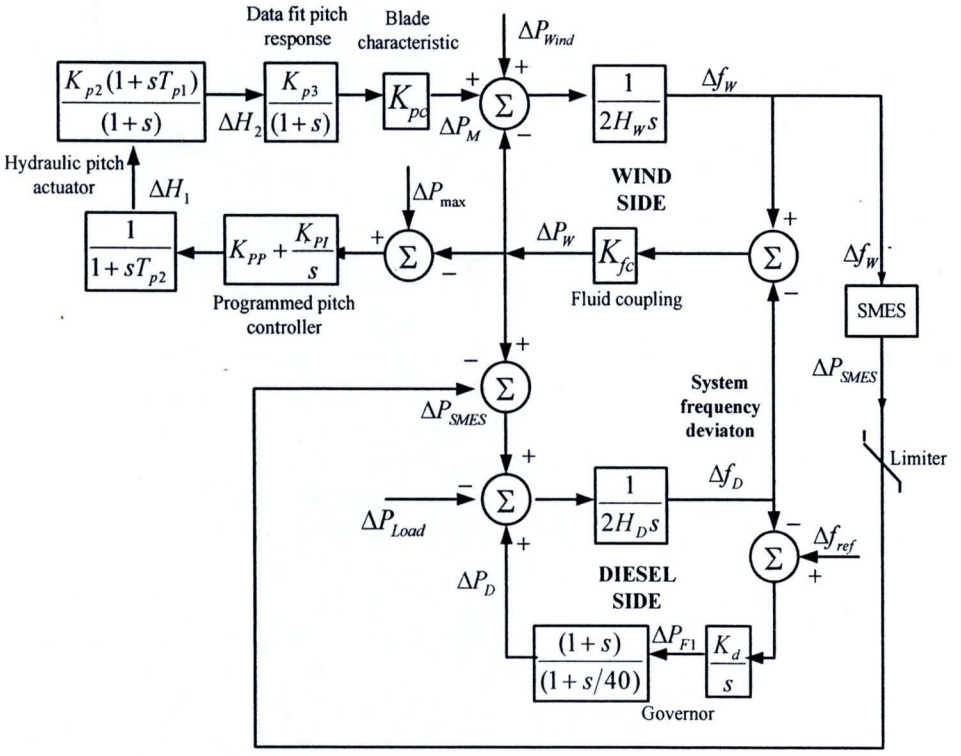

Fig. 2. Block diagram of a hybrid wind-diesel power generation with SMES.

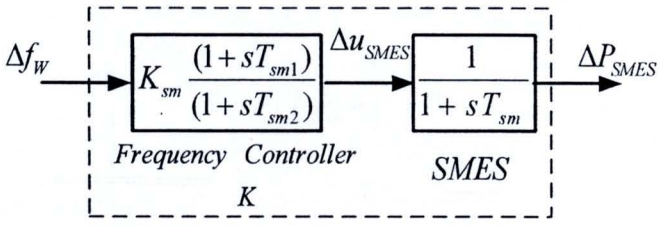

Fig. 3. Block diagram of SMES with the frequency controller K.

$$\Delta\dot{X} = A\Delta X + B\Delta P_{SMES} \tag{1}$$

As shown in Fig. 3, the block diagram of SMES [9] consists of two transfer functions connected in series, i.e. the SMES model and the frequency controller. The SMES can be modeled by the first-order transfer function with

time constant $T_{sm} = 0.03$ s. For the frequency controller, it is practically represented by a lead/lag compensator with first-order. In the controller, there are three control parameters i.e., K_{sm}, T_{sm1} and T_{sm2}. The input signal of the controller is only the frequency deviation of the wind side (Δf_W). Note that, this linearized model can be used to design and evaluate the controller performance and robustness against the small disturbances only. To include a full nonlinear model of the system and simulate large disturbances over various operating conditions, the author has already proposed a robust SMES controller in [21].

4. Proposed Control Design

The objective of the control design is to optimize three control parameters so that the resulted controller is robust to system uncertainties. Based on the H_∞ loop shaping control [18,19], the optimization problem can be formulated. Subsequently, the GA is applied to solve the problem. The flow chart of the proposed design is shown in Fig. 4. The design step in the flow chart can be explained as follows.

Step 1 Selection of weighting functions

As in the conventional H_∞ loop shaping design, first the shaped plant G_S is established by weighting functions W_1 and W_2 as depicted in Fig. 5. Because the nominal plant G is an Single Input Single Output (SISO) system, the weighting functions W_1 and W_2 are chosen as

$$W_1 = K_W \frac{s+a}{s+b} \text{ and } W_2 = 1 \tag{2}$$

Where K_W, a and b are positive values. Because, the frequency control problem is in a vicinity of low frequency (<1 Hz) [16,17], W_1 is set as a high-pass filter $(a < b)$.

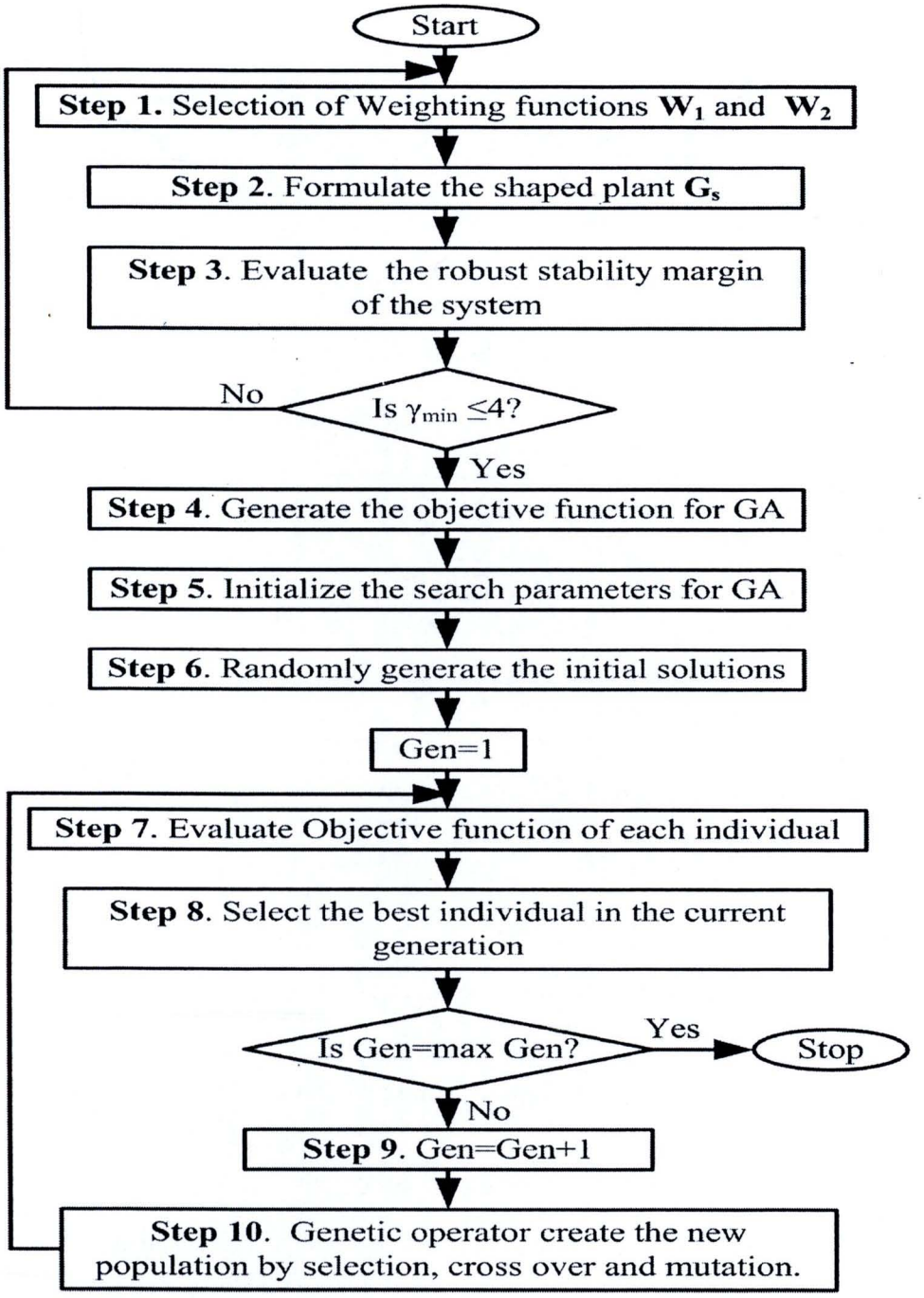

Fig. 4. Flow chart of the proposed design.

Step 2 Formulate the shaped plant G_S.

As shown in Fig. 5, a pre-compensator W_1 and a post-compensator W_2 are employed to form the shaped plant $G_S = W_2 G W_1$, which is enclosed by a solid line. The designed robust controller $K = W_1 K_\infty W_2$ is enclosed by a dotted line where K_∞ is the H_∞ controller.

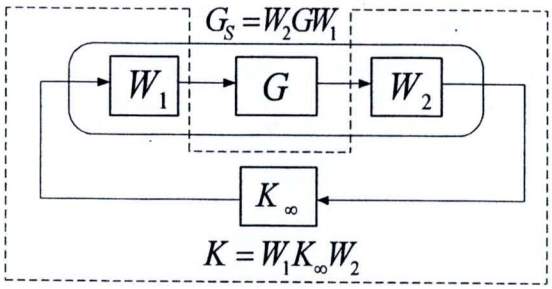

Fig. 5. Shaped plant G_S and designed robust controller K.

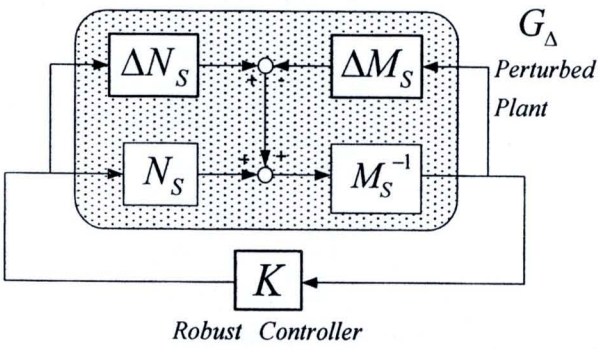

Fig. 6. Robust control problem.

Step 3 Evaluate the robust stability margin of the system

In this work, variation of system parameters, unpredictable load demands and fluctuating wind power etc., are defined as system uncertainties. Because, these uncertainties can not be clearly represented by mathematic equations, the coprime factorization is used to represent these unstructured uncertainties. Consequently, a

shaped plant G_S is expressed in form of normalized left coprime factor $G_S = M_S^{-1} N_S$, when the perturbed plant G_Δ is defined as

$$G_\Delta = \left\{ \left(M_S + \Delta M_S\right)^{-1} \left(N_S + \Delta N_S\right) \ : \ \left\| \Delta N_S \quad \Delta M_S \right\| \ \leq \ 1/\gamma \right\} \qquad (3)$$

Where ΔM_S and ΔN_S are stable unknown transfer functions which represent unstructured uncertainties in the nominal plant model G. Based on this definition, the robust control problem can be established by G_Δ and K as depicted in Fig. 6. The objective of robust control design is to stabilize not only the nominal plant G but also the family of perturbed plant G_Δ. In (3), $1/\gamma$ is defined as the robust stability margin. The maximum stability margin in the face of system uncertainties is given by the lowest achievable value of γ, i.e. $\gamma_{\min}$. Hence, $\gamma_{\min}$ implies the largest size of system uncertainties that can exist without destabilizing the closed-loop system in Fig. 6. The value of $\gamma_{\min}$ can be easily calculated from

$$\gamma_{\min} = \sqrt{1 + \lambda_{\max}\left(XZ\right)} \qquad (4)$$

Where $\lambda_{\max}(XZ)$ denotes the maximum eigenvalue of XZ. For minimal state space realization *(A, B, C, D)* of G_S, the values of X and Z are unique positive solutions to the generalized control algebraic Riccati equation

$$(A - BS^{-1}D^T C)^T X + X(A - BS^{-1}D^T C) - XBS^{-1}B^T X + C^T R^{-1} C = 0 \qquad (5)$$

and the generalized filtering algebraic Riccati equation

$$(A - BS^{-1}D^T C)Z + Z(A - BS^{-1}D^T C)^T - ZC^T R^{-1} CZ + BS^{-1}B^T = 0 \qquad (6)$$

Where $R = I + DD^T$ and $S = I + D^T D$. Note that no iteration on γ is needed to solve for $\gamma_{\min}$. To ensure the robust stability of the nominal plant, the

weighting function is selected so that $\gamma_{\min} \leq 4$ [18, 19]. If $\gamma_{\min}$ is not satisfied, then go to step 1, adjust the weighting functions.

Step 4 Formulate the objective function for GA optimization.

In this study, the performance and robust stability conditions in H_∞ loop shaping design approach are adopted to design a robust frequency controller K in Fig.3. The frequency controller is represented by

$$K = K_{sm}\left(\frac{1+sT_{sm1}}{1+sT_{sm2}}\right) \tag{7}$$

The control parameters K_{sm}, T_{sm1} and T_{sm2} are optimized by GA. The objective function is derived based on the following concept. As shown in Fig. 5, the designed controller K can be represented as

$$K = W_1 K_\infty W_2 \tag{8}$$

or

$$K_\infty W_2 = W_1^{-1} K \tag{9}$$

Selecting $W_2 = 1$ yields

$$K_\infty = W_1^{-1} K \tag{10}$$

As given in [18, 19], the necessary and sufficient condition of the designed robust controller K is

$$\left\| \begin{bmatrix} I \\ K_\infty \end{bmatrix} \left(I - G_S K_\infty\right)^{-1} \begin{bmatrix} I & G_S \end{bmatrix} \right\|_\infty \leq \gamma \tag{11}$$

Substituting (10) into (11) yields

$$\left\| \begin{bmatrix} I \\ W_1^{-1}K \end{bmatrix} \left(I - G_S W_1^{-1} K\right)^{-1} \begin{bmatrix} I & G_S \end{bmatrix} \right\|_\infty \leq \gamma \tag{12}$$

Equation (12) implies that if the ∞-norm of transfer function matrix in the left side is lower than γ, the robust controller K can be obtained. As a result, the ∞-norm of the left side term in (12) can be used to formulate the optimization problem as

$$\text{Minimize} \quad \left\| \begin{bmatrix} I \\ W_1^{-1}K \end{bmatrix} \left(I - G_S W_1^{-1} K\right)^{-1} \begin{bmatrix} I & G_S \end{bmatrix} \right\|_\infty \tag{13}$$

$$\text{Subject to} \quad 1.0 \leq K_{sm} \leq 50.0$$

$$0.001 \leq T_{sm1} \leq 1.0 \tag{14}$$

$$0.001 \leq T_{sm2} \leq 1.0$$

This optimization problem is solved by GA [20].

Step 5 Initialize the search parameters for GA. Define genetic parameters such as population size, crossover, mutation rate, and maximum generation.

Step 6 Randomly generate the initial solution. Set the first generation, Gen = 1.

Step 7 Evaluate objective function of each individual in (13).

Step 8 Select the best individual in the current generation. Check the maximum generation. If the current generation is the maximum generation, then stop. If the current generation is less than the maximum generation then go to Step 9.

Step 9 Increase the generation, i.e. Gen = Gen + 1.

Step 10 Create new population using genetic operators and go to step 7.

5. Simulation Studies

The linearized system in Fig. 2 is used for simulation studies. System parameters [16] are given in the appendix. Here, the designed results of the robust frequency controller of SMES based on the proposed method are explained as follows. As given in (2), the weighting functions are selected as

$$W_1 = 658\left(\frac{s+100}{s+447}\right), \quad W_2 = 1 \tag{15}$$

Accordingly, the shaped plant G_S can be established. As a result, $\gamma_{\min} = 1.3$. In the optimization, the GA parameters are set as follows; population size = 100, crossover probability = 0.6, mutation probability = 0.05, maximum generation = 100. Consequently, the convergence curve of the objective function can be shown in Fig. 7. The designed robust frequency controller of SMES is

$$K(s) = 48.9\left(\frac{0.9433s+1}{0.5828s+1}\right) \tag{16}$$

Fig. 8 shows the bode plots of system with and without SMES. It can be seen that the peak resonance of the system without SMES occurs in the low frequency range. With the proposed SMES, the resonance is damped significantly. This implies the control effect of the designed SMES controller.

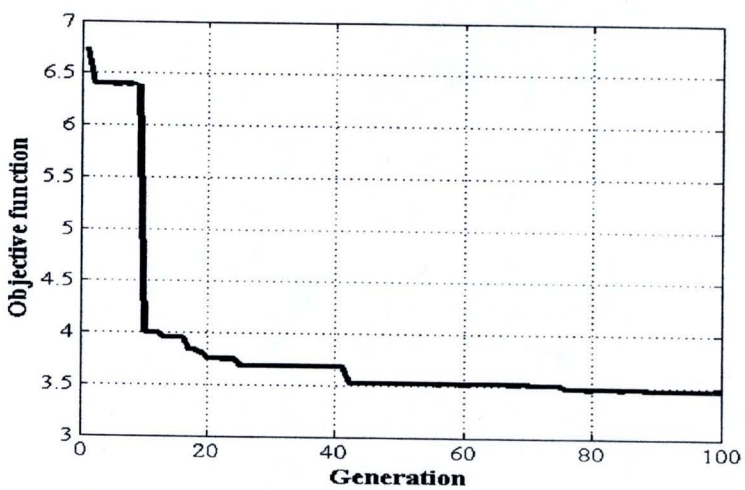

Fig. 7. Convergence curve of the objective function.

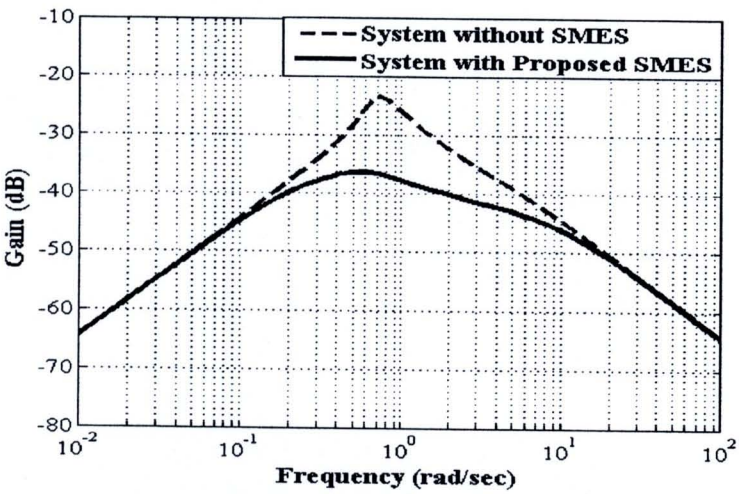

Fig. 8. System with and without SMES.

In simulation studies, the proposed robust controller of SMES is compared with the SMES in [16]. Note that, to determine the kW capacity of SMES, the limiter -0.01 pukW $\leq \Delta P_{SMES} \leq 0.01$ pukW on a system base 350 kW is added to the output of SMES. Simulation results under 4 case studies are carried out as follows.

Case 1: Step increase in wind power or load change

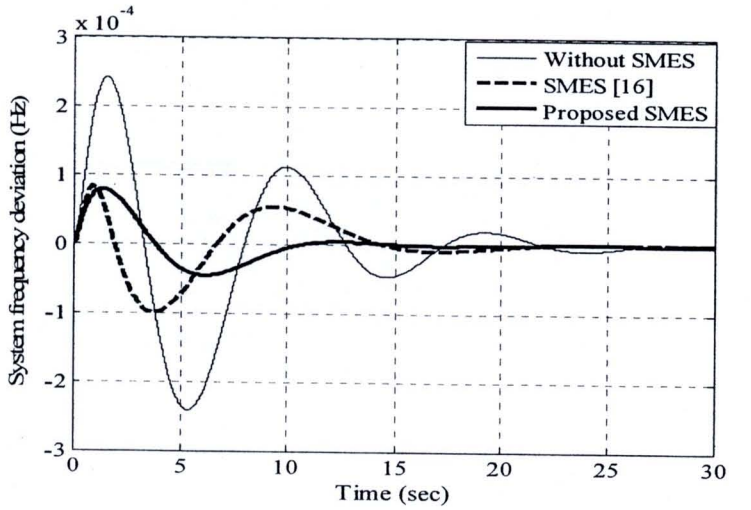

Fig. 9. System frequency deviation against a step increase of wind power.

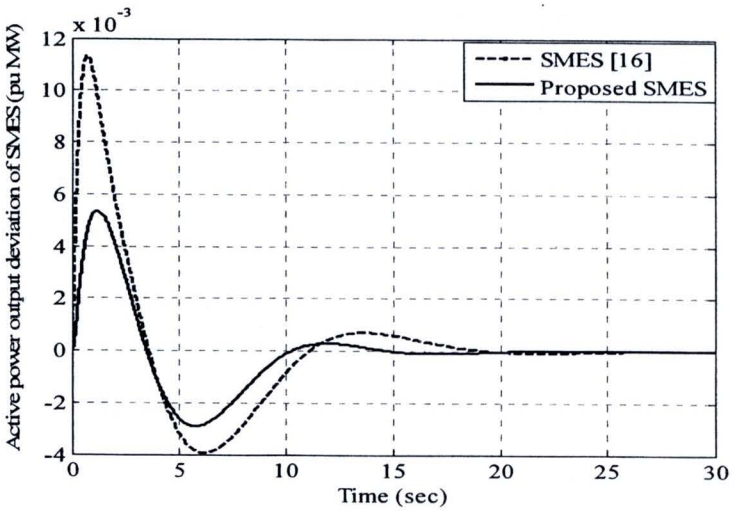

Fig. 10. Power output deviation of SMES against a step increase of wind power.

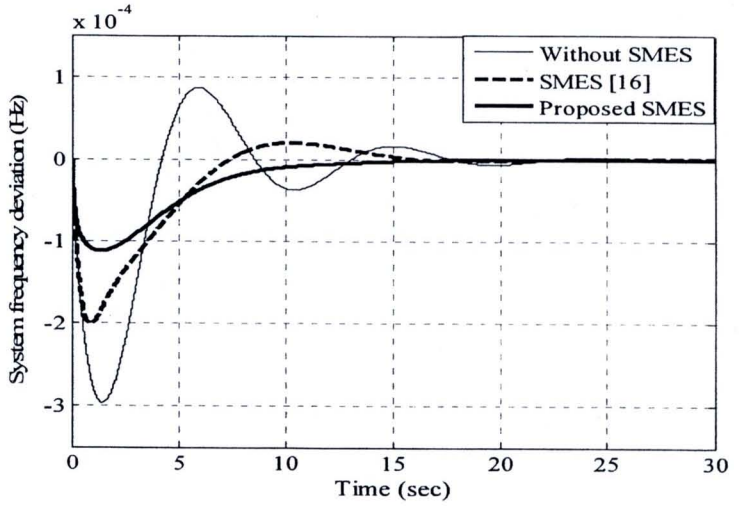

Fig. 11. System frequency deviation against a step increase in load.

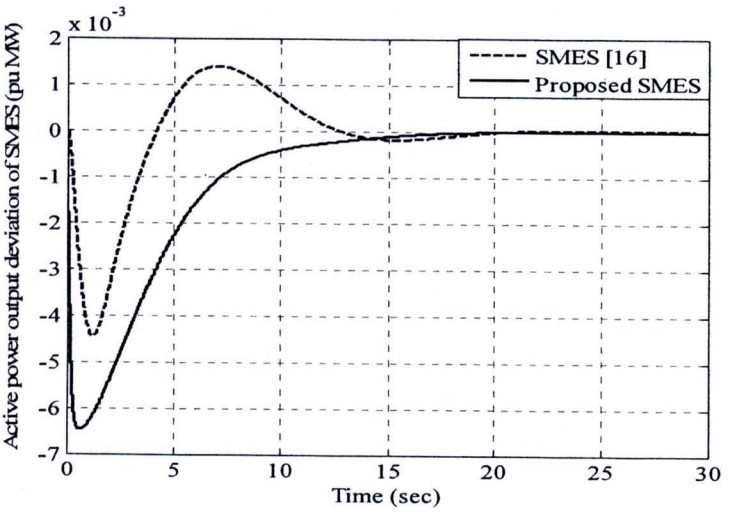

Fig. 12. Power output deviation of SMES against a step increase in load.

First, a 0.01 pukW step increase in the wind power input is applied to the system at t = 0.0 s. Fig. 9 shows the frequency deviation of the diesel generation side which represents the system frequency deviation. Without SMES, the system frequency highly oscillates and the peak frequency deviation is very large. The frequency oscillation takes about 30 s. to reach zero. This indicates that the pitch controller in the wind side and the governor in the diesel side are not able to work well. On the other hand, the peak frequency deviation is reduced significantly and returns to zero within shorter period in case of SMES [16] and the proposed SMES. The power output deviations of both SMESs are shown in Fig.10. The peak power output of the proposed SMES is lower than that of the SMES [16].

Next, a 0.01 pukW step increase in the load power is applied to the system at t = 0.0 s. As depicted in Fig.11, both SMES [16] and the proposed SMES are able to damp the frequency deviation quickly in comparison to without SMES case. As depicted in Fig.12, power output deviations of both SMESs are in the limit. These results show that both SMES [16] and the proposed SMES have almost the same frequency control effects under normal system parameters.

Case 2: Random wind power input.

In this case, the system is subjected to the random wind power input as shown in Fig.13. The system frequency deviations under normal system parameters are shown in Fig.14. By the proposed SMES, the frequency deviation is lower than that in case of SMES [16].

Next, the robustness of frequency controller is evaluated by an Integral Absolute Error (IAE) against the variation of system parameters. For 60 seconds of simulation study under the same random wind power in Fig.13, the IAE of the system frequency deviation is defined as

$$\text{IAE of } \Delta f_D = \int_0^{60} |\Delta f_D| dt \tag{17}$$

Fig.15 shows the values of IAE when the fluid coupling coefficient K_{fc} is varied from -30 % to +30 % of the normal values. The values of IAE in case of SMES [16] largely increase as K_{fc} decreases. In contrast, the values of IAE in case of the proposed SMES are lower and slightly change. Next, when all system parameters are changed from -30 % to +30 % of the normal values, the variation of IAE is depicted in Fig. 16. The values of IAE in case of SMES [16] highly increase when all system parameters decrease. This implies that SMES [16] is very sensitive to variation of system parameters. On the other hand, the proposed SMES is very robust to the variation of system parameters under this random wind power input. Fig.17 shows power output deviations of both SMESs under a 30 % decrease in all system parameters. Clearly, the peak power output of the proposed SMES is much lower than that of SMES [16].

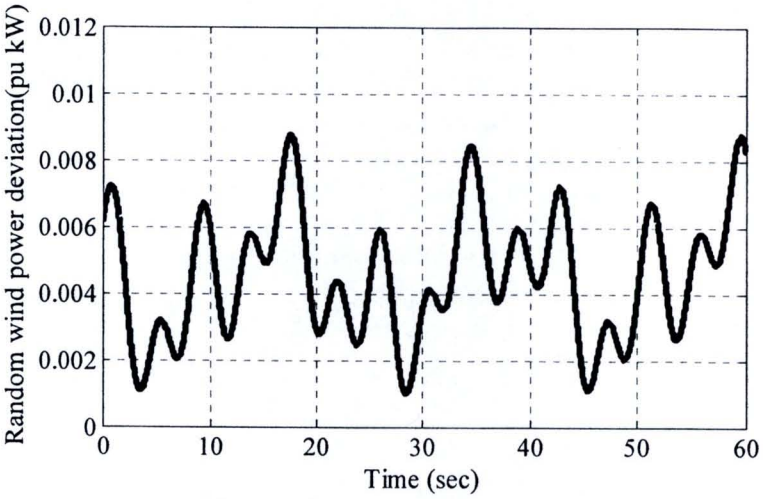

Fig. 13. Random wind power input.

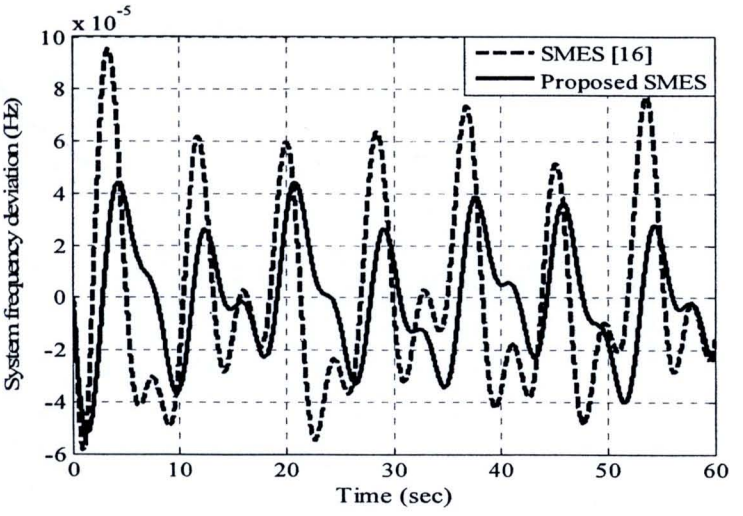

Fig. 14. System frequency deviation under normal system parameters.

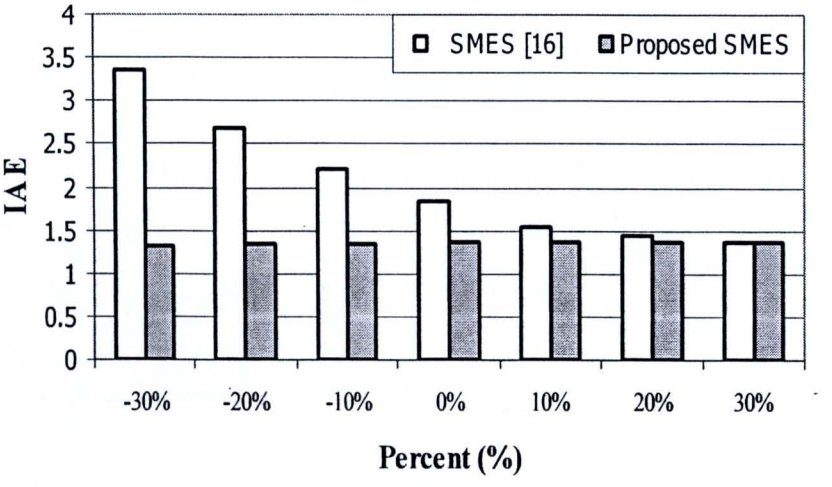

Fig. 15. Variation of IAE under a change of K_{fc}.

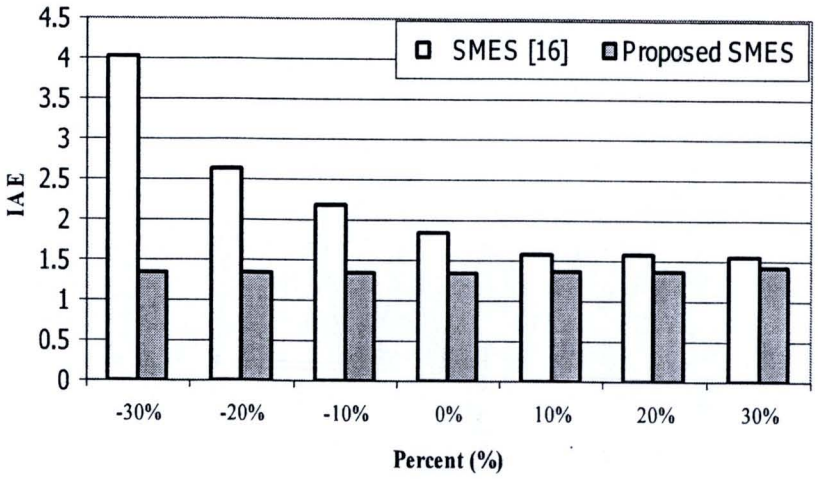

Fig. 16. Variation of IAE under a change of all system parameters.

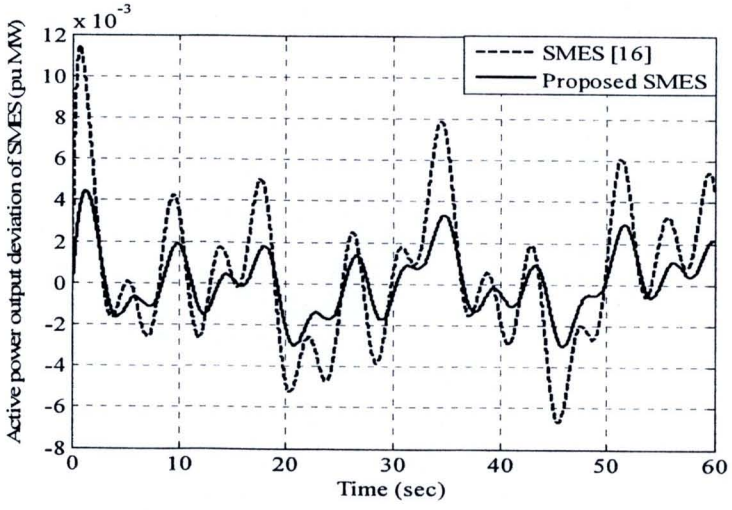

Fig. 17. Power output deviation of SMES under a 30 % decrease in all system parameters

Case 3: Random load change.

The random load change as shown in Fig.18 is applied to the system. Fig. 19 depicts the system frequency deviation under normal system parameters. Clearly,

the control effect of the proposed SMES is better than that of the SMES [16]. The values of IAE of system frequency deviation under the variation of K_{fc} from -30 % to +30 % of the normal values are shown in Fig.20. As K_{fc} decreases, the values of IAE in case of SMES [16] become larger. On the other hand, the values of IAE in case of the proposed SMES are lower and rarely change. The same trend of IAE variation is also obtained in Fig. 21 when all system parameters are varied from -30 % to +30 % of the normal values. The proposed SMES is more robust than the SMES [16] against the variation of system parameters under this random load change. As shown in Fig.22, power output deviations of both SMESs under a 30 % decrease in all system parameters are in the limit.

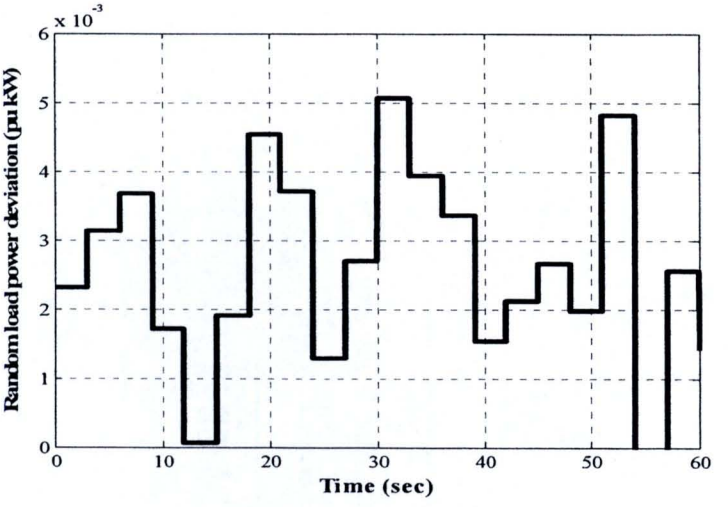

Fig. 18. Random load change.

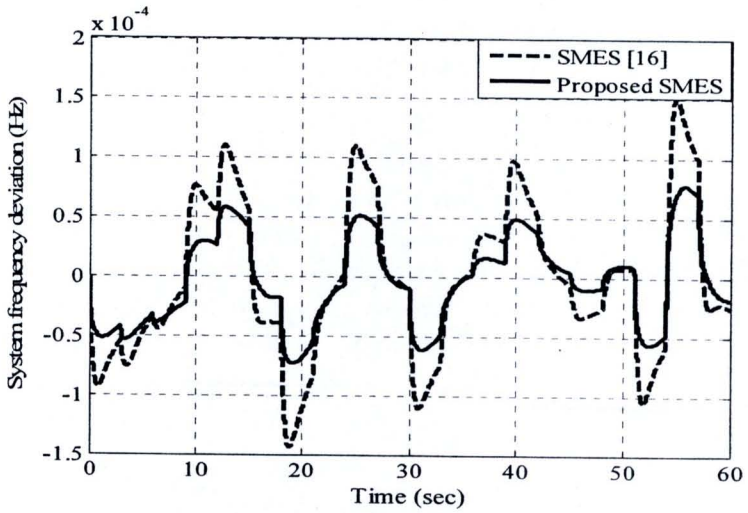

Fig. 19. System frequency deviation under normal system parameters.

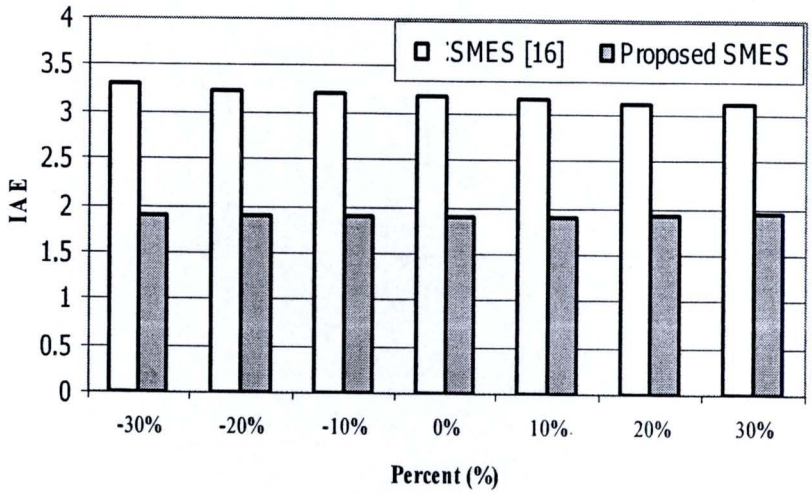

Fig. 20. Variation of IAE under a change of K_{fc}.

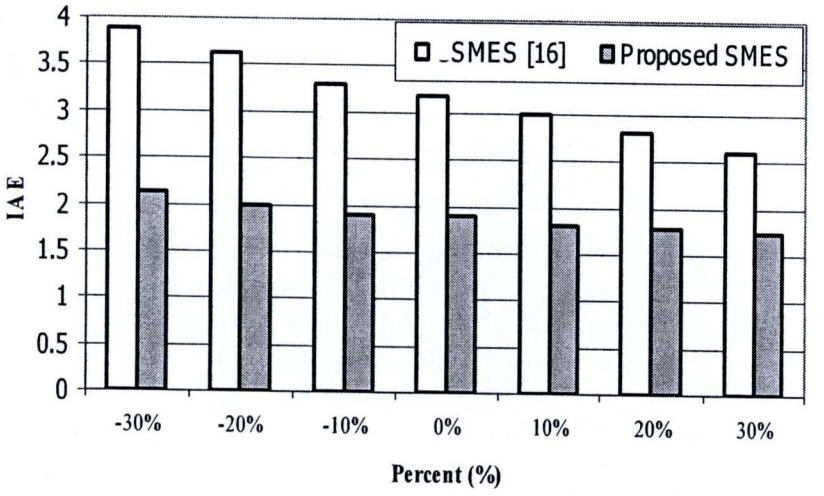

Fig. 21. Variation of IAE under a change of all system parameters.

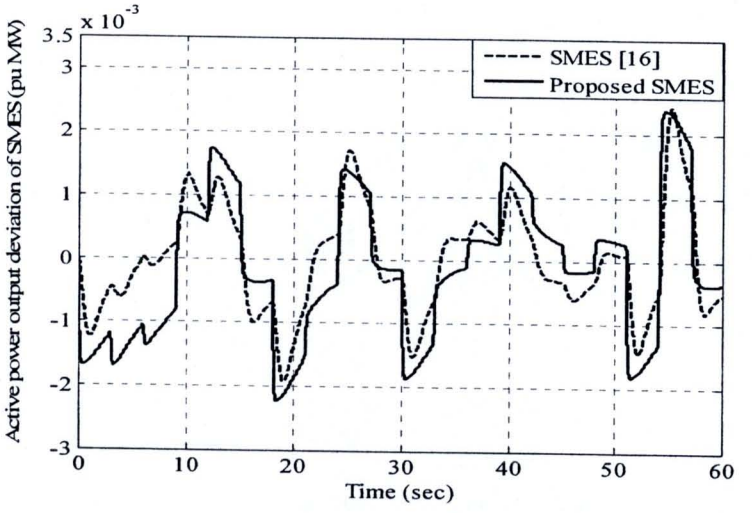

Fig. 22. Power output deviation of SMES under a 30 % decrease in all system parameters

Case 4: Simultaneous random wind power and load change.

In this case, the random wind power input in Fig. 13 and the load change in Fig.18 are applied to the system simultaneously. The system frequency deviation under normal system parameters are shown in Fig. 23. The frequency control

effect of the proposed SMES is superior to that of SMES [16]. Furthermore, when K_{fc} is reduced by 30 % from the normal value, the control effect of SMES [16] is significantly deteriorated as depicted in Fig.24. On the other hand, the frequency deviation is significantly reduced by the proposed SMES. The values of IAE of system frequency under the variation of K_{fc} from -30 % to +30 % of the normal values are shown in Fig.25. As K_{fc} decreases, the values of IAE in case of SMES [16] highly increase. On the other hand, the values of IAE in case of the proposed SMES are much lower and almost constant. In addition, when all parameters are changed from -30 % to +30 % of the normal values, the same tendency of IAE variation is also achieved as in Fig.26. These results confirm that the superior robustness of the proposed SMES over the SMES [16] against the variation of system parameters under both random wind power input and load change. Fig.27 depicts the power output deviations of both SMESs. The power output deviation of the proposed SMES is lower than that of SMES [16].

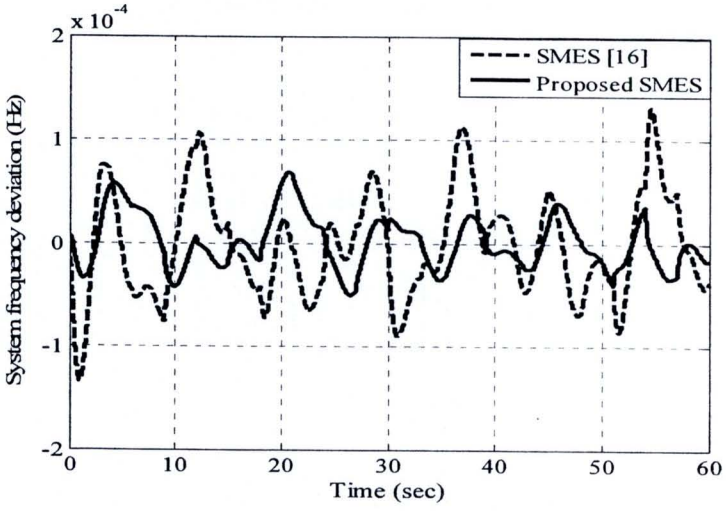

Fig. 23. System frequency deviation under normal parameters.

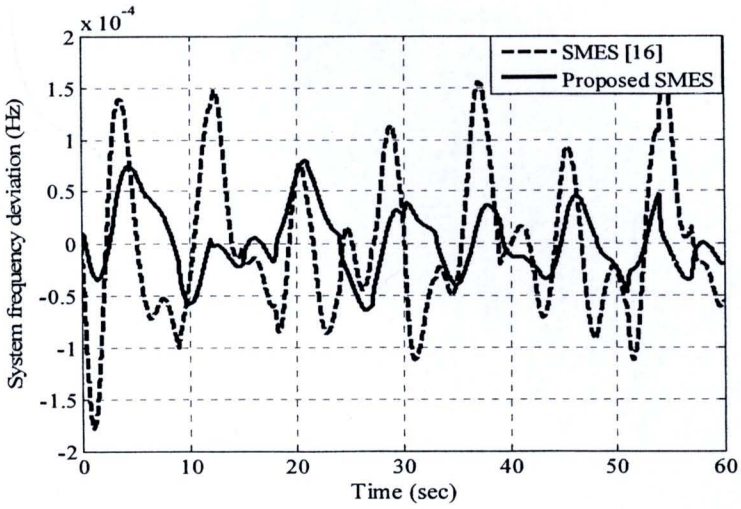

Fig. 24. System frequency deviation under a 30 % decrease in K_{fc}.

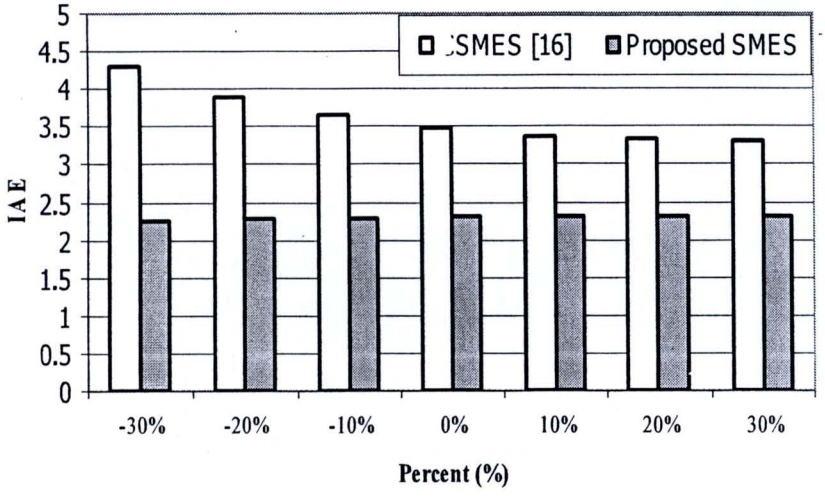

Fig. 25. Variation of IAE under a change in K_{fc}.

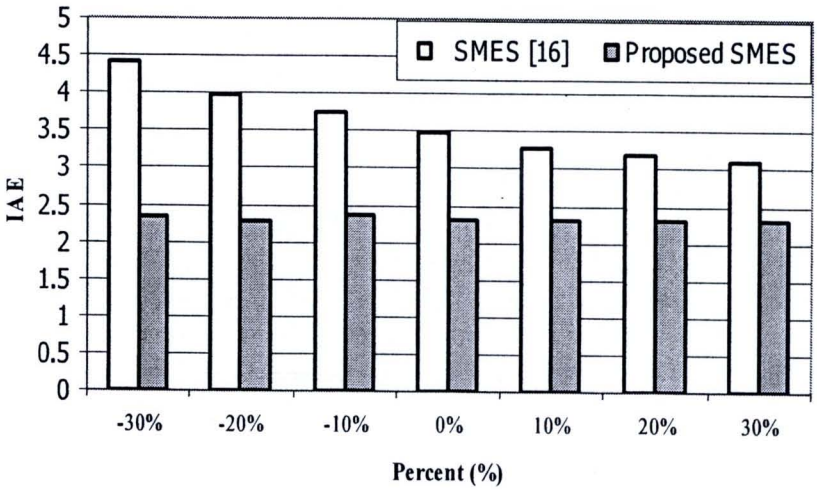

Fig. 26. Variation of IAE under a change in all system parameters.

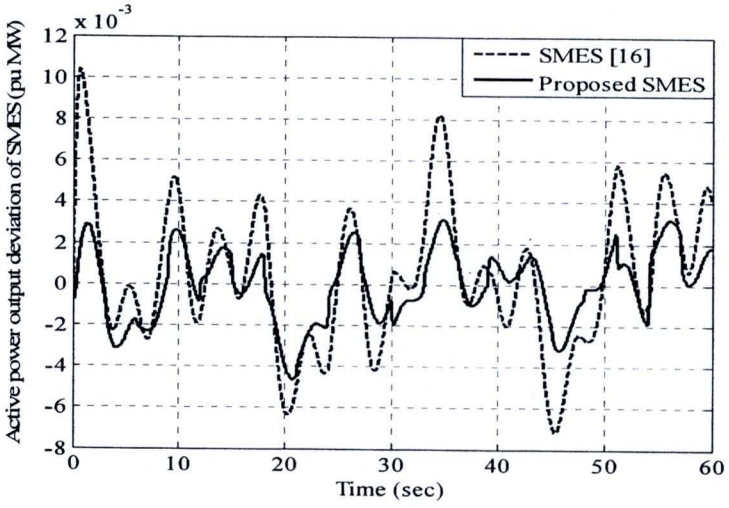

Fig. 27. Power output deviation of SMES under a 30 % decrease in all system parameters.

Finally, the kW and kJ capacities required for frequency control of the proposed SMES are evaluated based on random wind power input and load change in case study 4 in addition to a 30 % decrease in all system parameters. Note that there are various uncertainties in this case. The kW capacity is determined by the output limiter $-0.01 \leq \Delta P_{SMES} \leq 0.01$ pukW on a system base of

350 kW. As a result, the kW capacity of SMES is 3.5. For the kJ capacity, it is evaluated from the energy deviation of SMES (ΔE_{SMES}), where

$$\Delta E_{SMES} = \int \Delta P_{SMES} dt \tag{18}$$

$$\text{kJ Capacity of SMES} = \Delta E_{SMES\,(Max)} - \Delta E_{SMES\,(Min)} \tag{19}$$

Note that $\Delta E_{SMES\,(Max)}$ and $\Delta E_{SMES\,(Min)}$ are maximum and minimum values of energy deviation of SMES. Consequently, the kJ capacity of SMES is about 3.25. The small power capacity of SMES is required for the frequency control. This shows the economical merit of the proposed robust frequency control by SMES. In addition, the use of SMES allows an increase in the integration of wind energy in an island system.

6. Conclusions

The robust controller of SMES for frequency control in the hybrid wind-diesel power system has been presented. In the proposed controller design, unstructured uncertainties in the system such as variation of system parameters, power variations due to wind and load changes etc., are modeled by coprime factorization. The structure of frequency controller is practically based on the first-order lead/lag compensator with a single input signal. Consequently, it is easy to implement in practical systems. To obtain the controller parameters, the optimization problem based on H_∞ loop shaping technique can be automatically solved by GA. Simulation results clearly confirm that the proposed robust SMES is much superior to the SMES in [16] in terms of the robustness against uncertainties, random wind input and load change. Besides, the small power capacity of SMES is required for robust frequency control. The use of SMES allows an increase in the integration of wind energy in an island system

Appendix

System data

$P_R = 350\,\text{kW}$, $H_W = 3.5$ s, $H_D = 8.5$ s, $K_{fc} = 16.2$ Hz/pukW, $K_D = 16.5$ Hz/pukW, $K_{p2} = 1.25$, $K_{p3} = 1.4$, $T_{p1} = 0.6$ s, $T_{p2} = 0.041$ s, $K_{pc} = 0.08$, $K_{PI} = 4.0$, $K_{PP} = 1.5$.

Nomenclatures

P_R	area capacity
H_W	inertia constant on machine base for wind system
H_D	inertia constant on machine base for diesel system
K_{fc}	fluid coupling between wind and diesel sides
K_d	governor gain
K_{PI}	integral controller gain of pitch controller
K_{PP}	proportional controller gain of pitch controller
K_{p2}	gain of hydraulic pitch actuator
K_{p3}	gain of data fit pitch response
T_{p1}	time constant of hydraulic pitch actuator
T_{p2}	time constant of hydraulic pitch actuator
K_{pc}	blade characteristic
ΔP_{Load}	load change
ΔP_D	power output deviation of diesel side
ΔP_{Wind}	change in wind power
ΔP_W	power output deviation of wind side
Δf_W	frequency deviation of wind generation side
Δf_D	frequency deviation of diesel generation side (system frequenc deviation)
ΔP_{SMES}	power output deviation of SMES
ΔX	state vector
Δu_{SMES}	control signal deviation of SMES controller
A	system matrix
B	input matrix
K_{sm}	gain of frequency controller
T_{sm1}	time constant of frequency controller
T_{sm2}	time constant of frequency controller
T_{sm}	time constant of SMES

References

[1] Ackermann, T., *Wind power in power systems*, John Wiley & Sons Ltd, 2005.

[2] Patel, M.R., *Wind and solar power systems, design, analysis and operation*, 2nd Edition, CRC Press, 2006.

[3] Hunter, R., and Elliot, G., *Wind-diesel systems, a guide to technology and its Implementation*, Cambridge University Press, 1994.

[4] Lipman, N.H., *Wind-diesel and autonomous energy systems*, Elservier Science Publishers Ltd, 1989.

[5] Elgerd, O.L., *Electric energy systems theory, an introduction*, Mc Graw Hill, 1982.

[6] Jaleeli N. et al, "*Understanding automatic generation control*," *IEEE Transactions on Power Systems,* vol. 7, no. X, pp.106-112, 1999.

[7] Davies, T.S., Jefferson, C.M., and Mayer, R.M., "Use of flywheel storage for wind-diesel system," *Journal of Wind Engineering and Industrial Aerodynamics*, vol.27, pp. 157-165, 1988.

[8] Kunisch, H.J., Kramer, K.G., and Demonik, H., "Battery energy storage: another option for load-frequency control and instantaneous reserve," *IEEE Transactions on Energy Conversions*, vol. 1, no. 3, pp. 41-46, 1986.

[9] Boom, R.W., and Perterson, H., "A superconducting energy storage for power systems," *IEEE Transactions on Magnetic*, vol.8, pp. 701-703, 1972.

[10] Takahashi, R, and Tamura, J., "Frequency stabilization of small power system with wind farm by using flywheel energy storage system," *Proc. of IEEE International Symposium of Diagnostics for Electric Machines, Power electronics and Drives 2007,* pp.393-398.

[11] Aditya, S.K., and Das, D., "Application of battery energy storage system to load frequency control of an isolated power system," *International Journal of Energy Research*, vol. 23, no. 3, pp. 247-258, 1999.

[12] Lazarewicz, M.L., and Rojas, A., "Grid frequency regulation by recycling electrical energy in flywheels," *Proc. IEEE Power Engineering Society General Meeting 2004*, vol.2, pp. 2038-2042.

[13] Aditya, S. K., and Das, D., "Battery energy storage for load frequency control of an interconnected power system." *Electric Power Systems Research*, vol. 58, no. 3, pp. 133-213, 2001.

[14] Banerjee, S, Chatterjee, J.K., and Tripathy, S.C., "Application of magnetic energy storage unit as load frequency stabilizer," *IEEE Transactions on Energy Conversions*, vol.5, no. 1, pp. 46-51, 1990.

[15] Tripathy, S.C., Balasubramanian, R, and Chandramohanan, Nair P.S., "Effect of superconducting magnetic energy storage on automatic generation control considering governor deadband and boiler dynamics," *IEEE Transactions on Power Systems*, vol. 7, no. 3, pp.1266-1273, 1992.

[16] Tripathy, S.C., "Dynamic simulation of hybrid wind-diesel power generation system with superconducting magnetic energy storage," *Energy Conversion and Management*, vol.38, no.9, pp.919-930, 1997.

[17] Tripathy, S.C., Kalantar, M, Balasubramanian, R., "Dynamic and stability of wind and diesel turbine generators with superconducting magnetic energy storage unit on an isolated power system," *IEEE Transactions on Energy Conversions*, vol. 6, no. 4, pp. 579-585, 1991.

[18] Macfarlane, D.C., and Glover, K., "Robust controller design using normalized coprime factor plant descriptions," *Lecture notes in control and information sciences,* vol. 138, Springer, 1990.

[19] Skogestad, S, and Postlethwaite, *Multivariable feedback control: analysis and design*. 2nd edition, John Wiely, 2005.

[20] Haupt, R.L., and Hault, S.E., *Practical genetic algorithm*, 2nd edition, Wiley-interscience, 2004.

[21] Ngamroo, I., Cuk Supriyadi, A. N., Dechanupaprittha, S., and Mitani, Y., "Power oscillation suppression by robust SMES in power system with large wind power penetration," *Physica C: Superconductivity and Its Applications,* vol. 469, no. 1, pp. 44-51, 2009.

Physica C 469 (2009) 44–51

Contents lists available at ScienceDirect

Physica C

journal homepage: www.elsevier.com/locate/physc

Power oscillation suppression by robust SMES in power system with large wind power penetration

Issarachai Ngamroo [a,*], A.N. Cuk Supriyadi [a], Sanchai Dechanupaprittha [b], Yasunori Mitani [b]

[a] Electrical Engineering Department, Faculty of Engineering, King Mongkut's Institute of Technology Ladkrabang, Bangkok 10520, Thailand
[b] Graduate School of Engineering, Kyushu Institute of Technology, Fukuoka 804-8550, Japan

ARTICLE INFO

Article history:
Received 15 August 2008
Received in revised form 26 October 2008
Accepted 5 November 2008
Available online 24 November 2008

PACS:
84.70.+p
84.71.−b

Keywords:
Superconducting magnetic energy storage
Power system control
Robust control
Inverse additive perturbation
Wind farm

ABSTRACT

The large penetration of wind farm into interconnected power systems may cause the severe problem of tie-line power oscillations. To suppress power oscillations, the superconducting magnetic energy storage (SMES) which is able to control active and reactive powers simultaneously, can be applied. On the other hand, several generating and loading conditions, variation of system parameters, etc., cause uncertainties in the system. The SMES controller designed without considering system uncertainties may fail to suppress power oscillations. To enhance the robustness of SMES controller against system uncertainties, this paper proposes a robust control design of SMES by taking system uncertainties into account. The inverse additive perturbation is applied to represent the unstructured system uncertainties and included in power system modeling. The configuration of active and reactive power controllers is the first-order lead–lag compensator with single input feedback. To tune the controller parameters, the optimization problem is formulated based on the enhancement of robust stability margin. The particle swarm optimization is used to solve the problem and achieve the controller parameters. Simulation studies in the six-area interconnected power system with wind farms confirm the robustness of the proposed SMES under various operating conditions.

1. Introduction

At present, the penetration of wind power generations into power systems highly increases because of low impact to environment and infinite availability. Nevertheless, the wind power is unpredictable and intermittent in nature. The fluctuation of wind power generation may lead to a severe problem of tie-line power oscillations [1–4]. Additionally, the power oscillations due to wind power may violate the transmission capability margin and deteriorate the system stability [5,6].

To overcome this problem, a superconducting magnetic energy storage (SMES), which is able to supply and absorb active and reactive power simultaneously [7,8], can be applied. In the past, SMES has been used to solve many problems in power systems such as an improvement of power system dynamics [9,10], a frequency control in interconnected power systems [11,12], an enhancement of power quality [13], a stabilization of sub-synchronous oscillation in the turbine-generator [14], a load leveling [15], etc. On the other hand, various generating and loading conditions, wind power fluctuations, variation of system parameters and system nonlinearities, etc., result in unstructured system uncertainties. The SMES controller designed without taking system uncertainties into account may fail to operate and stabilize the power system.

To improve the robustness of the SMES controller against system uncertainties, this paper focuses on a robust controller design of SMES using the inverse additive perturbation [16]. Unstructured system uncertainties are represented by the inverse additive perturbation model and included in the system modeling. The structure of active and reactive power controllers is the first-order lead–lag compensator. Controller parameters are optimized by particle swarm optimization (PSO) [17] based on the improvement of the robust stability margin of the control system. Simulation studies are carried out in the six-area interconnected power system with large wind farms. Simulation results under various operating conditions such as heavy line flow, light line flow and wind power fluctuations, confirm that the robustness of the proposed SMES is superior to that of the SMES designed without considering robustness.

2. Study system and modeling

A six-area interconnected power system in Fig. 1 is used as the study system. The area capacity ratio for areas 1–6 is 20:13.5:6:75:40:6.75:33 with a 1000 MVA base. Each area is represented by a 5-state transient model [18]. It is equipped with a sim-

* Corresponding author.
E-mail address: ngamroo@gmail.com (I. Ngamroo).

0921-4534/$ - see front matter © 2008 Elsevier B.V. All rights reserved.
doi:10.1016/j.physc.2008.11.002

Nomenclature

$K_P(s)$	SMES active power controller
$K_Q(s)$	SMES reactive power controller
$K_{Ism}(s)$	SMES coil current controller
$K_V(s)$	SMES voltage controller
K_1	gain of active power controller
K_2	gain of reactive power controller
T_{11}, T_{12}	time constants of the active power controller (s)
T_{21}, T_{22}	time constants of the reactive power controller (s)
ΔP_{tie}	active power deviation (p.u.)
ΔQ_{tie}	reactive power deviation (p.u.)
K_P	proportional gain of PI controller
T_I	time constant of PI controller (s)
K_{sm}	gain of SMES coil controller
I_{sm}	SMES coil current (p.u.)
I_{sm0}	initial value of SMES coil current (p.u.)
E_{out}	SMES energy output (J)
L_{sm}	SMES coil inductance (H)
$I_{sm,base}$	SMES current base (A)
P_{sm}	SMES active power output (p.u.)
Q_{sm}	SMES reactive power output (p.u.)
$S_{sm,base}$	SMES MVA base
V_{tbase}	system base voltage
E_{sm}	energy stored in a SMES unit (J)
E_{sm0}	initial energy stored in a SMES unit (J)
K_{Vsm}	gain of SMES voltage controller
V_{t0}	initial value of a terminal bus voltage of a SMES unit (p.u.)
V_{ts}	bus voltage of SMES (p.u.)
P_d	desired active power output of SMES (p.u.)
Q_d	desired reactive power output of SMES (p.u.)
AP	active power fraction
AQ	reactive power fraction
$CONV$	converter
T_c	time constant of converter (s)
K_i	gain of SMES controller
T_{ij}	time constant of SMES controller (s)
$\|\cdot\|_\infty$	infinite norm of transfer function
ζ	actual damping ratio of the dominant inter-area oscillation mode
ζ_{spec}	desired damping ratio of the dominant inter-area oscillation mode
σ	actual real part of the eigenvalue
σ_{spec}	desired real part of the eigenvalue
$K_{i,\max}$	maximum gain of power controller
$K_{i,\min}$	minimum gain of power controller
$T_{ij,\max}$	maximum time constant
$T_{ij,\min}$	minimum time constant

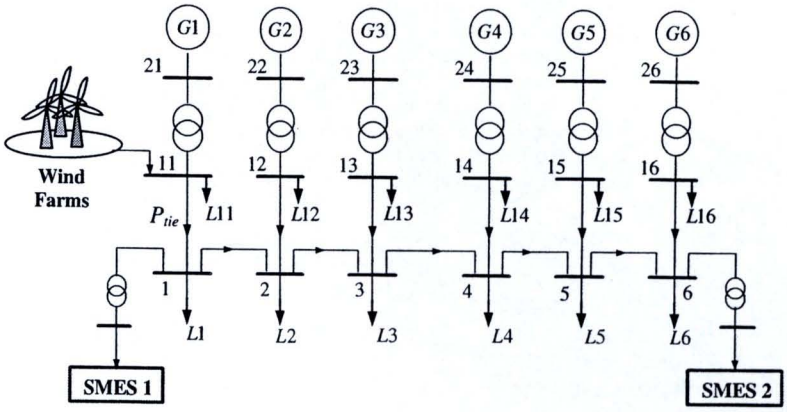

Fig. 1. Six-area interconnected power system with wind farms.

plified exciter and governor [18]. For the study purpose, the electric power is transferred from areas 1–6. The wind farm is located at bus 11 in area 1 with maximum generating capacity 450 MW. In this study, the wind farm is modeled by the random power source. Based on the residue method [19], the suitable locations of two SMESs are selected at bus 1 and bus 6. Each SMES has a specification of 800 MJ, 40 kA, 1000 MVA [19].

Fig. 2 shows the SMES model with simultaneous active and reactive power (P–Q) modulation control scheme [20]. In the model, K_P and $K_Q(s)$ are represented by

$$K_P(s) = K_1 \frac{(1 + T_{11}s)}{(1 + T_{12}s)} \tag{1}$$

$$K_Q(s) = K_2 \frac{(1 + T_{21}s)}{(1 + T_{22}s)} \tag{2}$$

The input signals of active and reactive power controllers of SMES1 and SMES2 are ΔP_{tie} and ΔQ_{tie} in a tie-line from bus 11 to bus 1 and from bus 16 to bus 6, respectively. In this paper, gains and time constants of both controllers are optimized by the proposed method.

As shown in Fig. 2, $K_{Ism}(s)$ can be represented by

$$K_{Ism}(s) = \left(K_P + \frac{1}{T_I s}\right) K_{sm}(I_{sm} - I_{sm0}) \tag{3}$$

In the SMES model, the effect of I_{sm} is considered, since the dynamic behavior of I_{sm} significantly affects the overall performance of SMES. In practice, I_{sm} is not allowed to reach zero to prevent the possibility of discontinuous conduction under unexpected disturbances. On the other hand, high I_{sm} which is above the maximum allowable limit, may lead to loss of superconducting properties. Based on the hardware operational constraints, the lower and upper coil current limits are considered and assigned as $0.30I_{sm0}$ and $1.38I_{sm0}$, respectively. Here, I_{sm} can be calculated from the PEI block which has a relation as

$$I_{sm} = \sqrt{I_{sm0}^2 - \frac{2E_{out}}{L_{sm} I_{sm,base}^2}} \tag{4}$$

$$E_{out} = \int P_{sm} dt \cdot S_{sm,base} \tag{5}$$

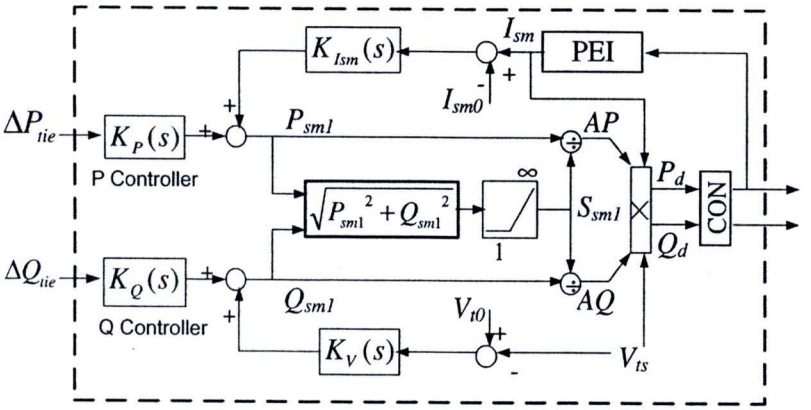

Fig. 2. SMES with active and reactive (P–Q) controllers.

Subsequently, the energy stored in a SMES unit and the initial energy stored can be determined by

$$E_{sm} = E_{sm0} - E_{out} \tag{6}$$

$$E_{sm0} = 0.5 L_{sm} I_{sm0}^2 \cdot I_{sm.base}^2 \tag{7}$$

Besides, $K_V(s)$ can be represented by

$$K_V(s) = K_{Vsm}(V_{t0} - V_{ts}) \tag{8}$$

The desired active and reactive power outputs of SMES can be expressed as

$$P_d = V_{ts} I_{sm} AP \tag{9}$$

$$Q_d = V_{ts} I_{sm} AQ \tag{10}$$

In Fig. 2, P_{sm} and Q_{sm} are the output of the SMES controlled converter (CONV). The converter transfer function can be represented by the first-order time-lag compensator as

$$CONV = 1/(1 + T_c s) \tag{11}$$

3. Proposed robust control design

To improve the robustness of active and reactive power controllers against system uncertainties, the inverse additive perturbation [16] is applied to formulate the optimization problem of controller parameters.

The feedback control system with inverse additive perturbation is depicted in Fig. 3. G is the nominal plant. K is the designed controller. System uncertainties such as various generating and loading conditions, variation of system parameters and nonlinearities, etc., are represented by Δ_A which is the unstructured additive uncertainty model. Based on the small gain theorem, for a stable additive uncertainty Δ_A, the system is stable if

$$|\Delta_A G/(1 - GK)| < 1 \tag{12}$$

Then,

$$|\Delta_A| < 1/|G/(1 - GK)| \tag{13}$$

The right hand side of (13) implies the size of system uncertainties or the robust stability margin against system uncertainties. By minimizing $|G/(1 - GK)|$, the robust stability margin of the closed-loop system is maximum. This concept can be applied as the optimization problem as

$$\begin{aligned} &\text{Minimize} \quad J = \|G/(1 - GK)\|_\infty \\ &\text{Subject to} \quad \zeta \geqslant \zeta_{spec}, \quad \sigma \geqslant \sigma_{spec}, \quad K_{i,\min} \leqslant K_i \leqslant K_{i,\max} \\ &T_{ij,\min} \leqslant T_{ij} \leqslant T_{ij,\max}, \quad i = 1,2, \quad j = 1,2 \end{aligned} \tag{14}$$

ζ_{spec} and σ_{spec} are desired damping ratio and desired real part of the eigenvalue corresponding to the dominant inter-area oscillation mode, respectively. The objective of the optimization is not only to improve the robustness of the SMES but also to move the dominant inter-area oscillation modes to the D-stability region as shown in Fig. 4. This optimization problem is solved by PSO [17].

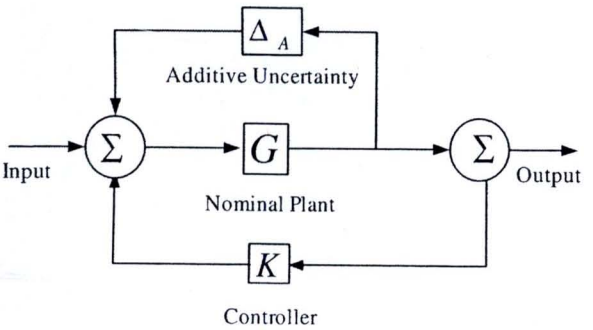

Fig. 3. Feedback system with inverse additive perturbation.

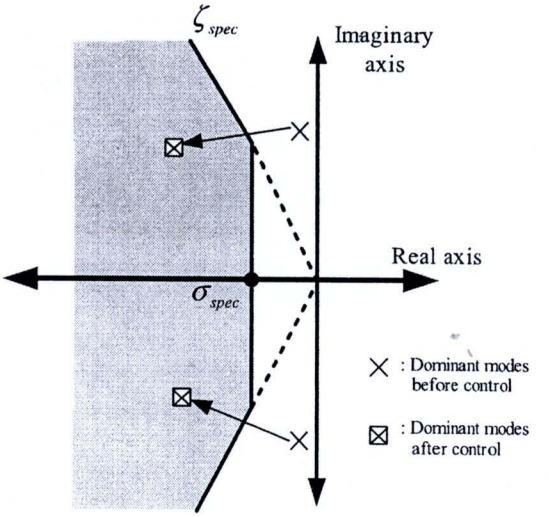

Fig. 4. D-stability region.

Table 1
SMES parameters.

Capacity: 800 MJ, 40 kA, 1000 MVA	
K_p: 40.0	I_{smo}: 0.675 p.u.
T_I: 0.40	L_{sm}: 10.0 H
K_{sm}: 1.00	$S_{sm,base}$: 1000 MVA
K_{Vsm}: 1.00	V_{tbase}: 25 kV
T_c: 0.01	V_{to}: 0.95 p.u.

4. Simulation studies

The parameters of SMES model in Fig. 2 are given in Table 1. For control parameters optimization of SMES by PSO, the design specification and ranges of search parameters are set as follows: $\zeta_{spec} = 0.04$, $\sigma_{spec} = -0.2$, $K_i \in [1 \quad 10]$, $T_{ij} \in [0.0001 \quad 1]$, number of particles = 24, maximum iterations = 100, acceleration factors = 2, and the inertia weights $\omega_{max} = 0.9$ and $\omega_{min} = 0.4$. First, the linearized power system is formulated based on the normal operating condition (Case 2) in Table 2. By optimizing control parameters in the linearized system using PSO, the active and reactive power controllers of the robust SMES which is referred to as "RSMES", are obtained as

RSMES1:

$$K_{P1}(s) = 5.788\frac{(0.7924s+1)}{(0.1845s+1)} \tag{15}$$

$$K_{Q1}(s) = 4.492\frac{(0.7828s+1)}{(0.2346s+1)} \tag{16}$$

RSMES2:

$$K_{P2}(s) = 3.452\frac{(0.8429s+1)}{(0.1775s+1)} \tag{17}$$

$$K_{Q2}(s) = 7.229\frac{(0.7589s+1)}{(0.2564s+1)} \tag{18}$$

The robustness of RSMES is compared with the SMES designed without considering the robustness which is referred as "CSMES". CSMES is designed to yield the damping ratio and the real part of the dominant inter-area mode same as the design specification of RSMES. Based on [21], the optimization problem of CSMES is formulated as

$$\begin{aligned} &\text{Minimize} \quad J = \sum_{\zeta \leqslant \zeta_{spec}} |\zeta_{spec} - \zeta| + \sum_{\sigma \geqslant \sigma_{spec}} |\sigma_{spec} - \sigma| \\ &\text{Subject to} \quad K_{i,\min} \leqslant K_i \leqslant K_{i,\max} \\ &T_{ij,\min} \leqslant T_{ij} \leqslant T_{ij,\max}, \quad i = 1,2, \quad j = 1,2 \end{aligned} \tag{19}$$

Note that the objective of the optimization (19) is to move the dominant inter-area oscillation modes to the D-stability region as shown in Fig. 4. Solving (19) by PSO, the active and reactive power controllers of CSMES are obtained as

CSMES1:

$$K_{P1}(s) = 5.724\frac{(0.2898s+1)}{(0.1908s+1)} \tag{20}$$

$$K_{Q1}(s) = 5.724\frac{(0.9689s+1)}{(0.7901s+1)} \tag{21}$$

CSMES2:

$$K_{P2}(s) = 4.823\frac{(0.8974s+1)}{(0.5883s+1)} \tag{22}$$

$$K_{Q2}(s) = 7.353\frac{(0.7342s+1)}{(0.4901s+1)} \tag{23}$$

Table 3 shows the eigenvalues and damping ratios of two dominant inter-area oscillation modes for three case studies. Without SMES, the damping ratios of two oscillation modes are very poor in cases 1 and 2 and become unstable in case 3 with heavy tie-line flow. On the other hand, the damping ratio and the real part of two oscillation modes are achieved by both CSMES and RSMES in all cases.

Table 2
Case studies (MVA base = 1000 MVA).

Generation	1. LL (P_{tie} = 1.5) (p.u.)	2. NOC (P_{tie} = 2.3) (p.u.)	3. HL (P_{tie} = 3.0) (p.u.)
G1	P_G = 8, $L1$ = 1.5, $L11$ = 5 + 0.5i	P_G = 12, $L1$ = 2.2, $L11$=7 + 0.7i	P_G = 16, $L1$ = 3.0, $L11$ = 10 + 1.0i
G2	P_G: 5.4, $L2$ = 1.0, $L12$ = 4.2 + 0.4i	P_G = 8.1, $L2$ = 1.5, $L12$ = 6.3 + 0.6i	P_G = 10.8, $L2$ = 2.0 $L12$ = 8.4 + 0.8i
G3	P_G = 2.7, $L3$ = 0.6, $L13$ = 2.1 + 0.2i	P_G = 4.05, $L3$ = 0.9, $L13$ = 3.2 + 0.3i	P_G = 5.4, $L3$ = 1.2 $L13$ = 4.2 + 0.4i
G4	P_G = 16, $L4$ = 3.0, $L14$ = 13 + 1.3i	P_G = 24, $L4$ = 4.5, $L14$ = 18.5 + 1.8i	P_G = 32, $L4$ = 6 $L14$ = 26 + 2.6i
G5	P_G = 2.7, $L5$ = 0.6, $L15$ = 2.1 + 0.2i	P_G = 4.05, $L5$ = 0.9, $L15$ = 3.2 + 0.3i	P_G = 5.4, $L5$ = 1.2, $L15$ = 4.2 + 0.4i
G6	P_G = 11.55, $L6$ = 3.0, $L16$ = 10.2 + 1.0i	P_G = 16.4, $L6$ = 4.5, $L16$ = 15.3 + 1.5i	P_G = 23.2, $L6$ = 6.0, $L16$ = 20.6 + 2.0i

NOC: normal operating condition, LL: light load, HL: heavy load, P_G: generation (p.u.), Li: load at bus i (p.u.), base: 1000 MVA.

Table 3
Eigenvalues of dominant inter-area oscillation modes.

Case	No SMES	CSMES	RSMES
Case 1 (LL)	−0.155 ± 3.90i ζ = 0.0396	−0.402 ± 6.31i ζ = 0.0635	−0.381 ± 6.30i ζ = 0.0602
	−0.117 ± 2.93i ζ = 0.0400	−0.255 ± 3.96 ζ = 0.0644	−0.348 ± 3.89i ζ = 0.0892
Case 2 (NOC)	−0.104 ± 3.679i ζ = 0.028	−0.321 ± 6.65i ζ = 0.0481	−0.279 ± 6.63i ζ = 0.042
	−0.074 ± 2.713i ζ = 0.027	−0.218 ± 3.85i ζ = 0.0567	−0.369 ± 3.78i ζ = 0.097
Case 3 (HL)	−0.0361 ± 3.413i ζ = 0.011	−0.290 ± 6.81i ζ = 0.0425	−0.233 ± 6.76i ζ = 0.0345
	0.1001 ± 2.387i ζ = −0.040	−0.235 ± 3.76i ζ = 0.0624	−0.456 ± 3.81i ζ = 0.119

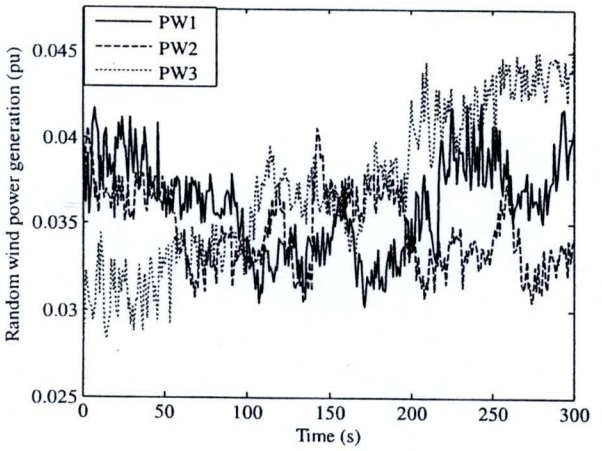

Fig. 5. Wind power generations.

Next, nonlinear simulations of three case studies in Table 2 are carried out under three patterns of wind power generations [PW1], [PW2] and [PW3] as depicted in Fig. 5. Each pattern of wind power is injected to bus 11. To show the frequency components of wind patterns, Fast Fourier Transform (FFT) is applied. As a result, the frequency components of each wind pattern can be shown in Fig. 6. It can be observed that the frequency components of all wind patterns are dominantly in the low frequency range which is in the same range of inter-area power oscillation (0.2–0.8 Hz). As a result, the power fluctuation from wind farms may activate the inter-area oscillation modes with weak damping and cause severe oscillation.

Figs. 7–9 show the comparison of the maximum tie-line power deviation (P_{tie}) in case of PW1, PW2 and PW3, respectively. Without SMES, the maximum power deviation is very large especially in case 3. In contrast, the maximum power deviation is effectively suppressed by either CSMES or RSMES. However, CSMES is quite sensitive to operating conditions in cases 2 and 3. The maximum power deviation highly increases in cases 2 and 3. On the other hand, RSMES is very robust to any operating condition and wind pattern. The maximum power deviation rarely changes. Fig. 10 shows tie-line power deviation of case 3 with wind PW1. Without SMES, since one dominant mode is unstable as shown in Table 3, the tie-line power gradually increases and eventually diverges (not shown here). On the contrary, the power fluctuation is significantly alleviated by SMES. Nevertheless, RSMES provides more damping effects than CSMES. These results signify that the robust stabilizing effect of RSMES against wind power fluctuations is much superior to that of CSMES.

Next, the frequency components of tie-line power deviations are analyzed by FFT in case of wind power PW2. Fig. 11 shows the comparison FFT results of tie-line power deviation in case 3 with wind power PW2. In the left figure, the amplitude of dominant frequency in case of No SMES is much higher than those of CSMES and RSMES. This implies that the amplitude of tie-line power deviation is very high and severe. The right figure shows the enlarged amplitude of dominant frequency. Clearly, the RMES is able to reduce the amplitude significantly in comparison to the CSMES.

To evaluate the robustness of SMES, the peak amplitude of FFT result of tie-line power deviation under three operating conditions is considered. Figs. 12–14 show the comparison of the peak amplitude of FFT result of tie-line power deviation in cases PW1, PW2 and PW3, respectively. Without SMES, the peak frequency characteristic is very large especially in case 3. In contrast, the peak frequency characteristic is effectively suppressed by either CSMES

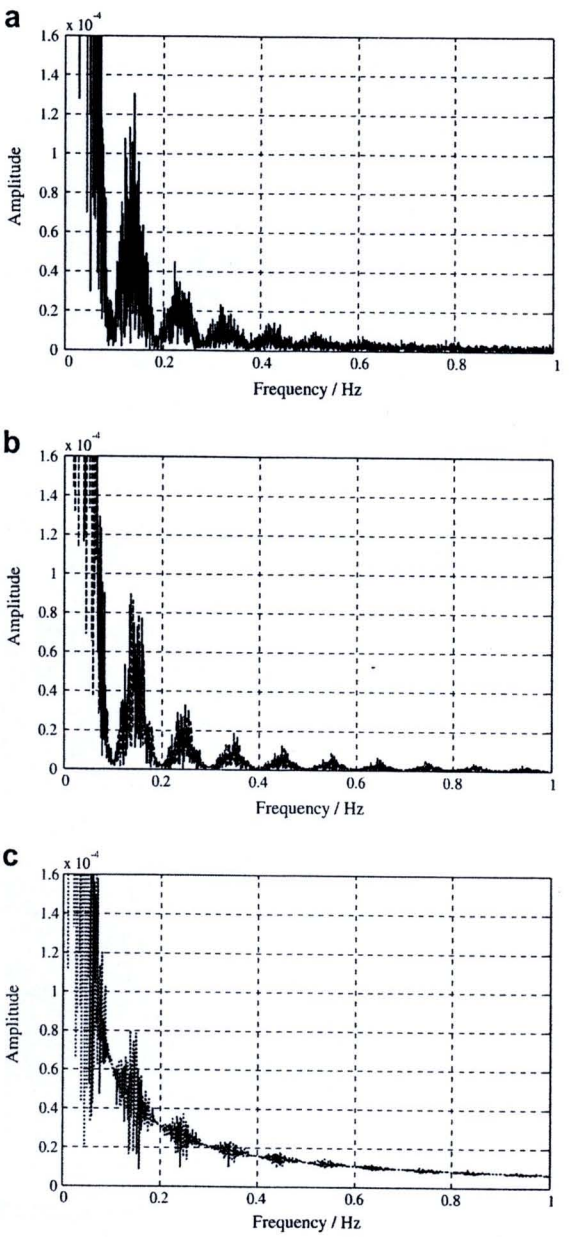

Fig. 6. Frequency component of wind patterns: (a) PW1; (b) PW2 and (c) PW3.

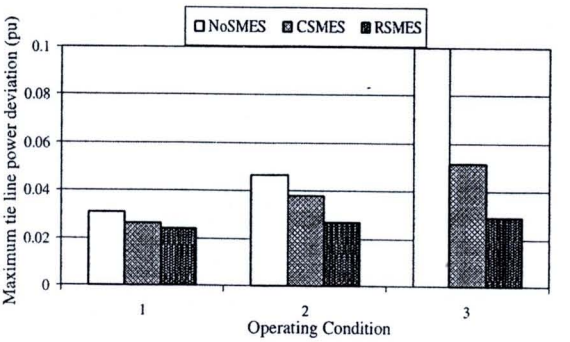

Fig. 7. Maximum tie-line power deviation in case of wind power PW1.

or RSMES. However, CSMES is quite sensitive to operating conditions in cases 2 and 3. The peak frequency characteristic highly in-

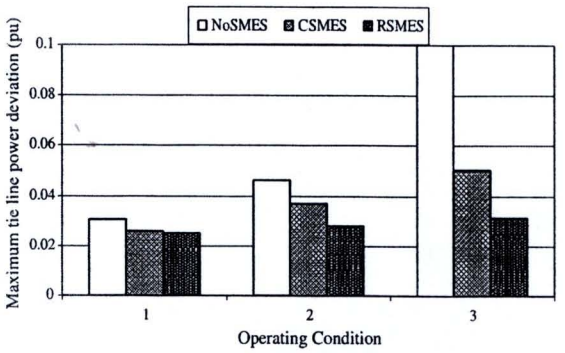

Fig. 8. Maximum tie-line power deviation in case of wind power PW2.

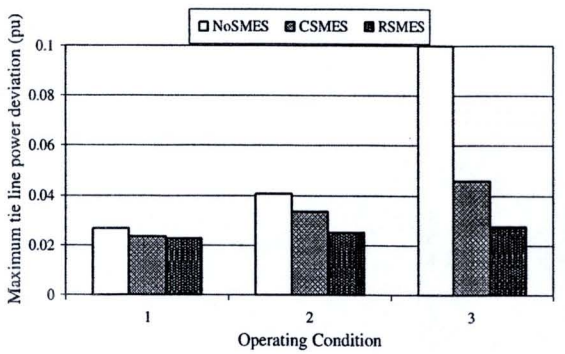

Fig. 9. Maximum tie-line power deviation in case of wind power PW3.

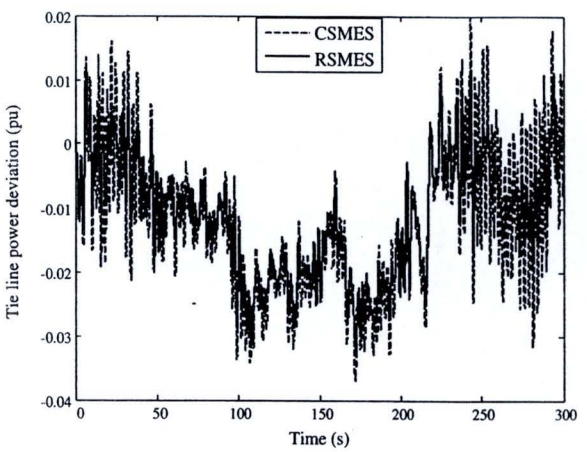

Fig. 10. Tie-line power deviation in case 3 with wind power PW1.

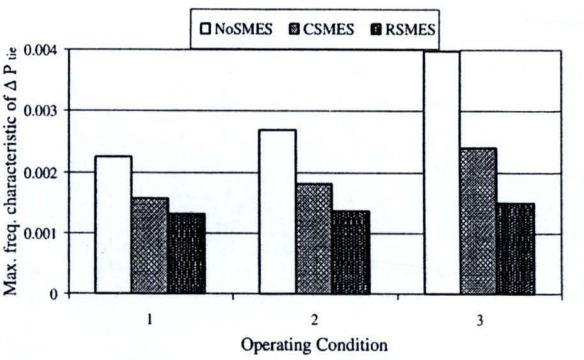

Fig. 12. Peak amplitude of FFT result of tie-line power deviation for PW1.

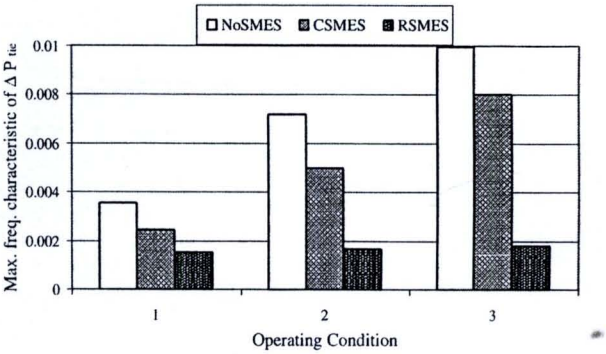

Fig. 13. Peak amplitude of FFT result of tie-line power deviation for PW2.

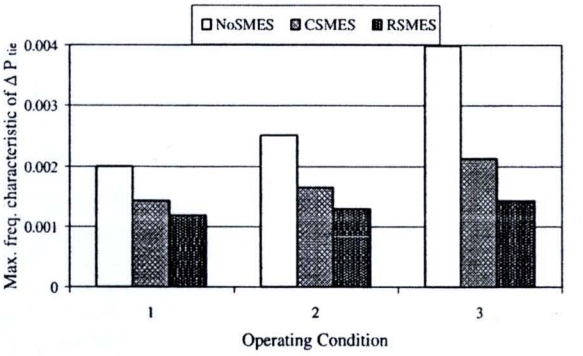

Fig. 14. Peak amplitude of FFT result of tie-line power deviation for PW3.

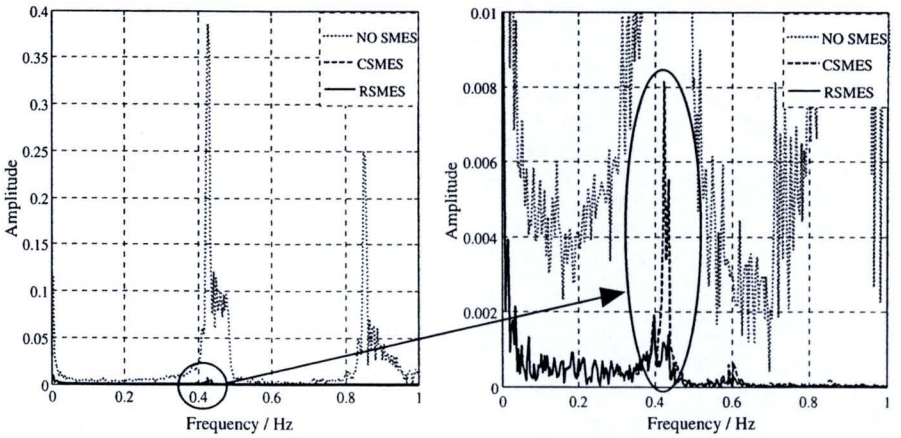

Fig. 11. FFT result of frequency components of tie-line power deviation with PW2.

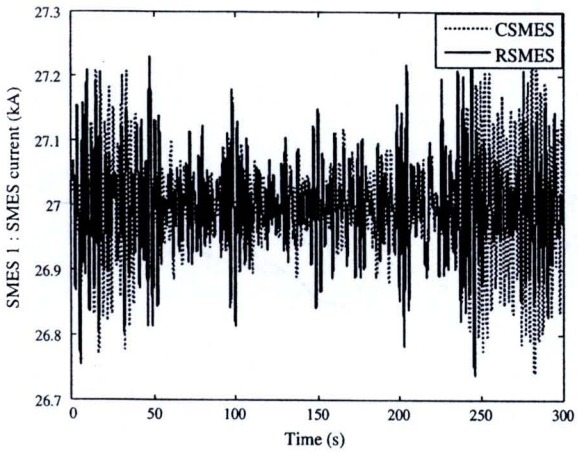

Fig. 15. SMES1 coil current in case 3 with wind power PW2.

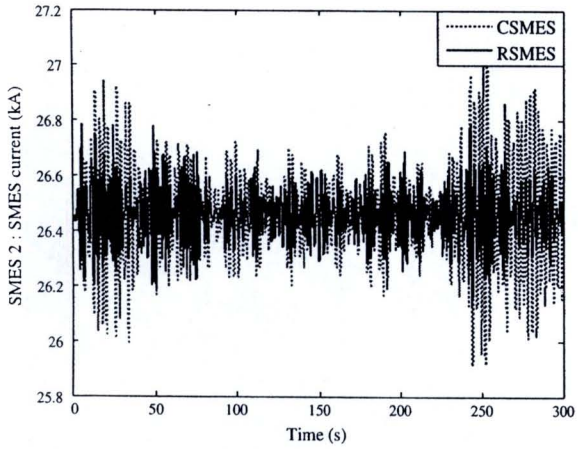

Fig. 16. SMES2 coil current in case 3 with wind power PW2.

creases in cases 2 and 3. On the other hand, RSMES is very robust to any operating condition and wind pattern. The peak frequency characteristic rarely changes.

The coil currents of SMES1 and SMES2 in case 3 with wind power PW2 are shown in Figs. 15 and 16, respectively. Both coil currents of CSMES and RSMES can properly remain within the allowable limits. For SMES1, the current fluctuation of RSMES is almost the same as that of CSMES. However, in case of SMES2, the current fluctuation of RSMES is much lower than that in case of CSMES. This indicates that RSMES can appropriately supply and receive electrical energy with power system. Accordingly, the stabilizing effect of tie-line power flow by RSMES is superior to that of CSMES.

To evaluate the robustness of both CSMES and RSMES, the eigenvalue analysis is carried out when P_{tie} is varied from 1.5 p.u. to 4.0 p.u. as shown in Table 4. Not only the design operating condition, CSMES is able to stabilize the dominant modes at a wide range of operating conditions. Nevertheless, at the very high power flow condition $P_{tie} \geqslant 3.84$ p.u., CSMES which is designed without considering robustness, loses stabilizing effect. It can not stabilize the oscillation mode anymore. One dominant mode becomes unstable. On the other hand, RSMES is very robust to this condition. It can robustly stabilize both dominant modes.

Finally, to investigate the eigenvalue result, nonlinear simulation with wind power PW1 when $P_{tie} = 3.84$ p.u. is performed and shown in Fig. 17. Clearly, simulation result is consistent with

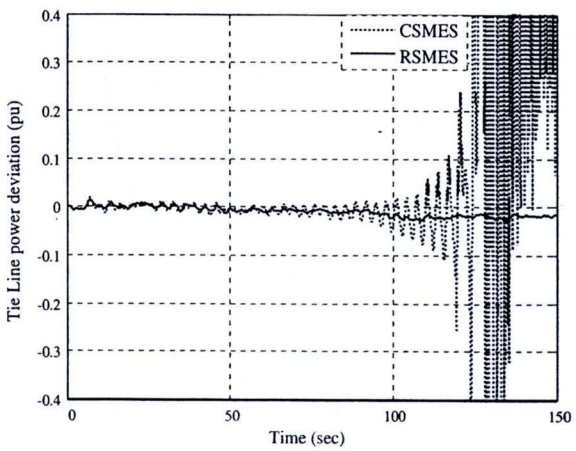

Fig. 17. Tie-line power deviation with wind power PW1 when $P_{tie} = 3.84$ p.u.

Table 4
Change in inter-area oscillation modes again variation of P_{tie}

P_{tie}	No SMES		CSMES		RSMES	
1.50	−0.1170 ± *j*2.9301*i*	−0.155 ± 3.9021*i*	−0.2550 ± 3.9621*i*	−0.4022 ± 6.3104*i*	−0.3482 ± 3.8932*i*	−0.3812 ± 6.3232*i*
1.63	−0.1292 + 2.7302*i*	−0.1437 + 3.8008*i*	−0.3667 + 3.0178*i*	−0.3345 + 5.6906*i*	−0.3978 + 3.3468*i*	−0.3556 + 6.4322*i*
1.76	−0.1274 + 2.7301*i*	−0.1443 + 3.8116*i*	−0.3699 + 3.0189*i*	−0.3310 + 5.7345*i*	−0.3947 + 3.3435*i*	−0.3419 + 6.4719*i*
1.89	−0.1257 + 2.7296*i*	−0.1487 + 3.8349*i*	−0.3715 + 3.0109*i*	−0.3271 + 5.7739*i*	−0.3894 + 3.3324*i*	−0.3277 + 6.5049*i*
2.02	−0.1202 + 2.7125*i*	−0.1479 + 3.8327*i*	−0.3711 + 2.9941*i*	−0.3228 + 5.8085*i*	−0.3836 + 3.3155*i*	−0.3142 + 6.5302*i*
2.15	−0.1110 + 2.6911*i*	−0.1465 + 3.8273*i*	−0.3686 + 2.9678*i*	−0.3180 + 5.8384*i*	−0.3769 + 3.2922*i*	−0.3017 + 6.5482*i*
2.28	−0.0996 + 2.6605*i*	−0.1450 + 3.8166*i*	−0.3636 + 2.9315*i*	−0.3127 + 5.8631*i*	−0.3688 + 3.2621*i*	−0.2902 + 6.5592*i*
2.41	−0.0849 + 2.6213*i*	−0.1425 + 3.7984*i*	−0.3555 + 2.8847*i*	−0.3069 + 5.8827*i*	−0.3587 + 3.2249*i*	−0.2795 + 6.5638*i*
2.54	−0.0673 + 2.5753*i*	−0.1396 + 3.7754*i*	−0.3435 + 2.8268*i*	−0.3005 + 5.8969*i*	−0.3460 + 3.1803*i*	−0.2696 + 6.5619*i*
2.67	−0.0465 + 2.5223*i*	−0.1359 + 3.7468*i*	−0.3263 + 2.7574*i*	−0.2934 + 5.9055*i*	−0.3303 + 3.1280*i*	−0.2598 + 6.5535*i*
2.80	−0.0227 + 2.4627*i*	−0.1312 + 3.7126*i*	−0.3029 + 2.6763*i*	−0.2856 + 5.9080*i*	−0.3109 + 3.0678*i*	−0.2493 + 6.5389*i*
2.93	**0.0288 + 2.3549*i***	−0.1281 + 3.6830*i*	−0.2719 + 2.5835*i*	−0.2770 + 5.9041*i*	−0.2873 + 2.9992*i*	−0.2402 + 6.5176*i*
3.06	**0.0621 + 2.2823*i***	−0.1206 + 3.6542*i*	−0.2410 + 2.4801*i*	−0.2676 + 5.8939*i*	−0.2681 + 2.9503*i*	−0.2296 + 6.4915*i*
3.19	**0.0832 + 2.1998*i***	−0.1107 + 3.5856*i*	−0.2155 + 2.4025*i*	−0.2571 + 5.8712*i*	−0.2492 + 2.9032*i*	−0.2197 + 6.4562*i*
3.32	**0.0990 + 2.1541*i***	−0.0978 + 3.5151*i*	−0.1649 + 2.2769*i*	−0.2458 + 5.8444*i*	−0.2254 + 2.8358*i*	−0.2132 + 6.4341*i*
3.45	**0.1358 + 2.0541*i***	−0.0829 + 3.4426*i*	−0.1217 + 2.1727*i*	−0.2389 + 5.8190*i*	−0.2010 + 2.7712*i*	−0.2056 + 6.4156*i*
3.58	**0.1693 + 1.9474*i***	−0.0663 + 3.3773*i*	−0.0708 + 2.0895*i*	−0.2302 + 5.7772*i*	−0.1732 + 2.6992*i*	−0.1981 + 6.3801*i*
3.71	**0.2050 + 1.8235*i***	−0.0449 + 3.2979*i*	−0.01018 + 2.002*i*	−0.2203 + 5.7405*i*	−0.1522 + 2.6512*i*	−0.1908 + 6.3561*i*
3.84	**0.2394 + 1.6787*i***	−0.0183 + 3.2111*i*	**0.0452 + 1.9017*i***	−0.2100 + 5.6915*i*	−0.1252 + 2.5902*i*	−0.1862 + 6.3373*i*
4.00	**0.2725 + 1.5020*i***	**0.0143 + 3.1161*i***	**0.1164 + 1.7868*i***	−0.1976 + 5.6444*i*	−0.1021 + 2.5504*i*	−0.1805 + 6.3283*i*

eigenvalue result. CSMES is not capable of damping the tie-line oscillation while RSMES can significantly alleviate the oscillation. These results confirm that the RSMES designed with considering system uncertainties is much superior to the CSMES in terms of robustness.

5. Conclusions

This paper presents a robust SMES controller design based on inverse additive perturbation in interconnected power systems with wind farms. To improve the robustness of the SMES controller against system uncertainties, the unstructured system uncertainties represented by inverse additive perturbation have been included in the system modeling. The configuration of active and reactive power controllers is the practical first-order lead/lag compensator with single input. Control parameters of power controllers are optimized based on the enhancement of the robust stability margin. Simulation results in the six-area interconnected power system with wind farms confirm that the robustness of the proposed SMES under various situations such as heavy line flow, light line flow and wind power fluctuations is much superior to that of the SMES designed without considering robustness.

Acknowledgement

This work was supported by the Thailand Research Fund under the Basic Research Grant No. BRG5080019.

References

[1] S.A. Lone, M.U. Mufti, J. Power Sources 163 (2006) 604–605.
[2] J.G. Slootweg, W.L. Kling, Elect. Power Syst. Res. 67 (2003) 9–20.
[3] R.D. Fernández, R.J. Mantz, P.E. Battaiotto, Renew. Energy 32 (2007) 1676–1688.
[4] R.D. Fernandez, P.E. Battaiotto, R.J. Mantz, Int. J. Hydrogen Energy 33 (2008) 3543–3548.
[5] T. Ackermann, Wind Power in Power Systems, John Wiley & Sons Ltd., 2005.
[6] N. Jenkins, R. Allan, P. Crossley, D. Kirschen, G. Strbac, Embedded generation, IEE Power Energy Series, vol. 31, 2000.
[7] R.W. Boom, H. Perterson, IEEE Trans. Magn. 8 (1972) 701–703.
[8] H.J. Boenig, J.F. Hauer, IEEE Trans. Power Appl. Syst. 10 (1985) 302–309.
[9] M.G. Rabbani, J.B.X. Devotta, S. Elangovan, Energy Convers. Manage. 39 (1998) 931–942.
[10] J.B.X. Devotta, M.G. Rabbani, Energy Convers. Manage. 41 (2000) 493–504.
[11] S.C. Tripathy, Energy Convers. Manage. 38 (1997) 919–930.
[12] I. Ngamroo, Energy Convers. Manage. 46 (2005) 3060–3090.
[13] X. Chu, X. Jiang, Y. Lai, X. Wu, W. Liu, IEEE Trans. Appl. Supercond. 11 (2001) 1769–1772.
[14] J.B.X. Devotta, M.G. Rabbani, S. Elangovan, Energy Convers. Manage. 40 (1999) 23–37.
[15] M.K. Abdelsalam, R.W. Boom, H.A. Perterson, IEEE Trans. Magn. 23 (1987) 3275–3277.
[16] P. Gu, H.r. Petkov, M.M. Konstantinov, Robust control design with MATLAB, Springer, 2005. pp. 14–20.
[17] J. Kennedy, R.C. Eberhart, in: IEEE International Conference on Neural Network, vol. 4, 1995, pp. 1942–1948.
[18] J. Machowski, J. Bialek, J.R. Bumby, Power System Dynamics and Stability, John Wiley, 1997. pp. 346–350.
[19] N. Martin, L.T.G Lima, IEEE Trans. Power Syst. 5 (1990) 1455–1469.
[20] S. Dechanupaprittha, K. Hongesombut, M. Watanabe, Y. Mitani, I. Ngamroo, Int. J. Emerg. Electr. Power Syst. 9 (2008).
[21] Y.L. Abdel-Magid, M.A Abido, IEEE Trans. Power Syst. 18 (2003) 1125–1132.

INTERNATIONAL JOURNAL OF HYDROGEN ENERGY 34 (2009) 7131–7142

Available at www.sciencedirect.com

ScienceDirect

journal homepage: www.elsevier.com/locate/he

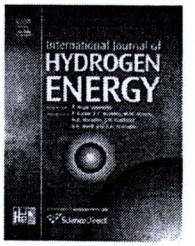

Review

Application of electrolyzer system to enhance frequency stabilization effect of microturbine in a microgrid system

Sitthidet Vachirasricirikul[a,*], Issarachai Ngamroo[b], Somyot Kaitwanidvilai[b]

[a]Department of Electrical Engineering, Faculty of Engineering, King Mongkut's Institute of Technology Ladkrabang, Bangkok 10520, Thailand
[b]Center of Excellence for Innovative Energy Systems, King Mongkut's Institute of Technology Ladkrabang, Bangkok 10520, Thailand

ARTICLE INFO

Article history:
Received 29 March 2009
Received in revised form
10 June 2009
Accepted 13 June 2009
Available online 23 July 2009

Keywords:
Electrolyzer system
Microturbine
Frequency stabilization
Microgrid
H_∞ loop shaping control
Particle swarm optimization

ABSTRACT

It is well known that the power output of microturbine can be controlled to compensate for load change and alleviate the system frequency fluctuations. Nevertheless, the microturbine may not adequately compensate rapid load change due to its slow dynamic response. Moreover, when the intermittent power generations from wind power and photovoltaic are integrated into the system, they may cause severe frequency fluctuation. In order to study the fast dynamic response, this paper applies electrolyzer system to absorb these power fluctuations and enhance the frequency control effect of microturbine in the microgrid system. The robust coordinated controller of electrolyzer and microturbine for frequency stabilization is designed based on a fixed-structure H_∞ loop shaping control. Simulation results exhibit the robustness and stabilizing effects of the proposed coordinated electrolyzer and microturbine controllers against system parameters variation and various operating conditions.

1. Introduction

According to the World Bank, more than 2 billion people around the world currently live in remote areas that are not yet connected to utility lines due to the limitations of investment costs, right of way difficulties and environment impacts [1]. To tackle this problem, the MG system [2,3] has been widely paid attentions. The MG is a cluster of the DG units, DS units and loads [4]. The MG system can be independently performed in an islanding mode and interconnected to the main utility grid [5]. Nowadays, there are many MG projects around the world such as the Consortium for Electric Reliability Technology Solutions (CERTS) project in the United States [6], the Aichi, Kyotango and Hachinohe MG projects in Japan [7], the MG project in Senegal [8], The Kythnos Island MG in Greece [9], the Labein MG in Spain [10], etc. The studied MG system consists of 100 kW WP, 25 kW PV, 100 kW MT, 5 kW FC, 70 kW ES of HOGEN® [11,12], CMS, load and TR connected to the UG. The capacity of MG system which is the possible maximum power generations from all sources in the MG, is equal to 230 kW. Note that ES is treated as the load with maximum absorbed power 70 kW. Here, the initial power generation in the MG is set to 100 kW which consists of 15 kW WP, 10 kW PV, 70 kW MT and 5 kW FC. This power generation balances with total loads 100 kW (50 kW ES and 50 kW load). As the primary power source, WP and PV are designed for

* Corresponding author. Tel./fax: +66 2326 4550.
E-mail address: sitthidetv@hotmail.com (S. Vachirasricirikul).

0360-3199/$ – see front matter
doi:10.1016/j.ijhydene.2009.06.050

Nomenclature

MG	microgrid
DG	distributed generation
DS	distributed storage
UG	utility grid
CMS	control and monitoring system
WP	wind power
PV	photovoltaic
MT	microturbine
FC	fuel cell
ES	electrolyzer system
H_2T	hydrogen tank
TR	transformer
P_{WP}	wind power output
P_{PV}	PV power output
P_{MT}	MT power output
P_{FC}	FC power output
P_{ES}	load power of ES
P_{tie}	tie line power
X_{tie}	tie line reactance
f_0	system frequency
ΔP	real power unbalance
Δf	change of frequency
ΔP_{MT}	change of MT power output
ΔP_{FC}	change of FC power output
ΔP_{ES}	change of ES load
ΔP_{tie}	change of tie line power
K_{PMTis}	proposed MT controller in islanding operation
K_{PESis}	proposed ES controller in islanding operation
K_{PMTug}	proposed MT controller in interconnected UG operation
K_{PESug}	proposed ES controller in interconnected UG operation
K_{MT}	droop property of MT output
K_{FC}	gain of FC
K_{ES}	gain of ES
T_{FC}	time constant of FC
T_{ES}	time constant of ES
M	inertia constant
D	damping coefficient
Base	base capacity

providing the power to load based on the different power demanding levels. In addition, the ES is designed to stabilize the system frequency and tie line power fluctuations. The power supply and demand balance control of the MG system are carried out by CMS. However, due to the lack of power supply from renewable sources, an MT is applied to supply the base load. Normally, the solar and wind energy are intermittent [13]. Consequently, the power production from WP and PV is variable. The real power unbalance in generation and load [14] causes severe frequency fluctuation in the MG system and tie line power fluctuation when the MG system is connected to the UG. To alleviate the frequency fluctuation, the MT is used to supply power for load change. Nevertheless, the MT cannot adequately compensate sudden load change and improve the severe frequency fluctuation instantaneously. This is because the MT has slow dynamic response due to the mechanical dynamic characteristics of governor and turbine [15–18]. Generally, the time constants of governor and turbine are in range of 0.2–0.5 s and 2.0–5.0 s, respectively [17,18]. To enhance the MT control effect, the ES control objective of HOGEN® is not only to build hydrogen for FC, but also to absorb rapid fluctuating power. The ES power consumption of HOGEN® can be controlled in the level of millisecond by tuning the pressure in the customer piping system. The electricity of ES is supplied by WP and PV. To solve the fluctuation problems of frequency and tie line power in the MG, the power outputs of MT and ES can be controlled by the CMS [15,16]. However, the controller parameters of MT

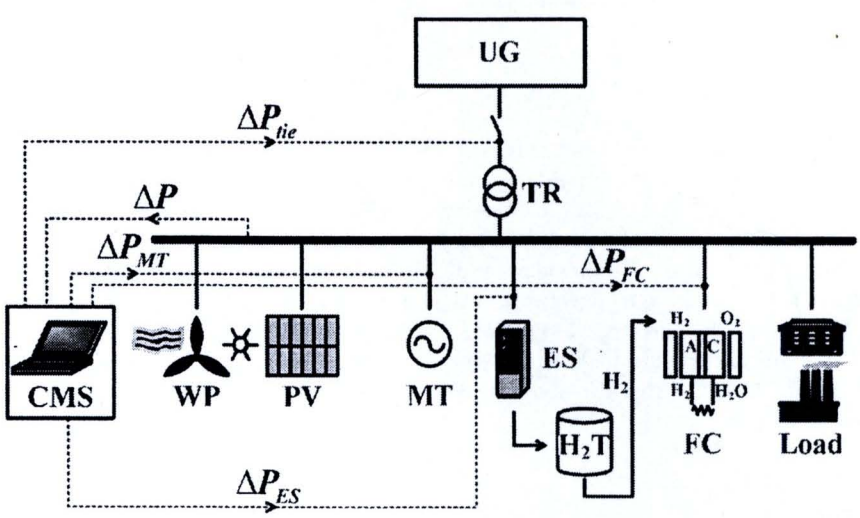

Fig. 1 – A microgrid system.

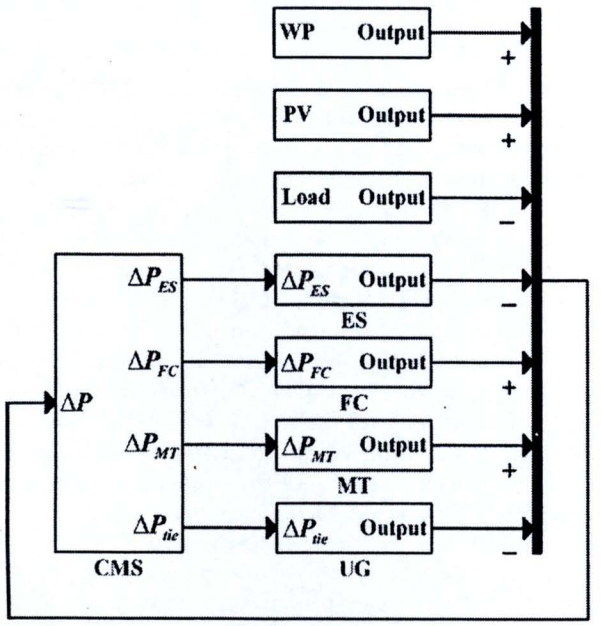

Fig. 2 – Microgrid system diagram.

and ES in Refs. [15,16] are separately designed for the islanding and interconnected UG modes. Hence, it cannot guarantee the well-coordinated control effects of MT and ES. Besides, these research works do not consider system uncertainties such as the system parameters variation, various generations and loadings, etc., in the control design. The robustness of the MT and ES controllers against the system uncertainties cannot be guaranteed.

To improve the robustness and coordinated control effect, an H_∞ control is one of the sophisticated design techniques [19,20]. Nevertheless, generally the designed H_∞ controller has a high order and is not easy to implement in real systems. Thus, the practical controller structures such as lead–lag compensator, proportional integral (PI), etc., are preferred because of their simple structure and low-order. However, the tuning of control parameters is very difficult to achieve the high robust controller against system uncertainties.

This paper proposes a new robust design of coordinated MT and ES controllers in CMS for stabilizing MG by using the particle swarm optimization (PSO) [21,22] based fixed-structure H_∞ loop shaping control. With fast dynamic control response, the ES is applied to enhance the frequency stabilizing effect of MT. The structure of MT and ES controllers is a PI. Based on the improvement of robust stability margin, the PI controller parameters of MT and ES in both the islanding and interconnected UG operations are simultaneously optimized. In the H_∞ loop shaping control, the performance and robust stability conditions are formulated as the objective function in the optimization problem. The normalized coprime factor [23,24] is used to form system uncertainties. Simulation results display the superior robustness and stabilizing effects of the proposed coordinated MT and ES controllers in comparison with the MT and ES controllers [15].

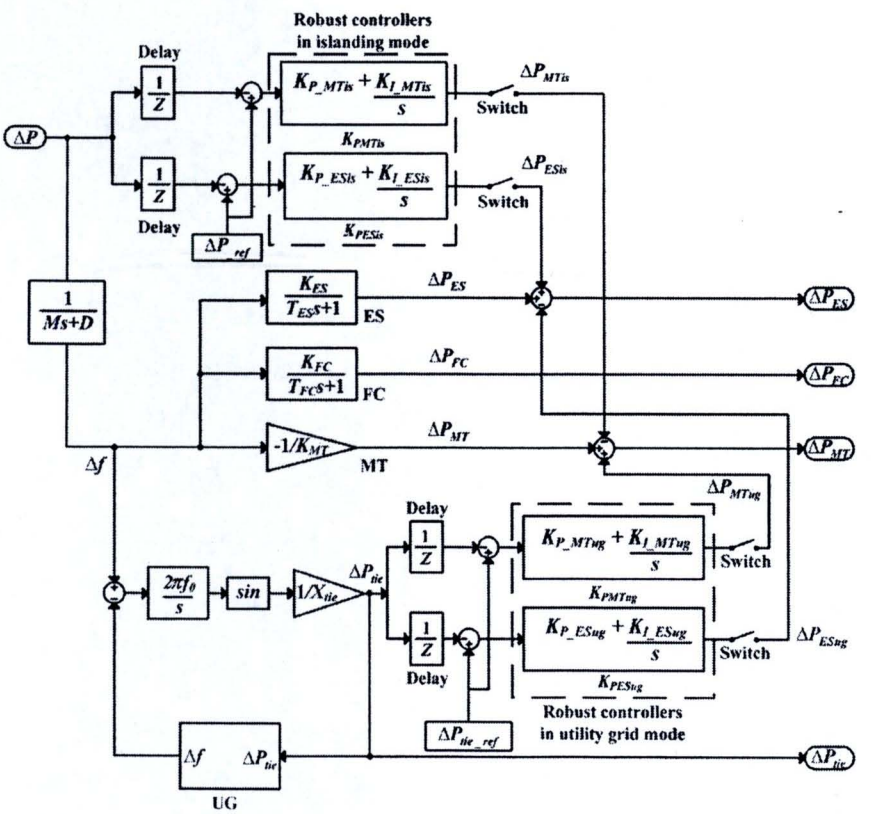

Fig. 3 – Linearized block diagram of CMS.

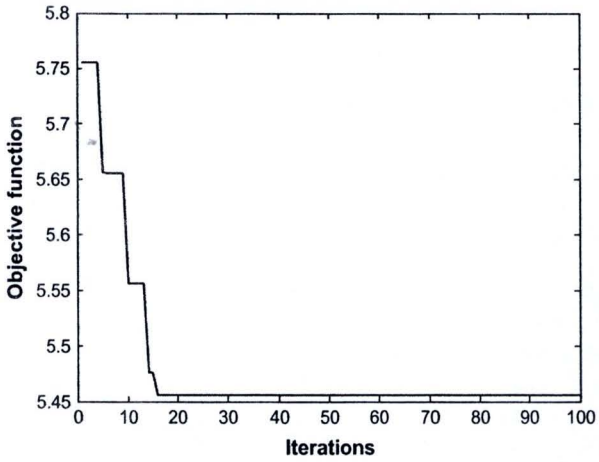

Fig. 4 – Objective function versus iteration.

This paper is organized as follows. First, problem formulation is described in Section 2. Next, Section 3 shows system modeling. Subsequently, Section 4 shows simulation results. Finally, Conclusion is given.

2. Problem formulation

As depicted in Fig. 1, the MG system consists of the WP, PV, MT, ES, H_2T, FC, CMS, load, TR and UG. The MT is used to supply power to the MG system when the WP and PV cannot sufficiently provide. The ES is utilized to produce hydrogen (H_2) as a fuel for FC by consuming some power outputs from WP and PV. The generated H_2 is stored in the H_2T. Naturally, the power generations from WP and PV are very unstable and intermittent. Thus, the real power unbalance causes the frequency fluctuation. Moreover, the frequency fluctuation under the interconnected UG causes the tie line power fluctuation. To solve this problem, the proposed coordinated MT and ES controllers in CMS are applied to stabilize the MG system. Here, the performance of ES is augmented to enhance the frequency stabilization effect of MT. It is supposed that the amount of hydrogen generated by ES in the hydrogen tank has more than 50% of the hydrogen tank capacity [25,26] for operating the FC throughout the test time period. Accordingly, the calculation details of hydrogen production or consumption are not provided in this work.

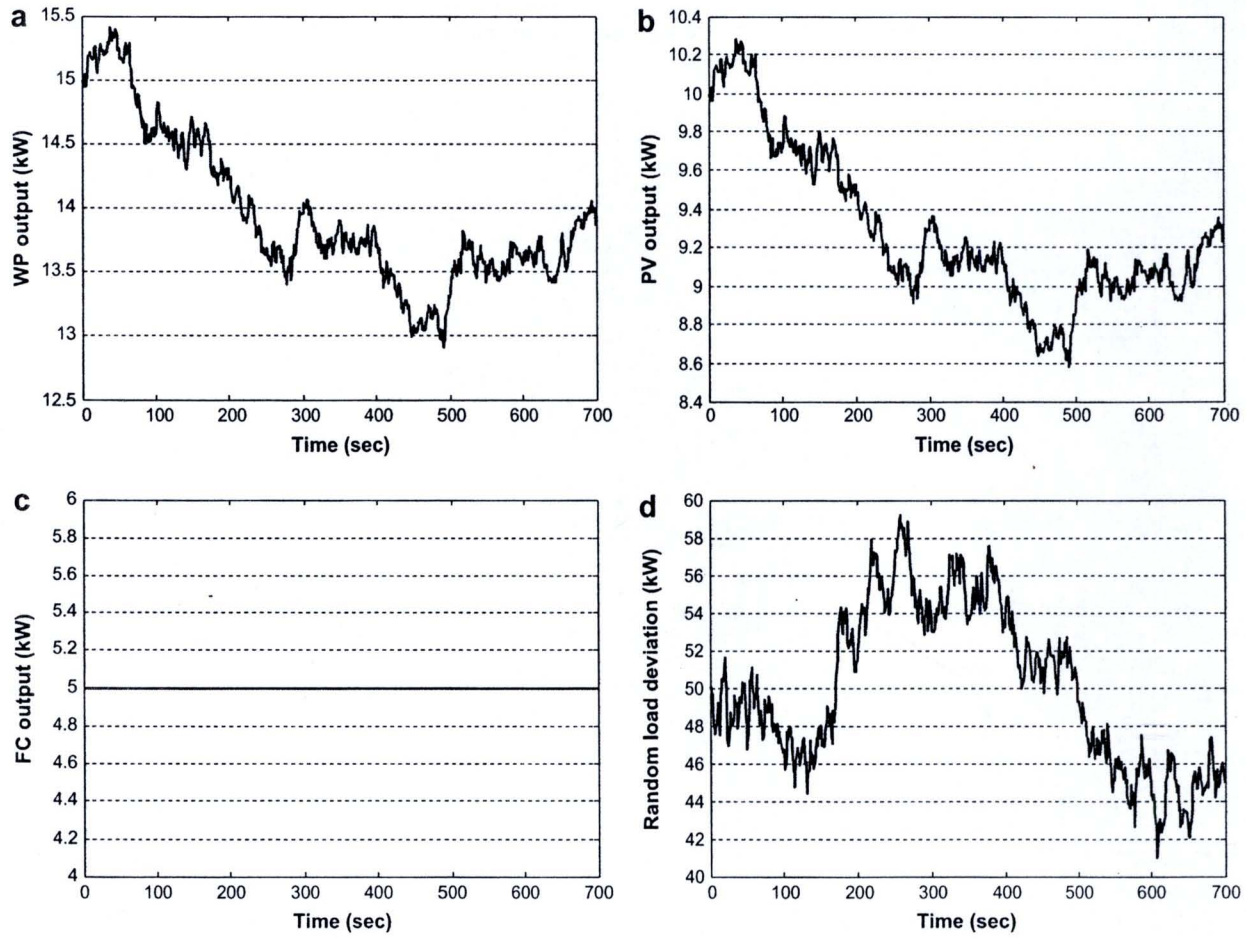

Fig. 5 – (a) WP output. (b) PV output. (c) FC output. (d) Random load deviation (normal case).

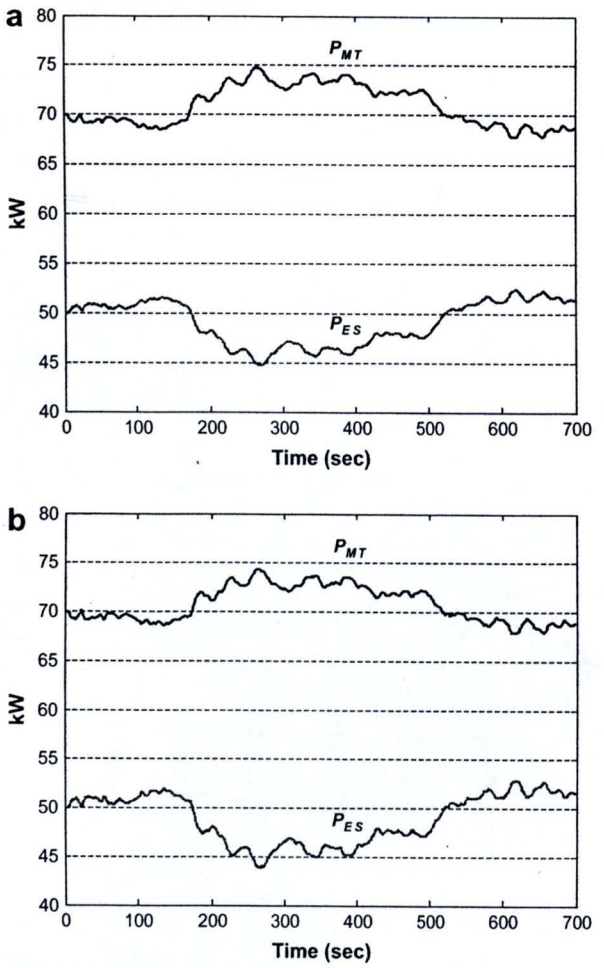

Fig. 6 – (a) Power outputs with the MT and ES controls under normal case (conventional method). (b) Power outputs with the MT and ES controls under normal case (proposed method).

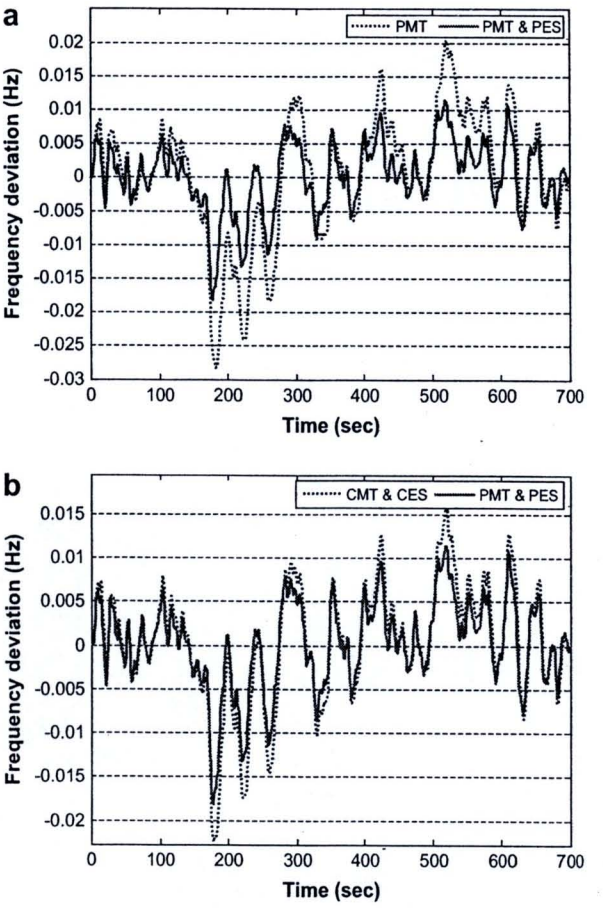

Fig. 7 – (a) Frequency deviation under islanding operation with the controls of PMT and PMT & PES. (b) Frequency deviation under islanding operation with the controls of CMT & CES and PMT & PES.

3. System modeling

The MG system diagram is depicted in Fig. 2. The proposed coordinated MT and ES controllers in CMS are utilized to minimize the feedback input signal of the real power unbalance (ΔP) in the MG system. The linearized block diagram of CMS is shown in Fig. 3. The delay times of the islanding and interconnected UG operations in Fig. 3 are for every 5 and 4 s, respectively. Note that the structures of ES and FC are high-order models and have the nonlinear characteristics. Nevertheless, the frequency control problem in electric power systems due to small disturbances can be generally studied in a linearized system [17,18]. Hence, the transfer functions of ES and FC are approximately represented by the first-order transfer function [25,27]. Besides, the descriptions of WP and PV models are explained in Appendix B.

Here, it is considered that the FC power output (P_{FC}) is set to a constant value of 5 kW throughout the test time period. Accordingly, the FC power is not used for real-time control of the power unbalance in the MG system. System parameters are given in Refs. [15,16]. The linearized state equation can be expressed as

$$\Delta\dot{X} = A\Delta X + B\Delta u \tag{1}$$

$$\Delta Y = C\Delta X + D\Delta u \tag{2}$$

$$\Delta P_{MTis} = K_{PMTis}(s)\Delta P \tag{3}$$

$$\Delta P_{ESis} = K_{PESis}(s)\Delta P \tag{4}$$

$$\Delta P_{MTug} = K_{PMTug}(s)\Delta P_{tie} \tag{5}$$

$$\Delta P_{ESug} = K_{PESug}(s)\Delta P_{tie} \tag{6}$$

$$K_{PMTis}(s) = K_{P\_MTis} + K_{I\_MTis}/s \tag{7}$$

$$K_{PESis}(s) = K_{P\_ESis} + K_{I\_ESis}/s \tag{8}$$

$$K_{PMTug}(s) = K_{P\_MTug} + K_{I\_MTug}/s \tag{9}$$

$$K_{PESug}(s) = K_{P\_ESug} + K_{I\_ESug}/s \tag{10}$$

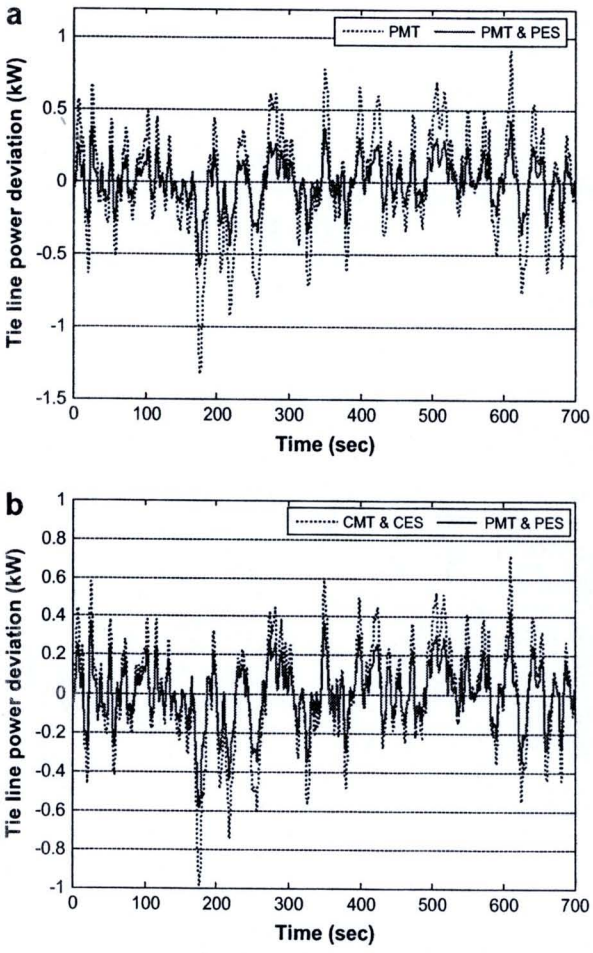

Fig. 8 – (a) Tie line power deviation under interconnected UG operation with the controls of PMT and PMT & PES. (b) Tie line power deviation under interconnected UG operation with the controls of CMT & CES and PMT & PES.

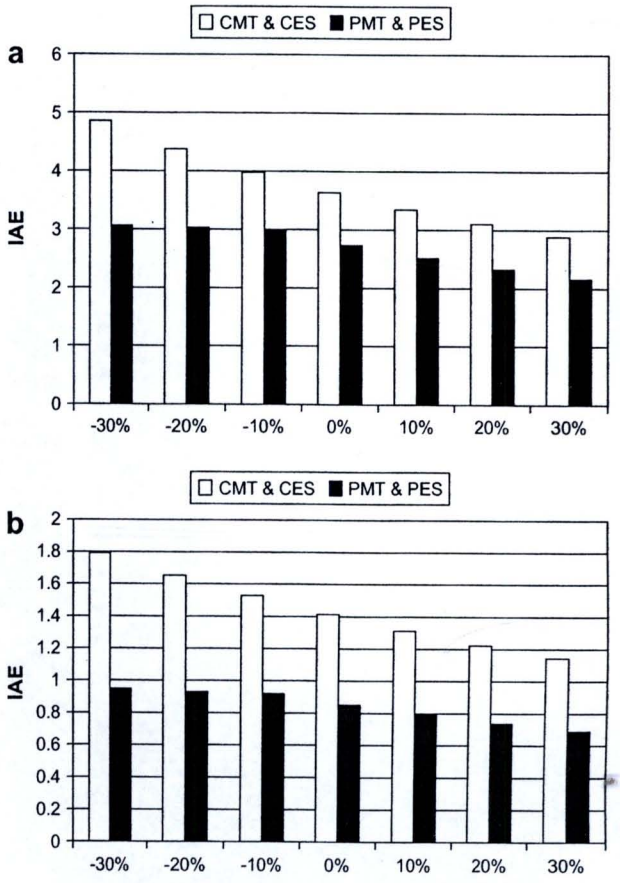

Fig. 9 – (a) IAE of Δf under islanding operation. (b) IAE of ΔP_{tie} under interconnected UG operation.

where the state vector $\Delta X = [\Delta P_{ES}\ \Delta P_{tie}\ \Delta f]^T$. ΔP_{ES}, ΔP_{tie} and Δf are small changes of ES load, tie line power and frequency, respectively. The output vector $\Delta Y = [\Delta P\ \Delta P_{tie}]^T$, the control output signal $\Delta u = [\Delta P_{MTis}\ \Delta P_{ESis}\ \Delta P_{MTug}\ \Delta P_{ESug}]^T$. ΔP_{MTis} and ΔP_{ESis} are small changes in the islanding operation of MT output and ES load, respectively. ΔP_{MTug} and ΔP_{ESug} are small changes in the interconnected UG operation of MT output and ES load, respectively. $K_{PMTis}(s)$, $K_{PESis}(s)$ and $K_{PMTug}(s)$, $K_{PESug}(s)$ are the proposed MT and ES controllers in the islanding and interconnected UG operations, respectively. Note that all four controllers are performed in the interconnected UG mode while $K_{PMTis}(s)$ and $K_{PESis}(s)$ are operated in the islanding mode. The system (1) is a multi-input multi-output (MIMO) system and referred to the nominal plant G.

The proposed robust controllers are implemented in the CMS which consists of the robust controllers in islanding mode (K_{PMTis} and K_{PESis}) and the robust controllers in utility grid mode (K_{PMTug} and K_{PESug}) as shown in Fig. 3. In this paper, the MATAB program is applied to develop the off-line parameters tuning of the proposed robust controllers based on the fixed-structure H_∞ loop shaping control. It should be noted that the MATLAB program can be developed to on line parameters tuning of the controllers. Based on the system generating and loading conditions, the control parameters can be adjusted and implemented in real time [28].

The design description of the relevant control theory such as H_∞ loop shaping control, PSO is given in Appendix A.

4. Simulation results

In this section, robust control design and simulation studied are carried out. The lower and upper bounds of search parameters and PSO parameters are set as follows: $K_{W1}, K_{W2}, K_{W3}, K_{W4} \in [0.0001\ \ 1000]$, $a_1, a_2, a_3, a_4 \in [0.0001\ \ 100]$, $b_1, b_2, b_3, b_4 \in [0.0001\ \ 100]$, $\gamma_{min} \in [1\ \ 4]$, $K_{P\_MTis} \in [0.0001\ \ 1]$, $K_{I\_MTis} \in [0.0001\ \ 1]$, $K_{P\_ESis} \in [0.0001\ \ 1]$, $K_{I\_ESis} \in [0.0001\ \ 1]$, $K_{P\_MTug} \in$

Table 1 – Changed system parameters under islanding operation.

System parameters	−30%	−20%	−10%	0%	10%	20%	30%
K_{ES}	70	80	90	100	110	120	130
T_{ES}	42	48	54	60	66	72	78
K_{MT}	0.028	0.032	0.036	0.040	0.044	0.048	0.052
M	7	8	9	10	11	12	13
D	0.7	0.8	0.9	1.0	1.1	1.2	1.3

Table 2 – Changed system parameters under interconnected UG operation.

System parameters	−30%	−20%	−10%	0%	10%	20%	30%
K_{ES}	70	80	90	100	110	120	130
T_{ES}	42	48	54	60	66	72	78
K_{MT}	0.028	0.032	0.036	0.040	0.044	0.048	0.052
M	7	8	9	10	11	12	13
D	0.7	0.8	0.9	1.0	1.1	1.2	1.3
X_{tie}	0.0504	0.0576	0.0648	0.0720	0.0792	0.0864	0.0936

$[0.0001\ \ 0.5]$, $K_{I\_MTug} \in [0.0001\ \ 0.5]$, $K_{P\_ESug} \in [0.0001\ \ 0.5]$, $K_{I\_ESug} \in [0.0001\ \ 0.5]$, PSO sizes = 50, maximum iterations = 100, $c_1 = 2$, $c_2 = 2$, $w_{min} = 0.4$ and $w_{max} = 0.9$. Thus, the weighting functions are suitably selected as

$$W_{MTis} = 910.9754\frac{s + 48.9961}{s + 96.9381}, \quad W_{ESis} = 806.7562\frac{s + 46.9839}{s + 93.9256} \tag{11}$$

$$W_{MTug} = 889.9907\frac{s + 41.9219}{s + 90.9769}, \quad W_{ESug} = 886.9561\frac{s + 44.9197}{s + 95.9942} \tag{12}$$

Based on these weighting functions, the shaped plant G_s can be established. This results in $\gamma_{min} = 2.5849$. The convergence curve of the objective function is illustrated in Fig. 4.

Consequently, the proposed MT and ES controllers (PMT & PES) in the islanding and interconnected UG operations of CMS are obtained as

$$K_{PMTis}(s) = 0.4300 + 0.6607/s \tag{13}$$

$$K_{PESis}(s) = 0.4397 + 0.8951/s \tag{14}$$

$$K_{PMTug}(s) = 0.1493 + 0.3994/s \tag{15}$$

$$K_{PESug}(s) = 0.1500 + 0.3999/s \tag{16}$$

In simulation study, the robustness and stabilizing effects of PMT & PES are compared with those of CMT & CES in CMS [15]. It is assumed that the WP, PV and FC outputs and the random

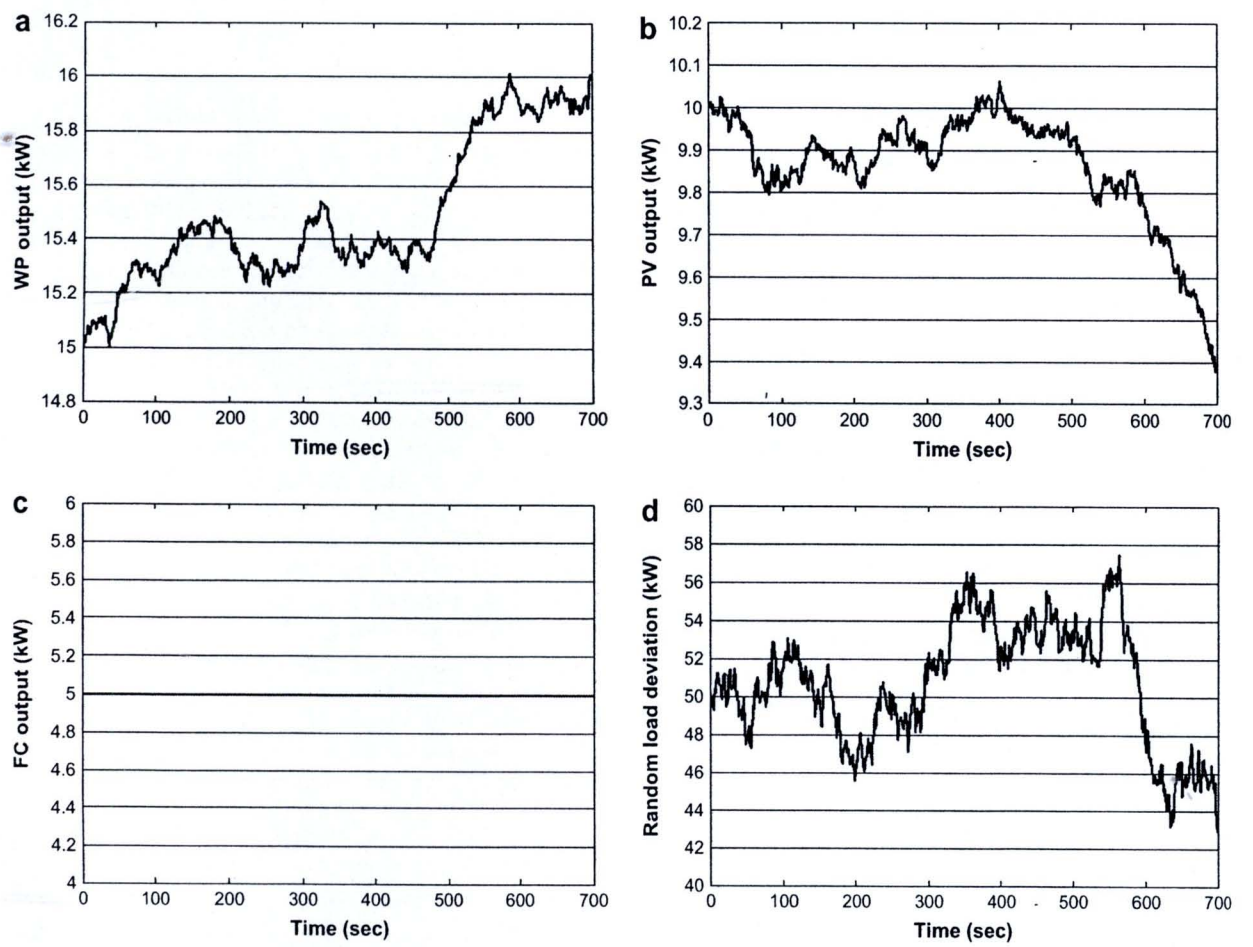

Fig. 10 – (a) WP output. (b) PV output. (c) FC output. (d) Random load deviation (changed system parameters case).

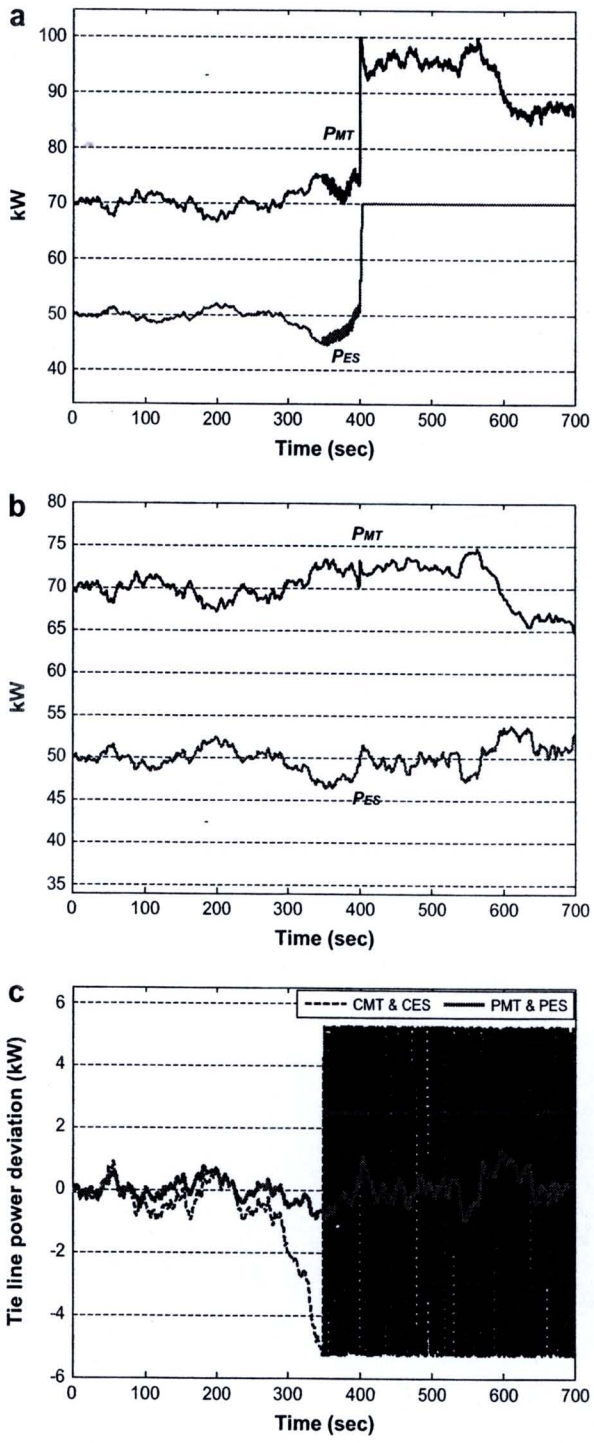

Fig. 11 – (a) Power outputs with the MT and ES controls (conventional method). (b) Power outputs with the MT and ES controls (proposed method). (c) Tie line power deviation with changed system parameters.

load deviation in Fig. 5 are applied to the MG system under the islanding and interconnected UG operations. From Fig. 5, the load demand is much higher than the PV and WP power production. Therefore, MTs in both conventional and proposed methods supply the insufficient power to the system while ESs of both methods absorb power from the system as shown in Fig. 6(a) and (b).

In the islanding operation, the frequency deviation under only PMT and PMT & PES controls is demonstrated in Fig. 7(a). The frequency fluctuation is significantly damped by PMT & PES in comparison with only PMT. This shows that the addition of ES highly improves the stabilizing effect of MT. The frequency fluctuation with the coordinated controls of PMT & PES and CMT & CES in the islanding operation is shown in Fig. 7(b). The frequency fluctuation under the control of PMT & PES is lower than that of CMT & CES.

For the interconnected UG operation, the tie line power fluctuation under only PMT and PMT & PES controls is shown in Fig. 8(a). The stabilizing effect of PMT & PES on a tie line power deviation is higher than that of only PMT. With the coordinated controls of PMT & PES and CMT & CES, the tie line power fluctuation is illustrated in Fig. 8(b). The power stabilizing effect of CMT & CES is lower than that of PMT & PES. This indicates the higher coordinated control effect of PMT & PES.

In order to investigate the robustness of PMT & PES against the variation of system parameters in the islanding and interconnected UG operations, the integral absolute error (IAE) of frequency deviation (Δf) and tie line power deviation (ΔP_{tie}) under the WP, PV and FC outputs and the random load deviation in Fig. 5 are determined as

$$\text{IAE of } \Delta f = \int_0^{700} |\Delta f| dt \tag{17}$$

$$\text{IAE of } \Delta P_{tie} = \int_0^{700} |\Delta P_{tie}| dt \tag{18}$$

Fig. 9(a) demonstrates the IAE values of Δf under the islanding operation while system parameters K_{ES}, T_{ES}, K_{MT}, M and D are changed from −30% to +30% of the normal values. In Fig. 9(b), the IAE values of ΔP_{tie} under interconnected UG operation are calculated while system parameters K_{ES}, T_{ES}, K_{MT}, M, D and X_{tie} are changed from −30% to +30% of the normal values. The changed parameters under islanding and interconnected UG operations are shown in Tables 1 and 2, respectively.

From Fig. 9(a), the IAE values of CMT & CES highly increase while system parameters decrease. In contrast, the changes of IAE values in the case of PMT & PES are lower than those of CMT & CES. Also, the IAE values of CMT & CES in Fig. 9(b) largely increase when system parameters decrease. On the other hand, the PMT & PES gives a lower change in IAE than CMT & CES. These show that PMT & PES is greatly robust to system parameters variation.

Next, it is supposed that the system is operated in an interconnected UG mode under the WP, PV and FC outputs and the random load deviation as shown in Fig. 10. At $t = 400$ s, the MT controller (K_{PMTis}) in the islanding operation is accidentally disconnected while three controllers (K_{PESis}, K_{PMTug} and K_{PESug}) are still operating for $t > 400$ s in order to investigate the robustness of the remaining controllers under the outage of one controller. During the simulation, it is assumed that K_{ES}, T_{ES}, K_{MT}, M and X_{tie} are decreased by 30% from the normal values, D is changed from 1 to −0.399. This implies that the values of the gain of ES, time constant of ES, droop property of MT, inertia constant and tie line reactance are supposedly decreased by 30% from their normal values. Also, D is reduced from positive damping to

negative damping. The negative damping can occur when the MG system is operating at the unstable point. Simulation results of the power outputs with the MT and ES controls and the tie line power fluctuation are shown in Fig. 11.

Fig. 11(a) and (b) shows power supplied by MTs and power absorbed by ESs in both conventional and proposed methods, respectively. Clearly, the power outputs of PMT & PES can be controlled effectively. On the contrary, the CMT & CES cannot manage the power unbalance in the MG system. Fig. 11(c) explains that the CMT & CES completely fails to stabilize the tie line power oscillation. The MG system becomes unstable. In contrast, the PMT & PES is robust against system parameters variation and controller outage situation. The PMT & PES successfully alleviates the power fluctuation. This result confirms the superior robustness and coordinated control effects of PMT & PES over the CMT & CES.

5. Conclusions

In this paper, the application of ES to enhance the robust frequency stabilization effects of MT has been presented. The robust coordinated controller design of ES and MT for frequency stabilization is based on a PSO-based fixed-structure H_∞ loop shaping control. With the PI structure, the proposed robust controller can be easily implemented in real systems. Simulation results confirm that the ES significantly improves the frequency stabilizing effect of MT. In addition, the proposed coordinated MT and ES show the superior robustness against system parameters variation and various operation situations.

Acknowledgements

This work was supported by the Thailand Research Fund under the Basic Research Grant No.BRG5080019 and the King Mongkut's Institute of Technology Ladkrabang Research Fund.

Appendix A

The proposed control design based on PSO-based fixed-structure H_∞ loop shaping control is described as follows:

A1 Loop shaping

A pre-compensator (W_1) and a post-compensator (W_2) in Fig. A1 are employed to form the shaped plant $G_s = W_2GW_1$, which is enclosed by a solid line. The designed robust controller $K = W_1K_\infty W_2$ is enclosed by a dotted line where K_∞ is the H_∞ controller.

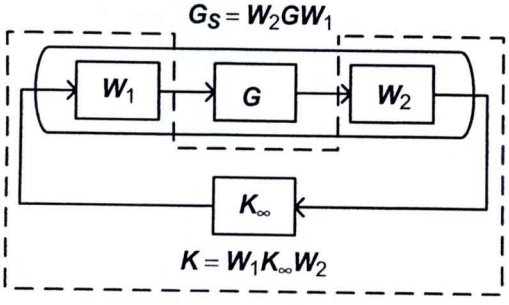

Fig. A1 – Shaped plant G_s and robust controller K.

A2 Weighting function selection

In this section, the weighting functions (W_1 and W_2) are chosen such that the open loop of the shaped plant has the following conflict properties [23,24]:

- To achieve a good performance tracking and good disturbance rejection, large open-loop gain (normally at low frequency range) is required. .
- To achieve a good robust stability and sensor noise rejection, small open-loop gain (normally at high frequency range) is required.

In Fig. A1, the shaped plant is established by weighting functions. Because the nominal plant G is an MIMO system, the weighting functions are selected as

$$W_1 = \begin{bmatrix} W_{MTis} & 0 & 0 & 0 \\ 0 & W_{ESis} & 0 & 0 \\ 0 & 0 & W_{MTug} & 0 \\ 0 & 0 & 0 & W_{ESug} \end{bmatrix}, \quad W_2 = I$$

$$W_{MTis} = K_{W1}\frac{s+a_1}{s+b_1}, \quad W_{ESis} = K_{W2}\frac{s+a_2}{s+b_2}$$

$$W_{MTug} = K_{W3}\frac{s+a_3}{s+b_3}, \quad W_{ESug} = K_{W4}\frac{s+a_4}{s+b_4} \tag{A1}$$

where W_{MTis}, W_{ESis} and W_{MTug}, W_{ESug} are the weighting functions of MT output and ES load in the islanding and interconnected UG modes, respectively. K_{W1}, a_1, b_1, K_{W2}, a_2, b_2, K_{W3}, a_3, b_3, K_{W4}, a_4 and b_4 are positive values, because the peak resonance of the open-loop system occurs in the low frequency range. Therefore, W_1 is set as a high-pass filter ($a_1 < b_1$, $a_2 < b_2$, $a_3 < b_3$, $a_4 < b_4$).

A3 H_∞ robust stabilization problem formulation

In this work, variation of system parameters, generating and loading conditions etc., are defined as unstructured system uncertainties. Because these uncertainties cannot be clearly explained by mathematic equations, the coprime

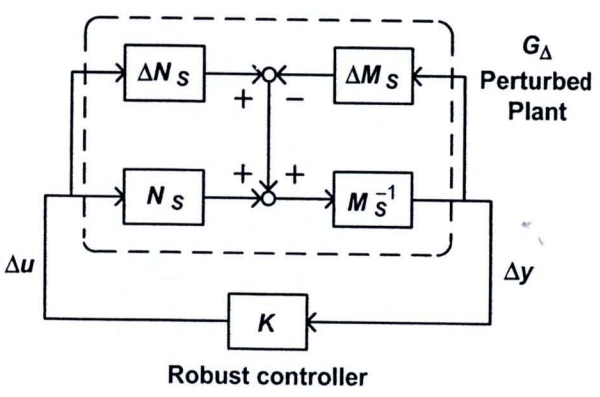

Fig. A2 – H_∞ robust stabilization problem.

factorization is used to represent these unstructured uncertainties. A shaped plant G_s is expressed in the form of normalized left coprime factor $G_s = M_s^{-1}N_s$, when the perturbed plant G_Δ is defined as

$$G_\Delta = \left\{(M_s + \Delta M_s)^{-1}(N_s + \Delta N_s) : \|[\Delta N_s \ \Delta M_s]\|_\infty \le 1/\gamma\right\} \quad \text{(A2)}$$

where ΔM_s and ΔN_s are stable unknown transfer functions which represent unstructured uncertainties in the nominal plant G. The H_∞ robust stabilization problem can be established by G_Δ and K as depicted in Fig. A2. The objective of robust control design is to stabilize not only the nominal plant G but also the family of perturbed plant G_Δ. In (A2), $1/\gamma$ is defined as the robust stability margin. The maximum stability margin in the face of system uncertainties is given by the lowest achievable value of γ. Therefore, γ_{min} implies the largest size of system uncertainties that can exist without destabilizing the closed-loop system in Fig. A2. The value of γ_{min} can be calculated from

$$\gamma_{min} = \sqrt{1 + \lambda_{max}(XZ)} \quad \text{(A3)}$$

where $\lambda_{max}(XZ)$ denotes the maximum eigenvalue of XZ. For minimal state-space realization (A,B,C,D) of G_s, the values of X and Z are unique positive solutions to the generalized control algebraic Riccati equation

$$(A - BS^{-1}D^TC)^TX + X(A - BS^{-1}D^TC) - XBS^{-1}B^TX + C^TR^{-1}C = 0 \quad \text{(A4)}$$

and the generalized filtering algebraic Riccati equation

$$(A - BS^{-1}D^TC)Z + Z(A - BS^{-1}D^TC)^T - ZC^TR^{-1}CZ + BS^{-1}B^T = 0 \quad \text{(A5)}$$

where $R = I + DD^T$ and $S = I + D^TD$. Note that no iteration on γ is needed to solve for γ_{min}. To ensure the robust stability of the nominal plant G, the weighting functions are chosen so that $1.0 \le \gamma_{min} < 4.0$ [23,24].

A4 Generate the objective function

In Fig. A1, K_∞ can be determined as follows:

$$K_\infty = W_1^{-1}K(s) \quad \text{(A6)}$$

Because $W_2 = I$, the necessary and sufficient condition of the robust controller K(s) [23,24] is

$$\left\|\begin{bmatrix} I \\ K_\infty \end{bmatrix}(I - G_sK_\infty)^{-1}[I\ G_s]\right\|_\infty \le \gamma \quad \text{(A7)}$$

Substitute (A6) in (A7), that is

$$\left\|\begin{bmatrix} I \\ W_1^{-1}K(s) \end{bmatrix}(I - G_sW_1^{-1}K(s))^{-1}[I\ G_s]\right\|_\infty \le \gamma \quad \text{(A8)}$$

Therefore, the objective function can be defined as

$$\text{Minimize } \gamma_{min} + \left\|\begin{bmatrix} I \\ W_1^{-1}K(s) \end{bmatrix}(I - G_sW_1^{-1}K(s))^{-1}[I\ G_s]\right\|_\infty \quad \text{(A9)}$$

Subject to

$$K_{W1\text{-}4,min} \le K_{W1\text{-}4} \le K_{W1\text{-}4,max}, \quad a_{1\text{-}4,min} \le a_{1\text{-}4} \le a_{1\text{-}4,max}, \quad b_{1\text{-}4,min} \le b_{1\text{-}4} \le b_{1\text{-}4,max},$$

$$\gamma_{min,min} \le \gamma_{min} < \gamma_{min,max}, \quad a_1 < b_1, \quad a_2 < b_2, \quad a_3 < b_3, \quad a_4 < b_4, \quad |G|_{dB,lf} < |G_s|_{dB,lf},$$

$$K_{P\_MTis,min} \le K_{P\_MTis} \le K_{P\_MTis,max}, \quad K_{I\_MTis,min} \le K_{I\_MTis} \le K_{I\_MTis,max},$$

$$K_{P\_ESis,min} \le K_{P\_ESis} \le K_{P\_ESis,max}, \quad K_{I\_ESis,min} \le K_{I\_ESis} \le K_{I\_ESis,max},$$

$$K_{P\_MTug,min} \le K_{P\_MTug} \le K_{P\_MTug,max}, \quad K_{I\_MTug,min} \le K_{I\_MTug} \le K_{I\_MTug,max},$$

$$K_{P\_ESug,min} \le K_{P\_ESug} \le K_{P\_ESug,max}, \quad K_{I\_ESug,min} \le K_{I\_ESug} \le K_{I\_ESug,max} \quad \text{(A10)}$$

where $K_{W1\text{-}4,min}$, $a_{1\text{-}4,min}$, $b_{1\text{-}4,min}$ and $K_{W1\text{-}4,max}$, $a_{1\text{-}4,max}$, $b_{1\text{-}4,max}$ are the minimum and maximum of the positive values of MT output and ES load in the islanding and interconnected UG operations; respectively. $\gamma_{min,min}$ and $\gamma_{min,max}$ are the minimum and maximum values of γ_{min}, respectively. $|G|_{dB,lf}$ and $|G_s|_{dB,lf}$ are the open-loop gains of the nominal plant G and the shaped plant G_s at low frequency range, respectively. $K_{P\_MTis,min}$, $K_{I\_MTis,min}$, $K_{P\_ESis,min}$, $K_{I\_ESis,min}$ and $K_{P\_MTis,max}$, $K_{I\_MTis,max}$, $K_{P\_ESis,max}$, $K_{I\_ESis,max}$ are the minimum and maximum of PI parameters of K_{PMTis} and K_{PESis}, respectively. $K_{P\_MTug,min}$, $K_{I\_MTug,min}$, $K_{P\_ESug,min}$, $K_{I\_ESug,min}$ and $K_{P\_MTug,max}$, $K_{I\_MTug,max}$, $K_{P\_ESug,max}$, $K_{I\_ESug,max}$ are the minimum and maximum of PI parameters of K_{PMTug} and K_{PESug}, respectively.

In (A9), the weighting functions are selected by tuning the γ_{min} value so that the open-loop gains of the shaped plant G_s are more than those of the nominal plant G at the low frequency range and the roll-off rates are approximately 20 dB/decade [23,24].

A5 PSO algorithm

The PSO algorithm [21,22] is described as follows:

1. Specify the parameters of PSO. Initialize a population of the particles with random positions and velocities within upper and lower bound values of the problem space. Set iteration count as iter = 1.
2. Evaluate the objective function for each particle using (A9).
3. Compare the fitness value of each particle with its best position for particle (*pbest*). The best fitness value among all the *pbests* is the best position of all particles in the group (*gbest*).
4. Update the velocity v_i and position of particle x_i by

$$v_{i+1} = w \cdot v_i + c_1 \cdot \text{rand}_1 \cdot (pbest - x_i) + c_2 \cdot \text{rand}_2 \cdot (gbest - x_i) \quad \text{(A11)}$$

$$x_{i+1} = x_i + v_{i+1} \quad \text{(A12)}$$

$$w = w_{max} - ((w_{max} - w_{min})/\text{iter}_{max}) \cdot \text{iter} \quad \text{(A13)}$$

where c_1 and c_2 are the cognitive and social acceleration factors, respectively. rand_1 and rand_2 are the random

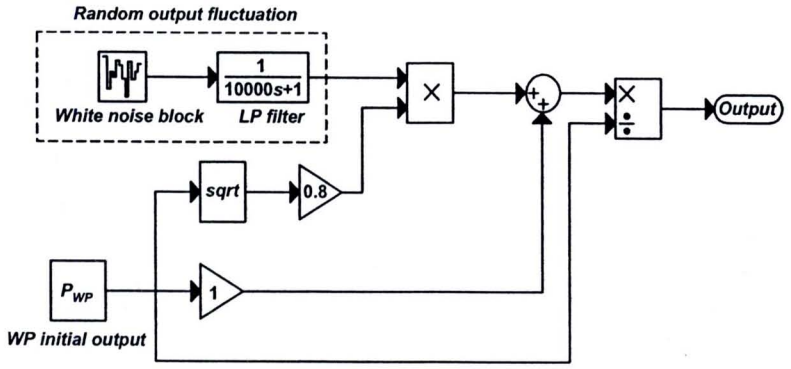

Fig. B1 – WP model.

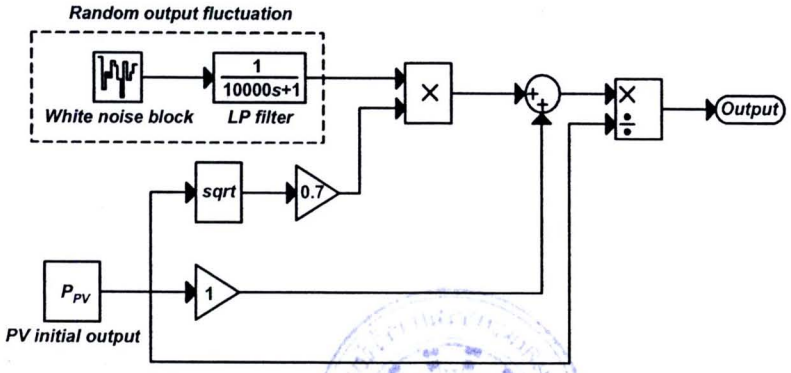

Fig. B2 – PV model.

numbers of range (0,1). w is inertia weight factor. w_{min} and w_{max} are the minimum and maximum inertia weight factors, respectively. iter and $iter_{max}$ are the iteration count and maximum iteration, respectively.

5. Increment iteration for a step (iter = iter + 1).
6. When the maximum number of iterations is arrived, stop the process. Otherwise go to process 2.

Appendix B

In this paper, the standard deviations of WP and PV are mathematically evaluated as [15,16]:

$$dP_{WP} = 0.8\sqrt{P_{WP}} \quad \text{(B1)}$$

$$dP_{PV} = 0.7\sqrt{P_{PV}} \quad \text{(B2)}$$

The WP and PV models [15,16] are exhibited in Figs. B1 and B2, respectively. The WP and PV standard deviations in (B1) and (B2) are multiplied by a random output fluctuation derived from the white noise block with a low pass filter in MATLAB/SIMULINK in order to evaluate the random power fluctuation.

REFERENCES

[1] Ackermann T. Wind power in power systems. John Wiley & Sons, Ltd; 2005.
[2] Obara S'Y. Analysis of a fuel cell micro-grid with a small-scale wind turbine generator. International Journal of Hydrogen Energy 2007;32:323–36.
[3] Obara S'Y. Equipment plan of compound interconnection micro-grid composed from diesel power plants and solid polymer membrane-type fuel cell. International Journal of Hydrogen Energy 2008;33:179–88.
[4] Kroposki B, Lasseter R, Lse T, Morozumi S, Papathanassiou S, Hatziargyriou N. Making microgrids work. IEEE Power and Energy Magazine 2008;6:40–53.
[5] Katiraei F, Iravani R, Hatziargyriou N, Dimeas A. Microgrids management. IEEE Power and Energy Magazine 2008;6:54–65.
[6] Lasseter RH. CERTS microgrid. IEEE International Conference on System of Systems Engineering; 2007. p. 1–5.
[7] Morozumi S. Micro-grid demonstration projects in Japan. IEEE Power Conversion Conference; 2007. p. 635–42.
[8] Camblong H, Sarr J, Niang AT, Curea O, Alzola JA, Sylla EH, et al. Micro-grids project, part 1: analysis of rural electrification with high content of renewable energy sources in Senegal. Renewable Energy 2009;34:2141–50.
[9] Hatziargyriou N, Asano H, Iravani R, Marnay C. Microgrids. IEEE Power and Energy Magazine 2007;5:78–94.

[10] Barnes M, Ventakaramanan G, Kondoh J, Lasseter R, Asano H, Hatziargyriou N, et al. Real-world microgrids – an overview. IEEE International Conference on System of Systems Engineering; 2007. p. 1–8.
[11] Available from: <http://www.protonenergy.com>.
[12] Available from: <http://www.distributed-energy.com>.
[13] Do Sacramento EM, De Lima LC, Oliveira CJ, Veziroglu T Nejat. A hydrogen energy system and prospects for reducing emissions of fossil fuels pollutants in the Ceará state – Brazil. International Journal of Hydrogen Energy 2008;33: 2132–7.
[14] Obara S. Load response characteristics of a fuel cell microgrid with control of number of units. International Journal of Hydrogen Energy 2006;31:1819–30.
[15] Li X, Song YJ, Han SB. Study on power quality control in multiple renewable energy hybrid microgrid system. IEEE PowerTech 2007:2000–5.
[16] Li X, Song YJ, Han SB. Frequency control in micro-grid power system combined with electrolyzer system and fuzzy PI controller. Journal of Power Sources 2008;180:468–75.
[17] Kundur P. Power system stability and control. McGrawHill, Inc; 1993.
[18] Saadat H. Power system analysis. 2nd ed. McGrawHill, Inc; 2004.
[19] Zhou K, Doyle JC. Essential of robust control. Prentice-Hall; 1998.
[20] Wang F-C, Chen H-T. Design and implementation of fixed-order robust controllers for a proton exchange membrane fuel cell system. International Journal of Hydrogen Energy 2009;34:2705–17.
[21] Kennedy J, Eberhart R. Particle swarm optimization. IEEE International Conference on Neural Networks 1995:1942–8.
[22] Gaing ZL. A particle swarm optimization approach for optimum design of PID controller in AVR system. IEEE Transactions on Energy Conversion 2004;19:384–91.
[23] Mcfarlane DC, Glover K. Robust controller design using normalized coprime factor plant descriptions. In: Lecture notes in control and information sciences, vol. 138. Berlin: Springer-Verlag; 1990.
[24] Skogestad S, Postlethwaite I. Multivariable feedback control: analysis and design. 2nd ed. John Wiley; 2005.
[25] Senjyu T, Nakaji T, Uezato K, Funabashi T. A hybrid power system using alternative energy facilities in isolated island. IEEE Transactions on Energy Conversion 2005;20:406–14.
[26] Sasaki K, Kitai T, Maoka T, Aoki T, Ueno M, Kuwabara T, et al. On the voltage drop of phosphoric acid fuel cell due to its on–off operation. The Transactions of the Institute of Electrical Engineers of Japan 1998;118-B:1450–6.
[27] Lee D-J, Wang L. Small-signal stability analysis of an autonomous hybrid renewable energy power generation/energy storage system part I: time-domain simulations. IEEE Transactions on Energy Conversion 2008;23:311–20.
[28] Hiyama T, Ueno A. Development of real time power system simulator in matlab/simulink environment. IEEE Power Engineering Society Summer Meeting 2000;4:2096–100.